Management of Functional Data Variables in Decomposition-based Design Optimization

by

Michael J. Alexander

A dissertation submitted in partial fulfillment
of the requirements for the degree
Doctor of Philosophy
(Mechanical Engineering)
in The University of Michigan
2011

Doctoral Committee:

Professor Panos Y. Papalambros, Chair
Professor Michael M. Bernitsas
Professor Gregory M. Hulbert
Professor Jeffrey L. Stein
David J. Gorsich, U.S. Army TARDEC

To my family.

Acknowledgements

The Ph.D. process has been one of the most rewarding, challenging, and humbling experiences of my life. Among the key lessons I have learned is how to be passionate about my craft, persevere through significant adversity, and collaborate with others to achieve mutual success. Many people from different facets of my life have facilitated this learning process, and I will be forever indebted to them. My advisor, Prof. Panos Papalambros, has been the primary facilitator of my academic and professional growth over the past five years. Through our regular research meetings as well as his general interactions with other colleagues, he has shown me what it means to be vested in my work and how to approach it with a high level of excellence in terms of creativity, technical merit, and presentation. Furthermore, Prof. Papalambros has demonstrated the importance of life balance through his overall demeanor and concern toward my personal well-being and that of others.

Several other colleagues have been instrumental in my academic and professional development as well. My doctoral committee has provided useful feedback and suggestions regarding the technical details of my research as well as its overall relevance. Dr. Michael Kokkolaras also served as a good resource as he challenged me to master my technical knowledge regarding the motivation, background, and implementation of my work. The expertise and mentorship of Dr. James Allison was invaluable as he assisted with modifications to the original electric vehicle powertrain model, suggested potential solutions to a key research question, and coauthored several conference and journal publications associated with this research. Also, Dr. Jeongwoo Han played a major role in helping me to identify a technical issue in my master's thesis which ultimately led to a major research question in this dissertation.

The friendship and camaraderie of my colleagues within the Optimal Design Laboratory has also been a significant factor in my success. Key collaborations and discussions with Steven Hoffenson, Yi Ren, Kwang Jae Lee, and Dr. Kukhyun Ahn helped me improve the quality of my research, while the encouragement from Dr. Diane Peters, Dr. Abigail Mechtenberg, John and Katie Whitefoot, Soodeh Montazeri, and Anna-Maria McGowan continued to motivate me during challenging times both professionally and personally. Former lab colleagues such as Dr. Bart Frischknecht, Dr. Tahira Reid, and Dr. Jarod Kelly also provided tremendous support throughout this process. Finally, our administrative coordinator Connie Raymond-Schenk played a vital role in the scheduling and planning of my major research activities.

It is without a doubt that my most solid supporters throughout the Ph.D. process have come from within my family and circle of close, personal friends. My father, Dale, has been an outstanding supporter and confidant as he directly understood many of the challenges I faced since he himself is an engineer. My mother, Dwenn, has always been willing to listen and offer encouragement as I struggled to remain motivated at times. My brothers Patrick and Nolan also provided encouragement through their inspirational words, positive attitudes, and light-hearted conversations. Yakaira Ramos, my girlfriend, not only provided significant emotional support but also willingly loaned her computer to me when my own machine malfunctioned in the middle of writing this dissertation. My bible study brothers Jamaal Matthews, Gbenga Olumolade, Davin Phoenix, Memie Ezike, and Mike Logue in Men of Valor provided significant spiritual support through a major personal storm in my life that could have derailed my Ph.D. aspirations. Also, members of the Society of Minority Engineers and Scientists-Graduate Component as well as former faculty, staff, and classmates at the University of Cincinnati have been tremendous supporters throughout the years.

A final aspect that contributed to my success has been the various organizations and/or institutions that have funded my research: the Automotive Research Center, the National Consortium for Graduate Degrees for Minorities in Engineering and Science, Inc., and the Rackham Graduate School. Without these sources of funding, my graduate education and subsequent career aspirations would not have been financially possible.

Table of Contents

List of Figures

List of Tables

Abstract

The design of highly-sophisticated systems such as electric vehicle (EV) powertrains often requires knowledge from several engineering disciplines, making it increasingly advantageous to implement formal, decomposition-based optimization strategies to facilitate design decisions. In techniques such as Analytical Target Cascading (ATC), this requires systems to be represented as a hierarchy of interacting subsystems. Such behavior is formally captured through coupling variables which ensure that the subsystem design solutions are consistent, or in agreement, with one another. Many times the coupling variables exchanged among the subsystems are few in number and scalar-valued, which readily enables the use of ATC. However, other times the coupling variables may consist of highly-discretized functional data, such as motor performance curves in EV powertrain design. Because each element within these vector-valued coupling variables is treated as a decision variable in ATC, the design problem can become prohibitively large for optimization. Therefore, it becomes necessary to implement reduced dimension representations of the functional data that enable efficient, practical design optimization while maintaining reasonable accuracy.

Based on a literature review and some recent work, a method known as proper orthogonal decomposition (POD) has emerged as a leading candidate for the reduced representation of coupled, functional data within decomposition-based design optimization. However, the full capability of this method in terms of dimensionality reduction and its impact on decomposition-based optimization strategies has never been explored. This dissertation therefore presents a case study which modifies the tuning parameter within POD from its nominal value associated with high accuracy and low dimensionality reduction to progressively lower values and observes its impact on ATC design solution accuracy and optimization efficiency (runtime). Since the high-fidelity POD representation yielded the best design solution in terms of accuracy and optimization efficiency, it is concluded that such POD representations are most appropriate for coupled, functional data within ATC. In particular, it is found that high-fidelity POD representations possess good accuracy, reasonable dimensionality reduction, and enhance the functional data consistency among ATC subproblems through additional degrees of freedom (reduced representation variables) compared to low-fidelity POD representations, thus leading to fewer ATC iterations and faster runtimes.

Since consistency measures ultimately impact the convergence of ATC, it is critical to implement an appropriate measure for the coupled, functional data. Because the literature has not revealed any well-established functional data consistency measure for decomposition-based design optimization, this dissertation explores the Accuracy and Validity Algorithm for SIMulation (AVASIM) as an alternative to the "standard" root-mean-square error (RMSE) metric. After demonstrating the flexibility of AVASIM in allocating the importance of local versus global functional data accuracy through a newly-developed generalized formulation, a comparative study is conducted examining the impact of the RMSE, AVASIM, and generalized AVASIM consistency measures on ATC performance. The results indicate that the generalized AVASIM consistency measure is ideal for functional data as it provides a clear indication of consistency and led to the most accurate design solution in the least amount of time in the case study. Specifically, the emphasis on the stable global measure within generalized AVASIM enables it to provide more accurate design solutions using fewer function evaluations.

Finally, it is noted that the reduced representation variables often lack physical meaning, making the determination of their applicability boundary beyond simple bound constraints very difficult. This can lead to ill-behaved analysis and optimization, and so it is necessary to implement an appropriate constraint management technique for the reduced representation variables. Since the existing penalty value-based heuristic is inefficient, this dissertation presents an alternative that augments the former approach with support vector domain description (SVDD) and compares the impact of each technique on ATC performance. The results indicate that the SVDD augmentation is the best constraint management approach since it yielded the best design solution in terms of accuracy and efficiency (including SVDD modeling time). In particular, this method

forces the optimizer to perform more function evaluations in the feasible domain, thus leading to a higher probability of convergence to the optimal design solution with fewer overall function evaluations (and hence less runtime) instead of convergence to any feasible (yet suboptimal) solution.

Chapter 1

Introduction

Complex design problems are often addressed through a decomposition and collaboration process. In the development of an electric vehicle (EV) powertrain, for example, engineers may focus on significant design components such as the battery, electric traction motors, and belt-drive/gearbox transmission systems. These subsystem designs may be evaluated on several system-level criteria, including energy efficiency, performance, range, power availability, and battery packaging space. It is evident, therefore, that the design and evaluation of each powertrain component can be a challenging task to address simultaneously. This may motivate engineers to split the powertrain design process between two teams: a high-level, system design team that is responsible for the battery and belt-drive/gearbox transmission systems along with the selection of motor performance curves such that maximum energy efficiency is achieved, and a low-level, detailed design team that is responsible for ensuring that the specific motors selected meet the performance prescribed at the system level. Hence, although such division of labor may expedite the design process, collaboration is still required in order to provide a single, realizable design solution that satisfies all criteria.

The implementation of this design process on a practical level can often be challenging as it requires an iterative communication and decision-making process between both teams to ensure a feasible, optimal design. One tool that can facilitate this process is design optimization. Design optimization is the process by which evaluative criteria and requirements, known as objectives and constraints, are represented through analytical or simulation-based models and subjected to mathematical programming techniques to identify an optimal design solution [*Papalambros and Wilde* (2000)]. This can be formally written as:

$$\begin{aligned} &\min_{\mathbf{x}} f(\mathbf{x}) \\ &\textit{subject to} \quad \mathbf{g}(\mathbf{x}) \le \mathbf{0},\ \ \mathbf{h}(\mathbf{x}) = \mathbf{0} \end{aligned} \tag{1.1}$$

In the above, **x** is the vector of design (or decision) variables, *f* is the objective function, **g** is the vector of inequality constraints, and **h** is the vector of equality constraints. Formulations of Equation (1.1) that depict the decomposition and collaboration process involved for design problems such as the EV powertrain are known as decomposition-based design optimization strategies. These approaches partition system design problems into subproblems that are decoupled [*Tosserams et al.* (2006)] and solved individually, but include additional constraints to ensure that information coupled among the subproblems (such as the motor performance curves in this example) is consistent, or in agreement, with one another. Among the most effective decomposition-based optimization strategies is Analytical Target Cascading (ATC) [*Kim* (2001); *Kim et al.* (2003)], which uses a hierarchical overlapping coordination strategy. As with other decomposition-based optimization strategies, ATC performs reasonably well when the coupled information among subproblems is limited to a few, scalar-valued terms. However, when this coupled information consists of functional data, such as motor performance curves, these strategies can experience major issues including excessively long runtimes and/or limited convergence. This dissertation specifically addresses these issues by investigating efficient representation methods and consistency measures for coupled, functional data within a decomposition-based optimization framework, such as ATC.

1.1 Optimization with Functional Data

Optimization with respect to functional data can occur in many applications of simulation-based design, including automotive, aerospace, and controls-related problems. In general, functional data are infinite-dimensional design variables that must be represented in some finite form to enable numerical optimization. Because these functional data are generated by computer simulations, discretization is often used as a representation technique, transforming the functional data into finite-dimensional design variables. This can be represented in vector form as

$$z = f(y) \approx F([z_1, z_2, \cdots, z_q]^T, [y_1, y_2, \cdots, y_q]^T, y) \tag{1.2}$$

where y is the independent variable, z is the dependent variable, q is the number of discretized points, and F is some type of interpolation function, such as a lookup table. The problem with this representation is that it usually requires a large number of discretized points to ensure a sufficiently accurate representation of the functional data. In particular, the dimensionality (given by q) of these vector-valued variables can become prohibitively large for design optimization since each discretized point is treated as a decision variable. This issue is further compounded when these variables exist as coupled information in decomposition-based design optimization strategies because of the additional computational overhead already required for such implementations. Therefore, the functional data discretizations, termed vector-valued coupling variables (VVCVs) in decomposition-based optimization strategies, must be approximated with reduced dimension representations that improve optimization efficiency while preserving reasonable accuracy. The variables that are used within these low-dimensional representations are referred to as reduced representation variables [*Alexander* (2008); *Alexander et al*. (2009)].

1.2 Reduced Representations of VVCVs

Reduced representation techniques used in decomposition-based optimization strategies can be broadly categorized according to the manner in which dimensionality reduction is achieved. The two major classifications are metamodeling and curve-fitting approaches. Metamodeling approaches achieve dimensionality reduction by developing a surrogate model of the analysis function that relates a low-dimensional input vector of physical design variables to the VVCV. For example, rather than using a fine discretization of a motor map in design optimization, it may be preferable to create a metamodel of the simulation that produces this map and use its input variables as design variables instead. This is only effective, however, if the dimensionality of the input vector is less than that of the VVCV. It should also be noted that such a reduced representation could be achieved by directly using the analysis function; however, this would contradict the motivation for decomposition-based design optimization, and so the metamodel should be used instead.

Conversely, curve-fitting approaches achieve dimensionality reduction by establishing a functional representation form and varying a small set of parameters to approximate the VVCV. An example of this would be the use of polynomial coefficients in the representation of a dynamic time response history instead of the original, discretized signal. Like metamodeling approaches, this is only effective if the number of parameters is less than the dimensionality of the VVCV. Observe that with these definitions, some reduced representation techniques can be classified as both metamodeling and curve-fitting approaches. The decision regarding which method to implement, however, is ultimately dictated by the approach that uses the minimum number of reduced representation variables.

1.2.1 Prior Work

The published literature on reduced representations of VVCVs in decomposition-based optimization strategies is fairly limited. Sobieski and Kroo [*Sobieski and Kroo* (1996)] experienced reasonable success using Fourier coefficients to represent a lift distribution generated by an aerodynamics subproblem in the design of an aircraft within a collaborative optimization (CO) framework. However, there was no clear indication why this method was sufficient as the paper was primarily focused on demonstrating the capability of CO. Meade and Kokkolaras [*Meade and Kokkolaras* (1996)] addressed this issue from the broader perspective of multidisciplinary analysis in the solution of a viscous-inviscid-interaction airfoil analysis code. In this case, linear combinations of quadratic polynomials were used to approximate transpiration velocity vectors exchanged between underlying coupled analysis functions that were solved iteratively. Nevertheless, because the dimensionality reduction problem was not the primary focus of the paper, there was limited information regarding the motivation for the selection of the method. Delagrammatikas [*Delagrammatikas* (2001)] represented engine torque curves exchanged between subproblems in a specialized decomposition-based design optimization strategy for advanced powertrains through a coarse, four-point discretization. Such an approach was satisfactory but not robust for this study since the unstable accuracy of the reduced representation had the potential to lead to infeasible or suboptimal engine designs. Finally, LeGresley and Alonso [*LeGresley and Alonso* (2004)] used proper orthogonal decomposition (POD) to represent surface pressure and structural displacement distributions generated by aerodynamics and structural subproblems in the optimization of a low-fidelity aeroelastic model within a bi-level integrated system synthesis (BLISS) optimization framework. Although the authors produced promising results, they also acknowledged the need to demonstrate the effectiveness of POD in a more compelling problem that contained higher-fidelity models.

The motivating design application for this dissertation was the optimization of a hybrid-electric vehicle (HEV) powertrain system using ATC optimization. In early unpublished work, it was necessary to reduce the dimensionality of VVCVs associated with maximum and minimum motor torque curves and power loss maps. Polynomial response surface approximation [*Box and Hunter* (1957); *Box and Draper* (1987); *George and Ogot* (2006)] was initially implemented, with the polynomial coefficients serving as reduced representation variables. However, this was ineffective since many coefficients were required to produce approximations of reasonable accuracy. A more heuristic approach involved the use of weight coefficients as reduced representation variables in the linear interpolation of two distinct “baseline” functions to approximate the VVCVs. While this technique significantly reduced the dimensionality of the VVCVs, the accuracy of the new representations was severely compromised. Weight coefficients were also used as reduced representation variables in the linear combination of orthogonal functions [*Sansone and Hille* (2004); *Bretscher* (2005)] to approximate the VVCVs. Although orthogonality conditions could not be strictly enforced, this method demonstrated high capability due to its similarity to POD. Image warping [*Glasbey and*

Mardia (1998); *Stegmann* (2001)], which used warping parameters as reduced representation variables, also demonstrated some capability but possessed challenges in determining appropriate transformations for the VVCVs. In the end, it was found that using low-dimensional input vectors to radial-basis function (RBF) artificial neural networks (ANNs) [*Chen et al.* (1991); *Demuth et al.* (2009)] as reduced representations according to Kokkolaras et al. [*Kokkolaras et al.* (2004)] was a reasonable approach due to its high accuracy.

1.2.2 Recent Work

Because RBF ANNs were an established reduced representation method for VVCVs in HEV powertrain design and POD demonstrated high potential based on the literature review, a new study [*Alexander et al.* (2010a)] was conducted that compared the two techniques. Specifically, RBF ANNs and POD were used as reduced representations for VVCVs associated with maximum/minimum motor torque curves and power loss maps in the ATC optimization of an EV powertrain. RBF ANNs served as the baseline method in the investigation since it was previously implemented in two similar studies. Based on the results, it was found that POD was the better reduced representation technique in this application. The most significant reason for this assessment was that implementing RBF ANNs, which is a metamodeling approach, violated the necessary condition of additive-separability [*Wagner and Papalambros* (1993)] for decomposition-based optimization strategies. This requires that functions, including objectives and constraints, in a system design problem be expressed as a sum of terms, with each term dependent on disjoint subsets of design variables. The violation of this property implied that an all-in-one (AiO) optimization problem formulation should have been used, which was not the goal of the study. Conversely, POD, which is a curve-fitting approach, easily satisfied additive-separability within ATC as it used reduced representation variables (POD coefficients) that were distinct from all other system design variables. In the rare event that RBF ANNs did satisfy additive-separability, the dimensionality of the reduced representation would not be guaranteed to be less than the dimensionality of the original VVCV for every application. POD, however, would always generate reduced representations with lower dimensionality than the original VVCV by virtue of its method. A final limitation of RBF ANNs (assuming additive-separability and dimensionality reduction were satisfied) was its lack of flexibility in dimensionality reduction. Regardless of the desired accuracy, the number of reduced representation variables for RBF ANNs would always be equal to the number of inputs to the network. The number of reduced representation variables for POD, however, is directly related to a tuning parameter that trades off accuracy and dimensionality reduction, which would enable tremendous flexibility.

Although it was acknowledged that the limitations of RBF ANNs could exist for any reduced representation, it was also observed that metamodeling approaches generally experience these issues more frequently as they use variables that may not reduce problem dimensionality and may violate additive-separability. Curve-fitting approaches were identified as more suitable because they use variables that reduce problem dimensionality more consistently and are unlikely to violate additive-separability. Of these latter approaches, POD emerged as one of the most attractive since it utilized data samples exclusively to determine a functional form of its approximation model, made limited assumptions regarding the number of reduced representation variables, and used a relatively limited number of such variables for approximation.

Despite these advantages, there are still two key issues that must be addressed when implementing POD as a reduced representation. First, more insight is required regarding the impact of the tuning parameter within POD on the performance of ATC. As indicated earlier, this parameter balances accuracy with dimensionality reduction of the POD representation, which enables tremendous flexibility for the reduced representation of VVCVs. Although it was set to a "nominal" value in this study that favored accuracy, such an approach may not be appropriate in general as it may limit the full capability of POD in terms of reduced representation and hence optimization efficiency. It is posited that as the tuning parameter is adjusted to favor dimensionality reduction, additional computational savings will be observed via fewer reduced representation variables; however, this has yet to be demonstrated. Furthermore, while such an adjustment would reduce the accuracy of the POD representation, it is uncertain whether this would translate into an inaccurate or suboptimal design solution as ATC enforces some degree of accuracy through its updated, weighted penalty function. Since the literature does not currently address this issue for any decomposition-based optimization strategy, it is necessary that the work in this dissertation resolves this issue.

Another problem that must be resolved is the effective constraint management of the POD reduced representation variables. Initial optimization runs using POD failed during this study due to powertrain simulation crashes, and closer inspection revealed that the POD approximation of the motor maps was inaccurate (Figure 1.1). This in turn was caused by the optimizer selecting reduced representation variables that were outside the POD model validity region as shown in Figure 1.2. Hence, the original assumption that the POD model validity region was defined by simple bound constraints was incorrect; instead, nonlinear constraints characterized the decision space, which is only partially seen in Figure 1.2. Because these reduced representation variables lacked physical meaning, it was challenging to formulate explicit constraints defining the model validity region. This issue was temporarily resolved by assigning large penalty values to objective and constraint function outputs that depended on the reduced representation variables when simulation failure occurred. Such a penalty value-based heuristic was effective for the non-gradient-based optimizer used in this study as it forced the selection of reduced representation variables that were within the model validity region. However, this heuristic was not efficient; it required many ATC iterations that ultimately led to an ill-conditioned optimization problem and an extensive runtime. The study indicated that the POD model validity region should ideally be constrained using a more direct approach that produces explicit constraints in the optimization formulation. This would facilitate the efficient performance of the optimizer and lead to fewer ATC iterations and faster runtimes.

Some common methods in the literature, such as probability density-based models [*Tarassenko et al.* (1995)] and convex hulling algorithms like Quickhull [*Barber et al.* (1996)], were considered as potential direct constraint management approaches but had significant limitations [*Malak* (2008)]. The probability density-based models, for example, generally require large datasets for a good boundary definition; however, the availability of such data may not always be possible [*Malak* (2008)]. In the case of convex hulling, many of these algorithms were not intended for the high-dimensional datasets that may still be present after using reduced representations such as POD. Moreover, such datasets are usually non-convex, and so the use of a convex hulling algorithm could generate boundary definitions that are ill-defined as in Figure 1.2. However, a method that utilizes support vector domain description [*Tax and Duin* (1999a); *Tax and Duin* (1999b)] and initially explored as part of this dissertation work [*Alexander et al.* (2010b)] was suggested as a promising solution to this problem. Because the work by Alexander et al. was in its preliminary phases, this dissertation must examine the implications of this approach in a more complete fashion.

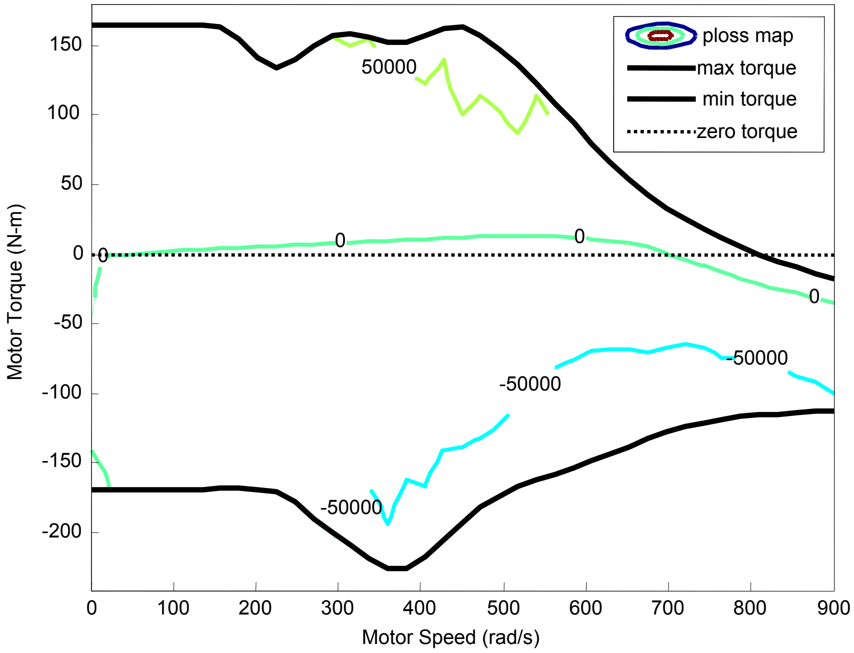

Figure 1.1 POD-Approximated Motor Map at Failed Design Point

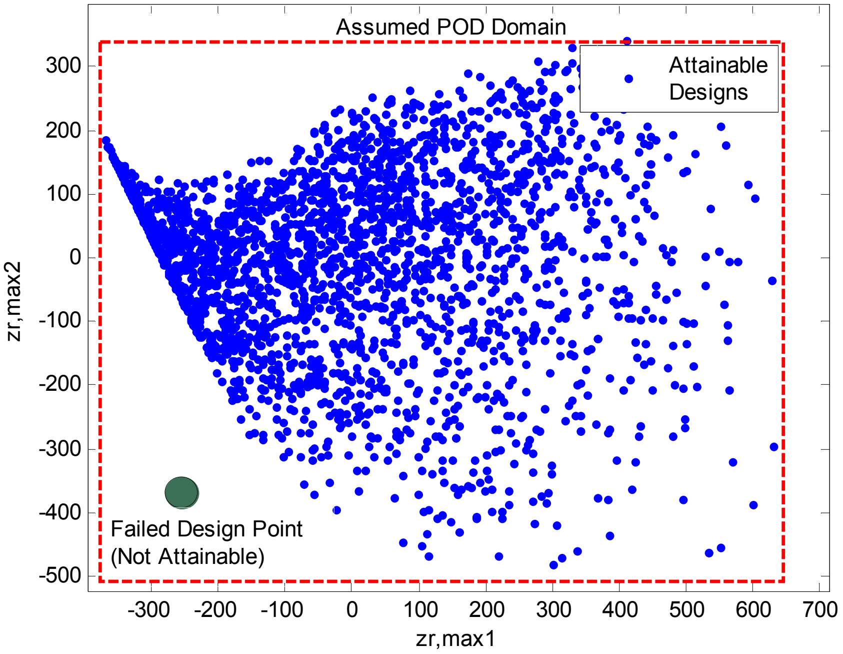

Figure 1.2 POD Model Validity Region for Two Components

1.2.3 Selection Criteria for Reduced Representations

The insights gained from both the prior and current work on reduced representations in decomposition-based optimization strategies have facilitated the development of slightly more formal selection criteria than dimensionality reduction and accuracy preservation. In particular, techniques considered for reduced representation should satisfy the following criteria:

1. The method should not violate additive-separability in decomposition-based optimization strategies.
2. The method should require minimal assumptions regarding the functional form of approximation.
3. The method should require minimal assumptions regarding the number of reduced representation variables to be used.

Another property that is ideal, but not necessary, is that the reduced representation should minimize the VVCV dimensionality such that it does not exceed the local design vector dimensionality in a given subproblem within decomposition-based optimization. As mentioned earlier, most of these strategies perform well when the number of coupling variables is limited, and so the satisfaction of this property would facilitate a well-conditioned decomposition-based optimization problem. For example, if an ATC strategy included a subproblem with a 5-dimensional local design vector and a 40-dimensional VVCV, the reduced representation should contain no more than 5 variables. Such a condition is problem-dependent, however, and may not always be capable of being satisfied. Therefore, this property is not strictly enforced in current research.

Upon reviewing the criteria listed above, it becomes evident why POD is among the leading methods for reduced representation. Additive-separability is rarely satisfied by metamodeling methods, and so this encourages the exploration of curve-fitting methods. Common approaches, such as polynomial response surfaces, are eliminated as they require strong assumptions about the functional form of the approximation (linear, quadratic, etc.) that are challenging to make when there is significant variation in the form of the functional data, which is often the case for these design problems. Other techniques, such as Fourier approximations and image warping, require many assumptions regarding the number of fitting parameters, or reduced representation variables, to use, which can add significant offline development time before optimization. However, as previously indicated, POD constructs unique functional forms (orthogonal basis functions) for a given problem based on functional data samples and uses only a single parameter to determine the number of reduced representation variables (POD coefficients). It is acknowledged, however, that POD may not be the best reduced representation for every problem application in general. Before this can be reasonably determined, other important issues, such as the impact of the tuning parameter within POD and the constraint management of the reduced representation variables, must be addressed. It is especially critical to note that the latter issue is not limited to POD, but is relevant to any alternative curve-fitting approach that uses reduced representation variables that are abstract quantities. Therefore, an appropriate solution to this latter problem would have broad implications.

1.3 Accuracy Assessment of Reduced Representations

Another important aspect of reduced representations is their ability to maintain reasonable accuracy. Although the reduced representation variables are used as decision variables in optimization, they still must compute approximations of the relevant functional data that can be utilized to solve the problem accurately. In the case of the EV powertrain design problem mentioned in this work, this includes motor torque curves, which are one-dimensional (1D) functional data, and motor power loss maps, which are two-dimensional (2D) functional data. Error metrics such as the mean-square error (MSE) or the root-mean-square error (RMSE) have been routinely used to validate these functional data approximations in the past [*Meckesheimer et al.* (2001); *Mullur and Messac* (2005); *Wang and Shan* (2007)]. However, the majority of these metrics were developed for 1D functional data accuracy assessment, and as such, perform well for this type of data. The suitability and performance of these metrics for higher dimensional functional data, such as 2D functional data, have been largely unexplored until recent work undertaken as part of this dissertation effort [*Alexander and Papalambros* (2010)]. Because the assumptions regarding the functional form and the number of variables for reduced representations are contingent upon accuracy assessment, the resolution of such an issue is critical. Moreover, decomposition-based design optimization strategies require effective consistency measures to assess the discrepancy between coupled quantities, including functional data, from different subproblems to facilitate convergence. These consistency measures are based on some type of error metric which should determine any discrepancy among the coupled quantities in a meaningful and accurate way. Currently, no well-established consistency measure exists for coupled functional data within decomposition-based optimization strategies in the literature, and so the standard practice [*Alexander* (2008); *Alexander et al.* (2009); *Alexander et al.* (2010a); *Alexander et al.* (2010b); *Alexander et al.* (2010c)] has been to use a RMSE consistency measure. Although this error metric has facilitated the use of decomposition-based optimization strategies such as ATC in the past, it may not be appropriate for higher dimensional functional data (such as motor power loss maps) and lacks a clear definition of consistency among coupled functional data. It is therefore necessary to identify a suitable error metric that can validate higher dimensional functional data approximations generated by reduced representations and support the convergence of decomposition-based optimization strategies with coupled functional data through a meaningful consistency measure.

The literature on 1D functional data accuracy assessment through error metrics is vast. Sarin provides a comprehensive list and description of these methods, along with key error measures such as magnitude, phase, and shape [*Sarin* (2008)]. Since this application deals with the validation of functional data approximations against functional data from high-fidelity simulations, the phase error measure is not as significant. Instead, error metrics that are robust and primarily address magnitude and shape error measures are considered. Vector norms, for example, form the basis of many error metrics, such as MSE and RMSE, and are relatively simple to use [*Sarin* (2008)]. Average residuals and their standard deviations are also straightforward in their implementation, but have the disadvantage of cancellation for comparisons containing positive and negative residuals [*Sarin* (2008)]. The coefficient of correlation and 0^{th}-2^{nd} order relative difference of moments are slightly more advanced than vector norms and, in the absence of significant phase error, possess effective measures of magnitude error [*Sarin* (2008)]. Sprague and Geers' error metric [*Geers* (1984); *Sprague and Geers* (2004); *Schwer* (2005)] and the similar Russell's error metric [*Russell* (1997a); *Russell* (1997b)] possess a measure that specifically addresses magnitude error; however, neither of these metrics can address shape error. Conversely, the normalized integrated square error [*Jacob et al.* (2000)] does possess measures of magnitude and shape error, but cannot account for the shape error in the overall metric. Dynamic time warping [*Keogh and Pazzani* (1999); *Liu et al.* (2002); *Ratanamahatana and Keogh* (2004); *Fang et al.* (2005); *Faundez-Zanuy* (2007)] and the Error Assessment of Response Time Histories metric or EARTH [*Sarin* (2008)] are advanced methods that effectively measure the magnitude and shape errors, but have the disadvantage of extensive computational time as they both require the solution of a dynamic programming problem. Although any of the aforementioned techniques could be selected for the initial inclusion of 2D functional data accuracy assessment, it is preferable to start with the simplest meaningful approach to gain some understanding. Of particular interest are error metrics that systematically, objectively and efficiently provide a clear indication of local and global functional data accuracy with respect to preset thresholds [*Sohns et al.* (2006)]. With these goals in mind, the metric selected for all functional data accuracy assessment in this dissertation was the Accuracy and Validity Algorithm for SIMulation, or AVASIM [*Sendur et al.* (2002)]. This metric is also investigated in this dissertation as an alternative for functional data consistency measurement within decomposition-based design optimization.

1.4 Summary and Overview

This chapter introduced the main research problem in this dissertation, which deals with the efficient and accurate representation of functional data that are (coupled) decision variables in a decomposition-based design optimization problem. It also presented the relevant problem application that will be focused on in this dissertation, which is EV powertrain design. In addition, reduced representation techniques were discussed, along with their appropriate selection criteria. This information was used to demonstrate the motivation for the exclusive use of POD in this work. Finally, the importance of an effective accuracy assessment tool was explained, and the literature review indicated the appropriateness of AVASIM as an error metric for functional data.

The remainder of the dissertation will delve deeper into the issues surrounding the management of VVCVs in ATC. Specifically, three key research questions that will serve as significant contributions to the research community will be addressed:

1. What effect do assumptions regarding the number of reduced representation variables have on the performance, including computational efficiency and accuracy, of ATC?
2. What are effective consistency measures for functional data that are coupled between design subproblems in ATC?
3. What are effective constraint management methods for reduced representation variables in ATC?

The first research question is based on an earlier discussion in this chapter regarding the net impact of the tuning parameter within POD on the performance of ATC. To address this issue, a study will be conducted that varies this tuning parameter from its “nominal” value, which favors accuracy, to progressively lower values that favor dimensionality reduction (fewer reduced representation variables) while observing the ATC optimization results. The second research question deals with the issue of assessing the discrepancy between coupled functional data from various subproblems within ATC in an accurate and meaningful way as mentioned earlier in this chapter. A comparative study between an existing consistency measure (RMSE) and AVASIM will be conducted to resolve this problem. Finally, the third research question addresses the problem of properly constraining abstract reduced representation variables in an ATC framework as previously discussed in this chapter. Specifically, a comparative study between an existing constraint management method (penalty value-based heuristic) and an alternative that utilizes support vector domain description will be conducted to resolve this issue.

The dissertation is organized as follows: Chapter 2 provides background information on ATC, POD, and AVASIM; Chapter 3 discusses the EV powertrain models that will be used in the case studies, which include a small, commercial EV powertrain and a military light-tactical EV powertrain; Chapters 4, 5, and 6 investigate the first, second and third research questions, respectively, using the commercial EV model as a design application; Chapter 7 applies the understanding gained from addressing the research questions to the more challenging military EV design problem; and Chapter 8 offers conclusions regarding the original research problem.

Chapter 2

Background

The preference for ATC, POD, and AVASIM as tools that support EV powertrain design was discussed in the previous chapter. The details of these methods are provided in this chapter to facilitate the understanding of relevant case studies later in the dissertation. ATC is discussed first along with important information regarding the problem structure, formulation, and coordination strategy. POD is presented next, including the description of two solution methods based on the number of data samples. Finally, the details of AVASIM are provided for both 1D and 2D functional data accuracy assessment.

2.1 Analytical Target Cascading

In design optimization, methods that partition complex system design problems into subproblems and optimize the subsystems while ensuring consistency among their solutions are known as decomposition-based design optimization strategies. Several hierarchical strategies, including Sobieski's framework [*Sobieszczanski-Sobieski et al.* (1985)], Cramer's formulations [*Cramer et al.* (1994)], and collaborative optimization (CO) [*Braun* (1996)], have been developed in earlier work. Among the most effective decomposition-based optimization strategies is Analytical Target Cascading (ATC). This method [*Kim* (2001); *Kim et al.* (2003)] has attracted much attention due to the intuitive nature of its hierarchical decomposition and coordination strategy. Furthermore, unlike its widely-used predecessor (CO), ATC possesses a proven convergence theorem [*Michelena et al.* (2003)] which states that its design solution is identical to that of the corresponding all-in-one (AiO) optimization problem when the consistency among linked subproblems is satisfied exactly. From a high-level perspective, ATC simultaneously minimizes performance-related objectives and deviations between design targets cascaded from upper levels and their realizable responses at lower levels. Optimality is achieved when the targets and responses are within an acceptable tolerance of one another.

ATC begins by first decomposing the system into design subproblems, where typically the top level is referred to as the system level and lower levels are referred to as subsystem levels (Figure 2.1). Note that a subproblem linked above a given element of interest is called a parent, and subproblems linked below a given element of interest are called children. The general ATC subproblem P_{ij} for the *ith* level and the *jth* element is defined as [*Tosserams et al.* (2006)]:

$$\begin{aligned}
&\min_{\bar{\mathbf{x}}_{ij}} f_{ij}(\bar{\mathbf{x}}_{ij}) + \pi(\mathbf{c}(\bar{\mathbf{x}}_{11}, \cdots, \bar{\mathbf{x}}_{NM})) \\
&\textit{subject to} \quad \mathbf{g}_{ij}(\bar{\mathbf{x}}_{ij}) \leq \mathbf{0},\ \mathbf{h}_{ij}(\bar{\mathbf{x}}_{ij}) = \mathbf{0} \qquad (2.1) \\
&\textit{where} \qquad \bar{\mathbf{x}}_{ij} = [\mathbf{x}_{ij}, \mathbf{r}_{ij}, \mathbf{t}_{(i+1)k_1}, \cdots, \mathbf{t}_{(i+1)k_{c_{ij}}}],\ \mathbf{c} = [\mathbf{c}_{22}, \cdots, \mathbf{c}_{NM}]
\end{aligned}$$

In the above, $\mathbf{x}_{ij}$ is the vector of local design variables, $\mathbf{t}_{ij}$ is the vector of target linking variables passed from the element's parent at level (i - 1), $\mathbf{r}_{ij}$ is the vector of response linking variables passed to the element's parent at level (i - 1), $\mathbf{c}_{ij} = \mathbf{t}_{ij} - \mathbf{r}_{ij}$ is the vector of consistency constraints between target and response linking variables, f_{ij} is the local objective function, π is a penalty function, $\mathbf{g}_{ij}$ is the vector of inequality constraints, $\mathbf{h}_{ij}$ is

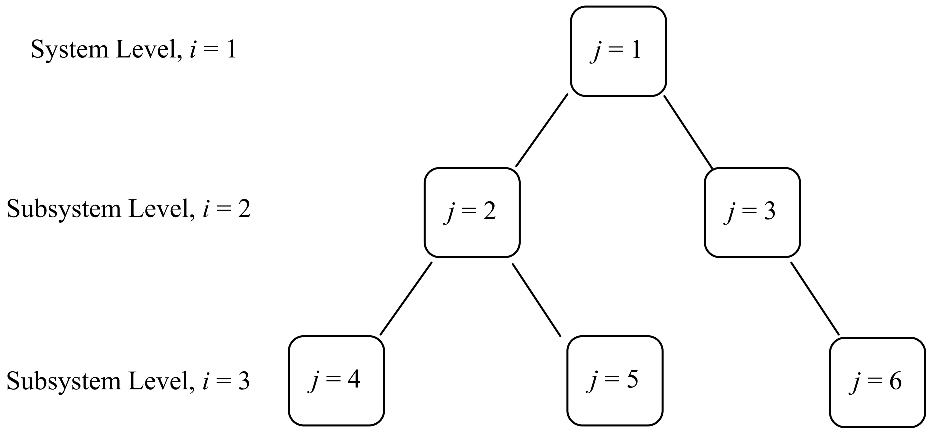

Figure 2.1 ATC Hierarchical Decomposition [*Tosserams et al.* (2006)]

the vector of equality constraints, N is the number of levels, and M is the total number of elements. Although $\mathbf{t}_{ij}$ and $\mathbf{r}_{ij}$ can include both coupling and shared variables, only coupling variables are present in the examples in this dissertation. Also, observe that the consistency constraints, which should be zero for an exact system solution, are relaxed through $\pi(\mathbf{c})$ such that $\|\mathbf{c}^{(K)} - \mathbf{c}^{(K\text{-}1)}\|_\infty$ is within some small tolerance before the algorithm is terminated, where K denotes the iteration number. Among the most effective choices for π is the augmented-Lagrangian (AL) function, which results in the following general ATC-AL subproblem formulation for the *ith* level and the *jth* element [*Tosserams et al.* (2006)]:

$$\begin{aligned}
&\min_{\bar{\mathbf{x}}_{ij}} f_{ij}(\bar{\mathbf{x}}_{ij}) - \mathbf{v}_{ij}^T\mathbf{r}_{ij} + \sum_{k\in C_{ij}} \mathbf{v}_{(i+1)k}^T\mathbf{t}_{(i+1)k} + \left\|\mathbf{w}_{ij}\circ(\mathbf{t}_{ij}-\mathbf{r}_{ij})\right\|_2^2 + \sum_{k\in C_{ij}}\left\|\mathbf{w}_{ij}\circ(\mathbf{t}_{(i+1)k}-\mathbf{r}_{(i+1)k})\right\|_2^2 \\
&\textit{subject to}\quad \mathbf{g}_{ij}(\bar{\mathbf{x}}_{ij}) \le \mathbf{0},\ \mathbf{h}_{ij}(\bar{\mathbf{x}}_{ij}) = \mathbf{0} \qquad\qquad (2.2)\\
&\textit{where}\qquad \bar{\mathbf{x}}_{ij} = [\mathbf{x}_{ij}, \mathbf{r}_{ij}, \mathbf{t}_{(i+1)k_1}, \cdots, \mathbf{t}_{(i+1)k_{c_{ij}}}]
\end{aligned}$$

Note that the linear and quadratic terms in the AL penalty function are weighted by the vectors **v** and **w**, respectively.

Figure 2.2 illustrates the information flow for the general ATC-AL subproblem formulation. The linking variable vectors $\mathbf{t}_{ij}$ and $\mathbf{r}_{(i+1)k}$ are passed as inputs from the subproblem's parent and children, respectively. They are treated as fixed parameters, while the linking variable vectors $\mathbf{r}_{ij}$ and $\mathbf{t}_{(i+1)k}$ are treated as decision variables, along with $\mathbf{x}_{ij}$. After the subproblem is solved, $\mathbf{r}_{ij}$ and $\mathbf{t}_{(i+1)k}$ are passed back to the subproblem's parent and children, respectively, as an indication of the consistency between adjacent subproblems. With this process defined, the complete algorithm for ATC-AL, which is known as the "method of multipliers" is as follows [*Tosserams et al.* (2006)]:

0. (Initialize): Define decomposed problem and initial solutions $\mathbf{x}^{(0)}$, $\mathbf{r}^{(0)}$, $\mathbf{t}^{(0)}$; set $\kappa = 0$; define outer loop termination criterion, ε, where ε is a small, positive number. Define $\mathbf{v}^{(1)}$ and $\mathbf{w}^{(1)}$.
1. (Inner loop/solve ATC): Set $\kappa = \kappa+1$. Solve decomposed problem with $\mathbf{v}^{(\kappa)}$, $\mathbf{w}^{(\kappa)}$ to obtain new estimates $\mathbf{x}^{(\kappa)}$, $\mathbf{r}^{(\kappa)}$, $\mathbf{t}^{(\kappa)}$.

2. (Convergence check): If outer loop converges ($\|\mathbf{c}^{(\kappa)}-\mathbf{c}^{(\kappa-1)}\|_\infty < \varepsilon$), set $\kappa = K$ and stop. Otherwise, proceed to Step 3.
3. (Outer loop/update penalty): Update penalty parameters to $\mathbf{v}^{(\kappa+1)}$ and $\mathbf{w}^{(\kappa+1)}$ with respective linear updating schemes using Step 1 results:

$$\begin{aligned} \mathbf{v}^{(K+1)} &= \mathbf{v}^{(K)} + 2\mathbf{w}^{(K)} \circ \mathbf{w}^{(K)} \circ \mathbf{c}^{(K)} \\ \mathbf{w}^{(K+1)} &= \beta\mathbf{w}^{(K)},\ where\ \beta \geq 1 \end{aligned} \tag{2.3}$$

Return to Step 1.

This algorithm converges assuming that the problem is convex (which is enforced by $\beta \geq 1$) and that the sequence of quadratic weight vectors **w** is non-decreasing.

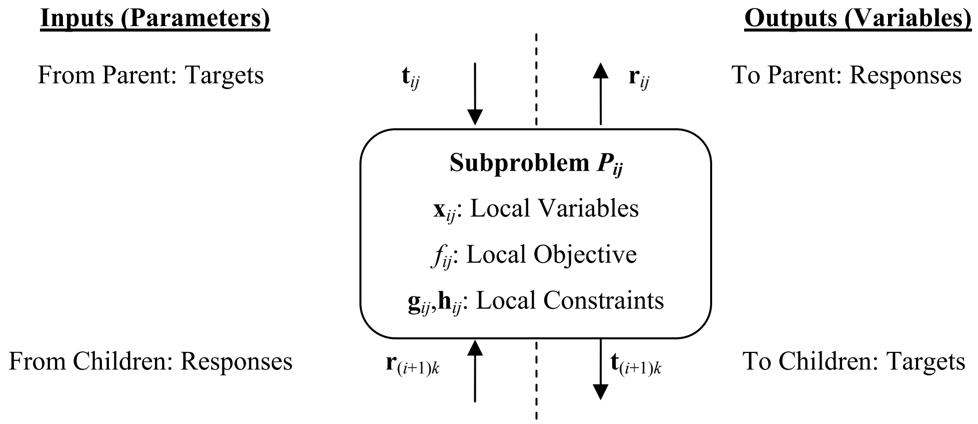

Figure 2.2 ATC Information Flow [*Tosserams et al.* (2006)]

The computational efficiency of ATC is often improved by using an inner loop coordination strategy known as the "alternating direction method" [*Tosserams et al.* (2006)], or AD. While earlier coordination strategies required ATC subproblems to be solved iteratively [*Michelena et al.* (2003)], this approach requires each subproblem to be solved only once in the inner loop. The simplest implementation of the ATC-AL-AD algorithm is to solve each subproblem sequentially starting at the top of the hierarchy and ending at the bottom. Such an approach enables the efficient solution of a decomposition-based design optimization problem while maintaining reasonable accuracy [*Tosserams et al.* (2006)].

2.2 Proper Orthogonal Decomposition

Proper orthogonal decomposition (POD) is often used in engineering applications as a model reduction technique to facilitate the analysis, design, and optimization of dynamic, linear systems. In broader applications, POD is also referred to as principal component analysis [*Ahmed and Goldstein* (1975)] or Karhunen-Loeve expansion [*Loeve* (1945); *Karhunen* (1946)]. Mathematically, all of these terms refer to the same linear transformation method, but with a particular meaning in various fields. POD, in particular, reduces the state-space representation of dynamic systems according to [*Wilcox* (2005)]:

$$\mathbf{z}(t) \approx \mathbf{\Phi}_p \mathbf{z}_r(t) + \overline{\mathbf{z}}(t) \tag{2.4}$$

Here, $\mathbf{z}(t)$ is the original state vector of dimension q, $\mathbf{z}_r(t)$ is the reduced state vector of dimension $p << q$, and $\mathbf{\Phi}_p$ is a matrix of the p most energetic basis functions $\boldsymbol{\varphi}$ used to construct the approximation of the original state vector. The final term $\overline{\mathbf{z}}(t)$ is the sample mean vector of dimension q and is used to center the data for the approximation. This transformation can be applied to the functional data variables in this dissertation by treating them as state vectors, thus modifying (2.4) by

$$\mathbf{z} \approx \mathbf{\Phi}_p \mathbf{z}_r + \overline{\mathbf{z}} \tag{2.5}$$

where $\mathbf{z}$ is the original q-dimensional functional data variable, $\mathbf{z}_r$ is the p-dimensional reduced representation, and $\mathbf{\Phi}_p$ and $\overline{\mathbf{z}}$ have the same meaning as in the state vector context but applied to the functional data variables. POD ultimately involves the construction of the full basis function matrix $\mathbf{\Phi}$ based on m samples $\mathbf{z}_i = [z_1, z_2, \ldots, z_q]^T$ and its reduction by examining the magnitude of its associated eigenvalues. This is accomplished by using either the direct method or the "method of snapshots" [*Sirovich* (1987)].

The most efficient approach when $q \leq m$ is the direct method [*Burkhardt et al.* (2003)], which begins by forming the covariance matrix **R**:

$$\mathbf{R} = \frac{\left(\mathbf{Z} - \overline{\mathbf{Z}}\right)\left(\mathbf{Z} - \overline{\mathbf{Z}}\right)^T}{m - 1} \tag{2.6}$$

In the above, **Z** is a (q x m) matrix containing all the samples of the original functional data variables and **Z** is a (q x m) matrix of the sample mean vector repeated m times. Next, a (q x q) eigenvalue problem on **R** is used to construct **Φ**,

$$\mathbf{R\Phi} = \mathbf{\Phi\Lambda} \tag{2.7}$$

where **Λ** is the diagonal matrix of eigenvalues. Assuming that the basis functions in **Φ** are arranged according to the magnitude of their associated eigenvalues,

$$\mathbf{\Phi} = \begin{bmatrix} \boldsymbol{\varphi}_1 & \boldsymbol{\varphi}_2 & \cdots & \boldsymbol{\varphi}_q \end{bmatrix}^T, \lambda_1 > \lambda_1 > \cdots > \lambda_q \tag{2.8}$$

this matrix is reduced to $\mathbf{\Phi}_p$ based on the cumulative percentage variation (CPV). The CPV is a measure of the relative importance of each basis function in **Φ** [*Toal et al.* (2008)]:

$$\frac{\sum_{i=1}^{p} \lambda_i}{\sum_{i=1}^{q} \lambda_i} \times 100 \geq CPV_{goal} \tag{2.9}$$

Observe that CPV_{goal} is assigned based on the desired amount of information to be captured through POD, which is usually 99% [*Bui-Thanh et al.* (2004)].

When $q > m$, the most efficient solution technique [*Burkhardt et al.* (2003); *Lucia et al.* (2003); *Wilcox* (2005)] is the "method of snapshots" [*Sirovich* (1987)]. This time, a correlation matrix **R** is generated:

$$\mathbf{R} = \frac{\left(\mathbf{Z} - \overline{\mathbf{Z}}\right)^T \left(\mathbf{Z} - \overline{\mathbf{Z}}\right)}{m} \tag{2.10}$$

From here, the associated (m x m) eigenvalue problem is solved,

$$\mathbf{RV} = \mathbf{V\Lambda} \tag{2.11}$$

where **V** represents the matrix of eigenvectors. The (q x m) orthogonal basis function matrix is constructed from:

$$\mathbf{\Phi} = \mathbf{ZV}_n, \quad v_{n,ij} = \left(1/\sqrt{m\lambda_{ii}}\right)v_{ij} \tag{2.12}$$

The above equations demonstrate why this procedure is referred to as the "method of snapshots": each basis function is a linear combination of the m sample vectors, or "snapshots", of original data [*Sirovich* (1987)]. Finally, $\mathbf{\Phi}_p$ is determined using the same procedure outlined in Equations (2.8)-(2.9) with q replaced by m.

2.3 Accuracy and Validity Algorithm for Simulation

The Accuracy and Validity Algorithm for SIMulation, or AVASIM [*Sendur et al.* (2002)], is an accuracy assessment tool that characterizes the local and global error between baseline and approximation functional data through ℓ_1-norms and residual sums. Using these measures, error indices are constructed such that nonnegative values denote valid functional data approximations with accuracy levels between 0 and 1, and all negative values generally denote invalid functional data approximations. Validity is defined by functional data approximations that lie within some predetermined threshold value; therefore, a value of 0 indicates that a functional data approximation is at the threshold and valid, whereas a value of 1 indicates that a functional data approximation is completely accurate.

2.3.1 Algorithm

The algorithm begins by selecting points of interest, known as target points [*Sohns et al.* (2006)], from the baseline functional data. These target points are used to calculate the local error index between the baseline and approximation functional data through an ℓ_1-norm indirectly. In addition, a percentage error tolerance tol_i must be assigned to each target point based on its desired accuracy level. The local error index between the baseline and approximation functional data for a single target point is therefore

$$E_{local,i} = 1 - \frac{|y_i - \hat{y}_i|}{y_i tol_i} \tag{2.13}$$

where y_i and $\hat{y}_i$ denote target point values from the baseline and approximation functional data, respectively. Observe that the above formulation degrades when $y_i \leq 0$ as this would either lead to division by zero or index values greater than 1. On a practical level, the division-by-zero issue may be resolved by setting $y_i = \delta$, where δ is a small, positive number. The index value issue can be alleviated by simply taking the absolute value of the denominator in Equation (2.13). With these problems addressed, an overall measure of the local error can be found by averaging $E_{local,i}$ for all n_p target points:

$$E_{local} = \frac{1}{n_p} \sum_{i=1}^{n_p} E_{local,i} \tag{2.14}$$

In the next phase, it is necessary to calculate the residual sum between the baseline and approximation functional data [*Sohns et al.* (2006)]. This value is used in conjunction with another residual sum between the baseline functional data and some threshold functional data to compute the global error index. The first residual sum is given by

$$RS_{app} = \int_0^X \left| y(x) - \hat{y}(x) \right| dx \tag{2.15}$$

where $y(x)$ and $\hat{y}(x)$ represent the complete baseline and approximation functional data respectively and X is the domain over which the functional data are defined. Similarly, the second residual sum is given by

$$RS_{thresh} = \int_0^X \left| y(x) - y_{thresh}(x) \right| dx, \qquad y_{thresh}(x) = ay(x+b) \tag{2.16}$$

where $y_{thresh}(x)$ represents the complete threshold functional data. It is this residual sum that sets a maximum acceptable value for the global error. Note that the amplitude threshold coefficient a and the phase threshold coefficient b help set this value based on tol_i:

$$a = 1 + \min(tol_i), \qquad b = \min\left(\left| tol_i x_i^{base} \right|\right) \tag{2.17}$$

With this definition, the global error index between the baseline and approximation functional data is given by

$$E_{global} = 1 - \frac{RS_{app}}{RS_{thresh}} \tag{2.18}$$

The combined error index E_{comb} is found by simply calculating the arithmetic mean of the results of Equations (2.14) and (2.18). Typically, E_{comb} is used to gain a sense not only of the overall error between the functional data but also of whether an approximation is even valid with respect to the preset tolerances. Such a condition is referred to as a liberal validity criterion [*Sohns et al.* (2006)] as it only requires E_{comb} to be nonnegative for valid curve approximations. Conversely, if it is required that E_{local} and E_{global} (and hence E_{comb})

be nonnegative, then this condition is known as a conservative validity criterion [*Sohns et al.* (2006)].

Alexander and Papalambros [*Alexander and Papalambros* (2010)] used the previous equations to extend AVASIM for the accuracy assessment of 2D functional data by simply modifying the residual sums with double integration. Let $z(x,y)$ and $\hat{z}(x,y)$ represent the baseline and approximation functional data, respectively. Then the residual sum between the baseline and approximation functional data is

$$RS_{app} = \iint_D \left| z(x,y) - \hat{z}(x,y) \right| dxdy \tag{2.19}$$

where D is the domain over which the functional data are defined. Likewise, the residual sum between the baseline and threshold functional data is

$$RS_{thresh} = \iint_D \left| z(x,y) - z_{thresh}(x,y) \right| dxdy, \qquad z_{thresh}(x,y) = az(x+b, y+c) \tag{2.20}$$

where a is still the amplitude threshold coefficient and b and c are phase threshold coefficients for x and y respectively. Note that b and c are determined by:

$$b = \min\left(\left| tol_i x_i^{base} \right|\right), \qquad c = \min\left(\left| tol_i y_i^{base} \right|\right) \tag{2.21}$$

The rest of the algorithm remains the same, including the meaning of the validity criteria.

2.3.2 Demonstration of AVASIM Capability

In an effort to demonstrate the capability of AVASIM for both 1D and 2D functional data, the algorithm was applied to the motor maps used in the EV powertrain design problem. Specifically, approximations for the maximum and minimum torque curves and power loss maps were validated against their high-fidelity versions using the 1D and 2D AVASIM formulations, respectively. Since the target points selected in both cases were merely mesh points describing the functional data, a uniform tolerance of $tol_i = 0.10$ was assigned for all points. For similar reasons, the phase threshold coefficients were set to zero, as in Sohns [*Sohns et al.* (2006)], as opposed to the methodology described in Equations (2.17) and (2.21). Additionally, division-by-zero errors were avoided by setting $\delta = 10^{-4}$ for the torque curves and $\delta = 1$ for the power loss map based on experience. Finally, note that the number of target points for the power loss map was not known a priori but rather determined by a subroutine that only included points that were within the torque curve boundaries. A similar subroutine was used to define numerically the domain of integration D for the power loss map, which is also within the torque curve boundaries. The results from AVASIM are shown in Table 2.1, and Figures 2.3 and 2.4 illustrate the accuracy of these functional data approximations visually.

Upon reviewing these results, it is fairly evident that AVASIM reasonably describes the local and global accuracy of the functional data approximations. Specifically, it is seen that the conservative validity criterion is satisfied for all approximations and that the combined error indices for the torque curves and power loss map estimate accuracies of 76.5%, 96.6%, and 58.4%, respectively. Note that the global error indices indicate high global accuracies and are consistent with what is seen visually; however, the local error indices vary significantly and in some cases (e.g., maximum torque curve and power loss map) suggest lower local accuracies than what is seen visually. The relative instability of the E_{local} measure is likely due to issues associated with division by near-zero target points and as such is problem-dependent. However, the E_{global} measure is much more stable, and since global accuracy is often sufficient and desirable in many engineering applications, this can be of benefit. In particular, one can leverage this knowledge and modify the AVASIM formulations such that E_{comb} is not an arithmetic mean of E_{local} and E_{global}, but rather a weighted sum,

$$E_{comb} = w_{local} E_{local} + w_{global} E_{global} \tag{2.22}$$

where w_{local} and w_{global} are nonnegative weights whose sum must always equal 1. This new formulation is referred to as generalized AVASIM [*Alexander and Papalambros* (2010)] since it enables users to allocate the importance of each accuracy component when computing the combined error index. The work in later chapters will demonstrate how such flexibility could have important implications when using AVASIM as a consistency measure within an ATC framework.

Table 2.1 AVASIM Results for Functional Data Approximations

Index	Max-Torque	Min-Torque	Power Loss
E_{local}	0.588	0.969	0.319
E_{global}	0.942	0.963	0.849
E_{comb}	0.765	0.966	0.584

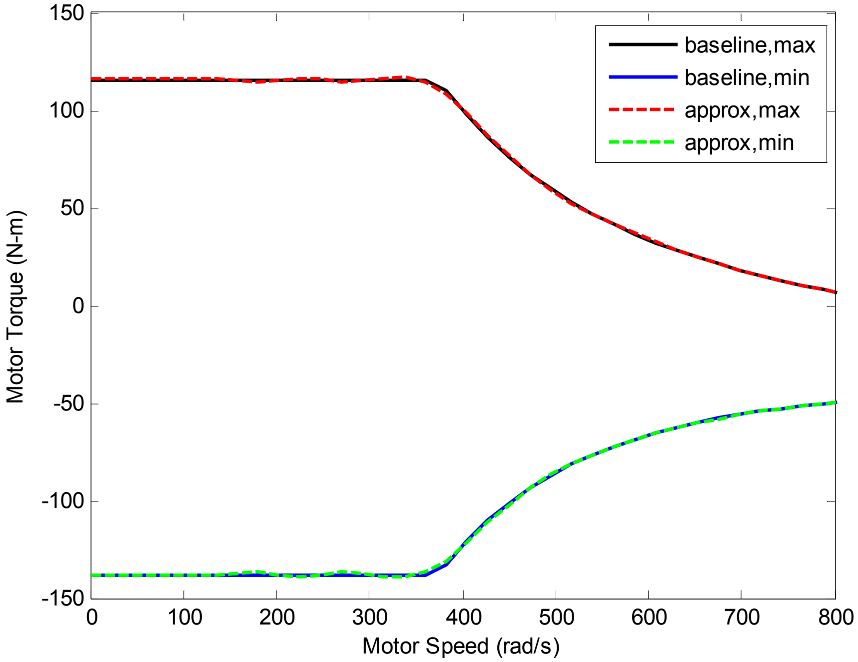

Figure 2.3 Torque Curve Comparison

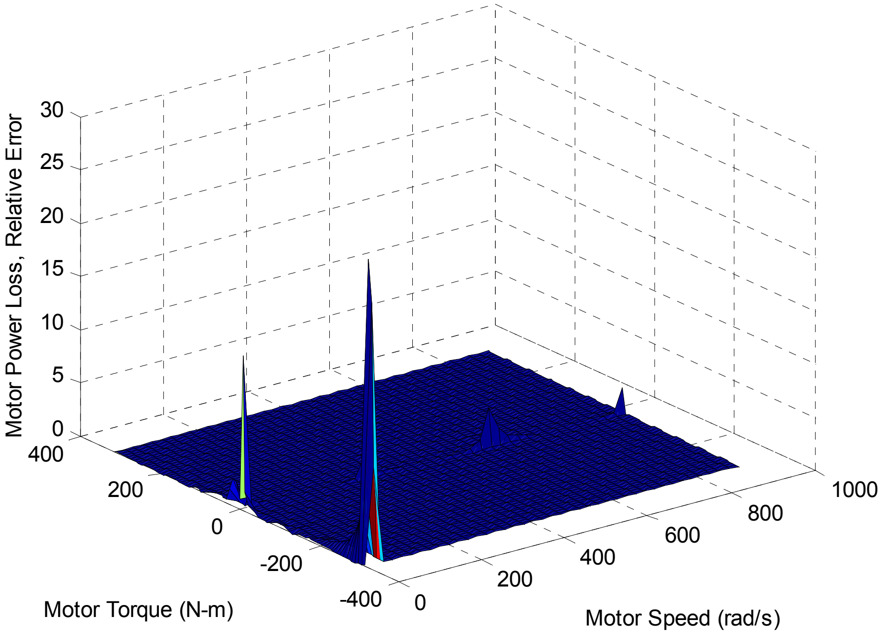

Figure 2.4 Power Loss Map Relative Error

2.4 Summary

This chapter discussed the details of ATC, POD, and AVASIM that are necessary to comprehend the procedures and results for the case studies in Chapters 4-7. In particular, a deeper explanation was provided for the selection of ATC as a decomposition-based optimization strategy, along with its partitioning and coordination approach; two solution strategies for POD based on the number of samples were discussed; and three formulations of AVASIM were reviewed, with the capability of the first two formulations demonstrated through a relevant example. The theory presented in this chapter will be routinely referred to when conducting studies exploring the use of functional data as decision variables in a decomposition-based optimization framework.

Chapter 3

Electric Vehicle Powertrain Models

Electric vehicles (EVs) are increasingly being considered as a viable alternative to conventional vehicles with internal combustion engines in order to reduce the consumption of non-renewable energy resources and emissions of greenhouse gases. For example, by the end of 2010, Nissan will introduce the first large-scale produced EV, the LEAF, in Japan, the United States, and Europe [*Nissan Zero Emission Website* (2010)]. The fact that EVs have existed for decades (albeit in a limited capacity) and that mass-production of such vehicles are emerging as of late only highlights the limited design experience in this domain. Such disparity of sufficient EV design knowledge makes the use of simulation-based design software attractive. These tools enable the exploration of preliminary system design through the proper integration of powertrain components that meet overall vehicle design targets effectively. Therefore, this chapter describes the models used to explore the EV powertrain design problem in both commercial and military vehicle applications.

3.1 Commercial Electric Vehicle Powertrain Model

The commercial electric vehicle powertrain model treated in this dissertation was initially developed by Allison [*Allison* (2008)] in a MATLAB®/Simulink® environment. A general plan view of the vehicle configuration can be seen in Figure 3.1. The model is for a two-passenger, mini-compact vehicle designed primarily for urban driving with some highway speed capability. This classification is evident by the vehicle's overall dimensions, which includes a wheelbase of L = 1.80 m and a track width of W = 1.27 m. The vehicle is powered by a lithium-ion battery energy storage system, which can vary in length, width, and longitudinal location relative to the front end of the battery compartment such that it lies within the dashed region defined by $b_{\ell,max}$ = 1.05 m and width $b_{w,max}$ = 1.20 m. Two electric traction motors drive the rear wheels through a synchronous belt drive system and are mounted at the pivots on the rear suspension trailing arms in an effort to minimize the unsprung mass in the system. A MacPherson strut configuration is used for the front suspension, and finally, low rolling resistance P145/70R12 tires are used to minimize energy consumption.

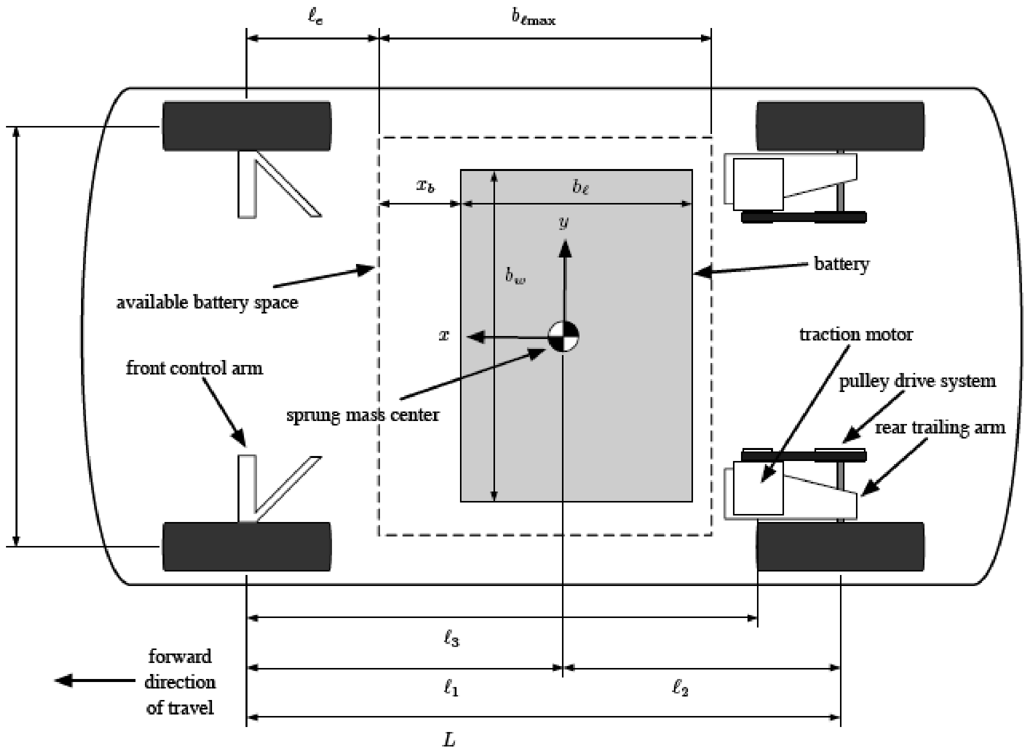

Figure 3.1 General Plan View of Commercial EV [*Allison* (2008)]

Because the case studies in this dissertation explore powertrain design exclusively, several modifications [*Alexander* (2008)] were made to the original analysis models within this simulation-based environment. The structural analysis model, for example, was held constant and thus excluded from the subsequent design problem. The original powertrain analysis model was decomposed into three separate entities: an electric traction motor analysis model, a battery size analysis model, and a vehicle-level analysis model. Any remaining input/output variables from the original powertrain analysis model (e.g., suspension variables) that were unaccounted for during decomposition were treated as parameters for a nominal vehicle design. Finally, a new analysis model was developed [*Alexander et al.* (2010c)] to account for motor mass property changes during design studies. The current analysis models are defined as:

$$[\mathbf{z}_{max}, \mathbf{z}_{min}, \mathbf{z}_{pLoss}, \omega_{max}, J_r] = \mathbf{f}_{motor}(\ell_s, r_m, n_c, R_r) \tag{3.1}$$

$$[m_m, I_{ym}, I_{zm}, y_m] = \mathbf{f}_{motorMass}(\ell_s, r_m) \tag{3.2}$$

$$[b_{\boldsymbol{\ell}}, b_w, m_{batt}] = \mathbf{f}_{battSize}(B_I, B_W, B_L) \tag{3.3}$$

$$[m_s, I_y, I_z, \boldsymbol{\ell}_1, h, b_{w,V}, b_{\boldsymbol{\ell},V}] = \mathbf{f}_{evMass}(x_{batt}, b_{\boldsymbol{\ell}}, b_w, m_{batt}, m_m, I_{ym}, I_{zm}, y_m) \tag{3.4}$$

$$\begin{aligned}[mpg_e, t_{60}, \tau_V, \omega_V, R, P_V, C_b] = \mathbf{f}_v(B_I, B_W, B_L, m_{batt}, m_s, I_y, \boldsymbol{\ell}_1, \cdots \\ h, p_r, \mathbf{z}_{max}, \mathbf{z}_{min}, \mathbf{z}_{pLoss}, \omega_{max}, J_r)\end{aligned} \tag{3.5}$$

Here, the functions $\mathbf{f}_{motor}$, $\mathbf{f}_{motorMass}$, $\mathbf{f}_{battSize}$, $\mathbf{f}_{evMass}$, and $\mathbf{f}_v$ correspond to the electric traction motor, motor mass, battery size, EV mass, and vehicle-level analysis models, respectively. The input/output variables for $\mathbf{f}_{motor}$ include the stack length ℓ_s, the rotor radius r_m, the number of turns per stator coil n_c, the rotor resistance R_r, the VVCVs representing the maximum torque curve $\mathbf{z}_{max}$, minimum torque curve $\mathbf{z}_{min}$, and power loss map $\mathbf{z}_{pLoss}$, the maximum motor speed ω_{max}, and the rotor moment of inertia J_r. The input variables to $\mathbf{f}_{motorMass}$ are shared with $\mathbf{f}_{motor}$, while the output variables include the motor mass m_m, the motor pitch inertia I_{ym}, the motor yaw inertia I_{zm}, and the lateral center of mass location of the motor y_m. Note that $\mathbf{f}_{motorMass}$ could be combined with $\mathbf{f}_{motor}$; however, it is also desired to keep the model parameters of $\mathbf{f}_{motor}$ independent of the vehicle configuration, and so $\mathbf{f}_{motorMass}$ is made distinct from $\mathbf{f}_{motor}$ since y_m is vehicle-dependent. The input/output variables for $\mathbf{f}_{battSize}$ are the battery electrode insertion scale

B_I, the battery cell width scale B_W, the number of cell windings B_L, the battery length b_ℓ, the battery width b_w, and the battery mass m_{batt}. With the exception of the battery compartment clearance x_{batt}, all of the input variables to $\mathbf{f}_{evMass}$ are coupled with the output variables of $\mathbf{f}_{battSize}$ and $\mathbf{f}_{motorMass}$. The output variables from $\mathbf{f}_{evMass}$ are the sprung mass m_s, the sprung mass pitch inertia I_y, the sprung mass yaw inertia I_z, the longitudinal center of mass location of the sprung mass $\boldsymbol{\ell}_1$, the vertical center of mass location of the sprung mass h, and the battery width and length packaging constraint violations $b_{w,V}$ and $b_{\ell,V}$, respectively. Similarly, all of the input variables to $\mathbf{f}_v$ are either shared with $\mathbf{f}_{battSize}$ or coupled with $\mathbf{f}_{motor}$, $\mathbf{f}_{battSize}$, and $\mathbf{f}_{evMass}$ with the exception of the belt drive ratio p_r. The output variables from $\mathbf{f}_v$ include the gasoline-equivalent fuel economy mpg_e, the 0-60 mph time t_{60}, the motor torque and speed constraint violations τ_V and ω_V, the vehicle range R, the battery power constraint violation P_V, and the battery capacity C_b, which indirectly constrains battery cost. Figure 3.2 illustrates the relationships among the analysis models. Observe that the dashed boxes in the figure indicate the problem decomposition for ATC design optimization.

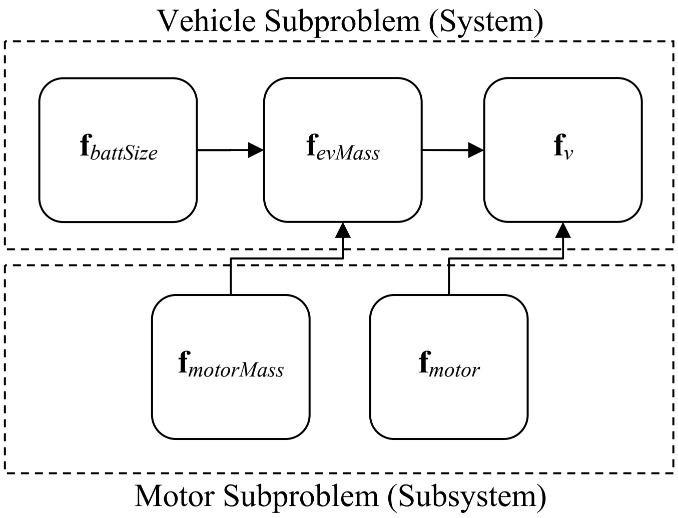

Figure 3.2 Commercial EV Analysis Model Relationships/Problem Decomposition

The remainder of this section presents the details of these analysis models, including the manner in which the input quantities are used to compute the output quantities. As with any optimization problem, a thorough understanding of the modeled system is essential in order to reasonably interpret results from the design study.

3.1.1 Electric Traction Motor Analysis Model

Electric motors are devices that transform electrical power into rotational mechanical power through the interaction of their stator and rotor magnetic fields. Because the current application involves vehicle propulsion, these motors are specifically referred to as electric traction motors. The main components of electric traction motors are the stator, the rotor, and the output shaft connected to the rotor (Figure 3.3). The stator encloses both the rotor and a portion of the output shaft and is usually supplied with three-phase AC power that corresponds to its three-phase windings [*Bose* (2002)]. A rotating magnetic field is generated by the stator when the power is supplied, and this in turn interacts with the magnetic field of the rotor, causing it to spin. In this work, an AC induction motor (IM) model is selected, which uses a rotor comprised of stacked iron sheets inserted with bars of conductive material that are parallel to the output shaft (Figure 3.3). The electric traction motors are just part of the complete drive system, which includes a power inverter and a controller. However, these latter elements are excluded from the model for the sake of simplicity.

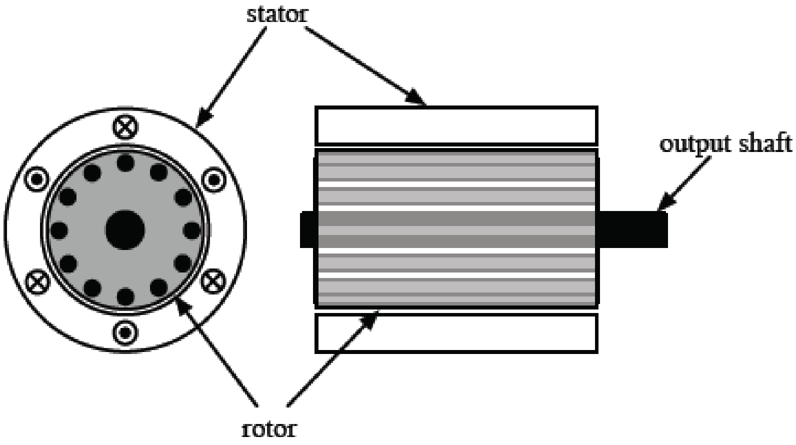

Figure 3.3 Diagram of Electric Traction (Induction) Motor [*Allison* (2008)]

3.1.1.1 Equivalent Electrical Circuit Model

The behavior of a single phase of the electric traction motor is characterized by the equivalent electrical circuit model in Figure 3.4 [*Bose* (2002)]. Here, V_s is the AC power source in terms of root-mean-square (RMS) voltage, L_m is the mutual inductance between the stator and rotor, R_s is the winding resistance of the stator, L_{ls} and L_{lr} are the leakage inductances of the stator and rotor respectively, and R_r is the variable electric resistance through the conductive bars in the rotor. The electromagnetic interaction between the stator and rotor is modeled by dividing the slip s into R_r. Slip, as defined in this model, is the difference between the rotation of the stator and rotor magnetic fields relative to the rotation of the stator magnetic field [*Bose* (2002)]:

$$s = \frac{\omega_e - \omega_{rot}}{\omega_e} \tag{3.6}$$

In the above, ω_e denotes the stator supply frequency that determines the rotational speed of the stator's magnetic field, and ω_{rot} denotes the rotor electrical speed that determines the rotational speed of the rotor's magnetic field. It should be observed that slip induces torque [*Bose* (2002)]. Therefore, when $s = 0$, the motor produces no torque and achieves synchronous (no-load) speed, and when $s = 1$, the motor becomes completely stalled. For $0 < s < 1$, the output torque increases until it reaches the breakdown torque, after which it gradually decreases to the stalled condition.

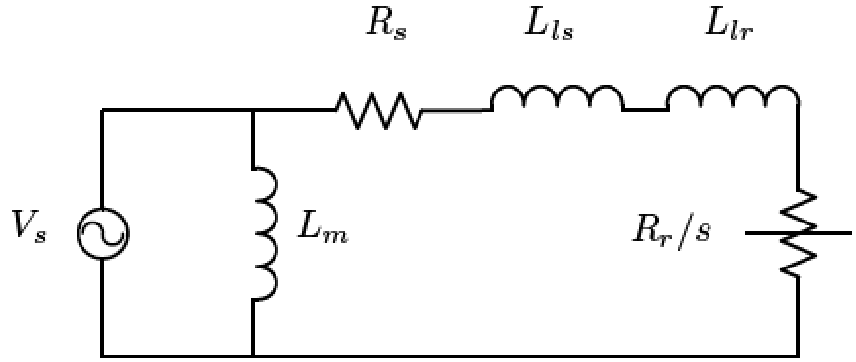

Figure 3.4 Equivalent Circuit Model of IM, Single Phase [*Bose* (2002)]

3.1.1.2 Determination of Induction Motor Properties

The input variables to the electric traction motor analysis model (ℓ_s, r_m, n_c, R_r) along with the parameters listed in Table 3.1 are used to calculate important properties of the IM. The rotor mass, for example, is given by

$$m_r = \pi r_m^2 \ell_s \rho_{fe} \tag{3.7}$$

and is used to compute the rotor moment of inertia, which is one of the outputs of the analysis model:

$$J_r = \frac{m_r r_m^2}{2} \tag{3.8}$$

The torque loss on the output shaft due to friction in the bearings is

$$\tau_{loss}(J_r) = c_m \omega_m \tag{3.9}$$

where c_m is the viscous friction coefficient and ω_m is the rotational speed of the output shaft in radians per second. The friction coefficient is a function of J_r as given by the following empirical relation [*Allison* (2008)]:

$$c_m = C_{m1}\left(1 - \frac{C_{m2}}{e^{C_{m3}J_r}}\right) + C_{m4}J_r \tag{3.10}$$

The output shaft speed is computed using ω_{rot}, which in turn is found by rearranging Equation (3.6) in terms of ω_e and s:

$$\omega_{rot} = \omega_e(1 - s) \tag{3.11}$$

$$\omega_m = 2\omega_{rot} / p \tag{3.12}$$

Next, the number of stator slots N_s, the stator windings per phase W_1, and the effective air gap δ_g (accounting for geometry and slot effects) are found using the following equations:

$$N_s = 2p_1 q m_1 \tag{3.13}$$

$$W_1 = 2p_1 q n_c \tag{3.14}$$

$$\delta_g = 0.06 r_m - 0.0025 \tag{3.15}$$

In the above, p_1 is the number of pole pairs in the stator, which is half of the number of stator poles p. Using these values, the mutual inductance can be calculated as [*Amin* (2001)]:

$$L_m = \frac{6\mu_0 W_1^2 r_m \ell_s}{\pi\, p_1^2 \delta_g} \tag{3.16}$$

The stator leakage inductance is estimated using the following empirical relationship derived by Allison [*Allison* (2008)]:

$$L_{ls} = L_m \left(0.07 - \frac{0.05}{1 + e^{(5.0 - \ell_s / r_m)/2}} \right) \tag{3.17}$$

It is assumed that the rotor leakage inductance is equal to the stator leakage inductance, which results in a total leakage inductance of:

$$L_l = L_{ls} + L_{lr} = 2L_{ls} \tag{3.18}$$

From here, the winding radius of the stator is calculated, assuming that the outer stator radius r_s is proportional to the rotor radius by a factor t_s [*Allison* (2008)]:

$$r_w = \sqrt{\frac{n_a n_p \left(r_s^2 - r_m^2\right)}{W_1 m_1}} = r_m \sqrt{\frac{n_a n_p \left(\left(t_s + 1\right)^2 - 1\right)}{W_1 m_1}} \tag{3.19}$$

The total winding length is:

$$\ell_w = 2\ell_s W_1 \tag{3.20}$$

Using these latter two properties, the stator winding resistance can be expressed as:

$$R_s = \frac{k_e \rho_{cu} \ell_w}{\pi r_w^2} \tag{3.21}$$

Finally, the maximum stator current I_{sm} of the IM has been fit to the following quadratic model [*Allison* (2008)]:

$$I_{sm} = C_{I1} + C_{I2} d_w + C_{I3} d_w^2 \tag{3.22}$$

Observe that in the above expression, d_w represents the winding diameter of the stator in millimeters and is given by $d_w = 2000 r_w$.

Table 3.1 Estimated Values of IM Parameters for Commercial EV [*Allison* (2008)]

Parameter	Description	Value
V_{sm}	Maximum stator voltage	460 V
p	No. of stator poles	4
q	No. of slots per phase per pole	3
m_1	No. of motor phases	3
σ_{Yr}	Rotor yield stress	300 MPa
ν	Rotor Poisson ratio	0.30
SF	Rotor safety factor	4
ω_{inv}	Maximum inverter frequency	1510 rad/s
ρ_{fe}	Iron density	7870 kg/m^3
C_{m1}	1st c_m parameter	0.062
C_{m2}	2nd c_m parameter	0.998
C_{m3}	3rd c_m parameter	0.94
C_{m4}	4th c_m parameter	0.0513
n_a	Slot volume ratio	0.8
n_p	Wire packaging ratio	0.5
t_s	Stator radius proportionality factor	0.3
k_e	End effect ratio	1.5
ρ_{cu}	Copper resistivity	1.72 x 10^{-8} Ω-m
C_{I1}	Constant I_{sm} parameter	0.0564
C_{I2}	Linear I_{sm} parameter	-0.0237
C_{I3}	Quadratic I_{sm} parameter	2.21

3.1.1.3 Development of Induction Motor Performance Curves

The IM performance curves include maximum and minimum torque curves and a power loss map that are initially generated by calculating the breakdown torque and power requirements at non-uniformly-spaced points in a torque-speed coordinate system. These calculated values are then used to interpolate the final performance curves as denoted by $\mathbf{z}_{max}$, $\mathbf{z}_{min}$, and $\mathbf{z}_{pLoss}$ over a prescribed, evenly-spaced mesh [*Allison* (2008)]. Because the torque curves set physical boundaries on the operating conditions of the motor, they must be generated first. Figure 3.5 illustrates some typical characteristics of these curves as well as the motor behavior within their specified boundaries. Note that the developed torque τ_e does not include mechanical losses; therefore, the stator supply frequency ω_e, also known as the stator electrical speed, is shown in the figure instead of the output shaft speed ω_m. The region between the maximum torque curve τ_{em} and the ω_e-axis denotes the forward motoring operating condition, whereas the region between the minimum torque curve τ_{emR} and the ω_e-axis denotes the forward regeneration operating condition [*Bose* (2002)]. During forward motoring, the IM functions as a true motor, with ω_{rot} lagging ω_e to produce positive slip. Conversely, during forward regeneration, the IM functions as a generator, with ω_e lagging ω_{rot} to produce negative slip. The reverse motoring and reverse regeneration operating conditions are excluded since only forward drive cycles are used in the design studies.

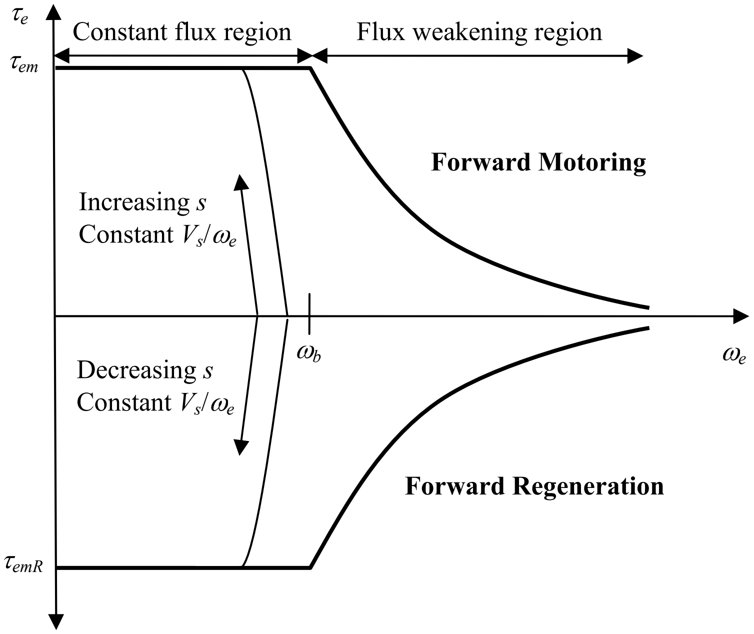

Figure 3.5 Typical IM Maximum/Minimum Torque Curves [*Allison* (2008)]

The maximum and minimum torque curves are generated by calculating their respective breakdown torques τ_{em} and τ_{emR} at all mesh points corresponding to ω_e:

$$\tau_{em} = \frac{3p}{4\omega_e} \cdot \frac{V_s^2}{\sqrt{R_s^2 + \omega_e^2 L_\ell^2} + R_s} \tag{3.23}$$

$$\tau_{emR} = -\frac{3p}{4\omega_e} \cdot \frac{V_s^2}{\sqrt{R_s^2 + \omega_e^2 L_\ell^2} - R_s} \tag{3.24}$$

Although the above equations do not include mechanical losses, the net breakdown torques $\tau_{em,net} = \tau_{em} - \tau_{loss}$ and $\tau_{emR,net} = \tau_{emR} - \tau_{loss}$ do account for these losses and are reflected in $\mathbf{z}_{max}$ and $\mathbf{z}_{min}$. Since it is known that the stator magnetic flux is proportional to the ratio V_s/ω_e [*Bose* (2002)], the torque curves can be divided into a constant flux sub-region and a flux weakening sub-region (Figure 3.5). In the constant flux sub-region, the ratio V_s/ω_e is given by a constant C_1, which yields nearly constant net breakdown torque. Such a condition is limited only by the relatively small frictional losses that increase with speed as indicated in Equation (3.9). However, in the flux weakening sub-region, the IM operates at maximum stator voltage V_{sm} and the ratio V_s/ω_e decreases as ω_e increases (since $V_s = V_{sm}$). This results in decreasing breakdown torque during forward motoring and increasing breakdown torque during forward regeneration.

The speed at which these two sub-regions are divided is known as the base speed ω_b. Physically, this corresponds to the speed at which the stator current I_s attains its maximum value I_{sm} (as given by Equation (3.22)) when $V_s = V_{sm}$. It is also used to compute the flux constant C_1 and to obtain a linear relation for V_s in the constant flux sub-region such that the net torque remains constant. The base speed is determined numerically through a root-finding procedure ($\omega_b = \{\omega_e \mid f(\omega_e) = I_s(\omega_e) - I_{sm} = 0\}$) that requires the calculation of the stator current. This is determined through circuit analysis of Figure 3.4, which in turn requires the calculation of total circuit impedance. First, the impedance of L_m is given by

$$Z_1 = jL_m\omega_e \tag{3.25}$$

where $j = \sqrt{-1}$ denotes the imaginary number. The equivalent impedance of R_s, $L_{\ell s}$, $L_{\ell r}$, and R_r/s in series is:

$$Z_2 = (R_s + R_r / s) + j\omega_e (L_{\ell s} + L_{\ell r}) \tag{3.26}$$

Because Z_1 and Z_2 are in parallel, the total circuit impedance Z_T is calculated as:

$$Z_T = \frac{Z_1 Z_2}{Z_1 + Z_2} \tag{3.27}$$

Finally, the stator current is calculated by taking the magnitude of Z_T and dividing it into the stator voltage:

$$I_s = \frac{V_s}{|Z_T|} \tag{3.28}$$

Therefore, the base speed can be obtained by solving $\omega_b = \{\omega_e \mid f(\omega_e) = I_s(\omega_e) - I_{sm} = 0\}$ for $V_s = V_{sm}$ in Equation (3.28) and $s = s_m$ in Equation (3.26), which is the slip at breakdown torque:

$$s_m = \frac{R_r}{\sqrt{R_s^2 + \omega_e^2 L_\ell^2}} \tag{3.29}$$

Observe that Equation (3.29) applies for forward motoring; for forward regeneration, a negative sign would need to be included. The base speed enables the direct computation of the flux constant C_1 [*Bose* (2002)]:

$$C_1 = V_{sm} / \omega_b \tag{3.30}$$

Additionally, ω_b is used in the development of a linear relation for V_s in the constant flux sub-region,

$$V_s = \frac{\omega_e \left(V_{sm} - V_{adj}\right)}{\omega_b} + V_{adj} \tag{3.31}$$

where V_{adj} is a voltage adjustment coefficient that is determined numerically through a root-finding procedure. In particular, Equation (3.31) is substituted into Equation (3.23) for the breakdown torque τ_{em} at a fixed $\omega_e < \omega_b$, which must be matched to the net breakdown torque $\tau_{em,net}$ at $\omega_e = \omega_b$ and $V_s = V_{sm}$ to ensure constant net torque in the constant flux sub-region. The voltage adjustment coefficient V_0 for the maximum torque curve is then defined as $V_0 = \{V_{adj} \mid f(V_{adj}) = \tau_{em}(V_{adj}) - \tau_{em,net} = 0\}$. A similar procedure is followed for the voltage adjustment coefficient V_{0R} for the minimum torque curve.

After constructing the torque curves through their net breakdown torques, the power loss map can finally be constructed. This requires intermediate calculations of the total circuit impedance, stator voltage, and stator current as described in Equations (3.26-3.28) and Equation (3.31) for the constant flux sub-region:

$$0^+ \le \omega_e \le \omega_b, \quad 0^+ \le s \le s_m \quad (\textit{forward motoring}) \tag{3.30}$$

$$0^+ \le \omega_e \le \omega_b, \quad 0^- \ge s \ge -s_m \quad (\textit{forward regeneration}) \tag{3.31}$$

Note that the superscript plus and minus signs indicate values slightly above and below zero, respectively, to avoid numerical issues. The power losses are computed as power input requirements to the IM [*Bose* (2002)]:

$$P_{in} = m_1 I_s V_s \cos\left(\angle Z_T\right) \tag{3.32}$$

In this equation, the cosine of the angle of Z_T denotes the power factor, which accounts for the effects of the inductive elements on power consumption. For forward regeneration, observe that P_{in} is negative and denotes power output capabilities. The power losses are calculated in a similar fashion for the flux weakening sub-region

$$\omega_b < \omega_e \le \omega_{e,max}, \quad 0^+ \le s \le s_m \quad (\mathit{forward\ motoring}) \tag{3.33}$$

$$\omega_b < \omega_e \le \omega_{e,max}, \quad 0^- \ge s \ge -s_m \quad (\mathit{forward\ regeneration}) \tag{3.34}$$

with the exception that the stator voltage is a constant $V_s = V_{sm}$ and hence does not need to be computed. Note that the upper bound on the electrical speed $\omega_{e,max}$ is "sufficiently large" [*Allison* (2008)] and is determined empirically. Figure 3.6 shows a sample motor map, complete with torque curves and power loss isocontours, for the IM.

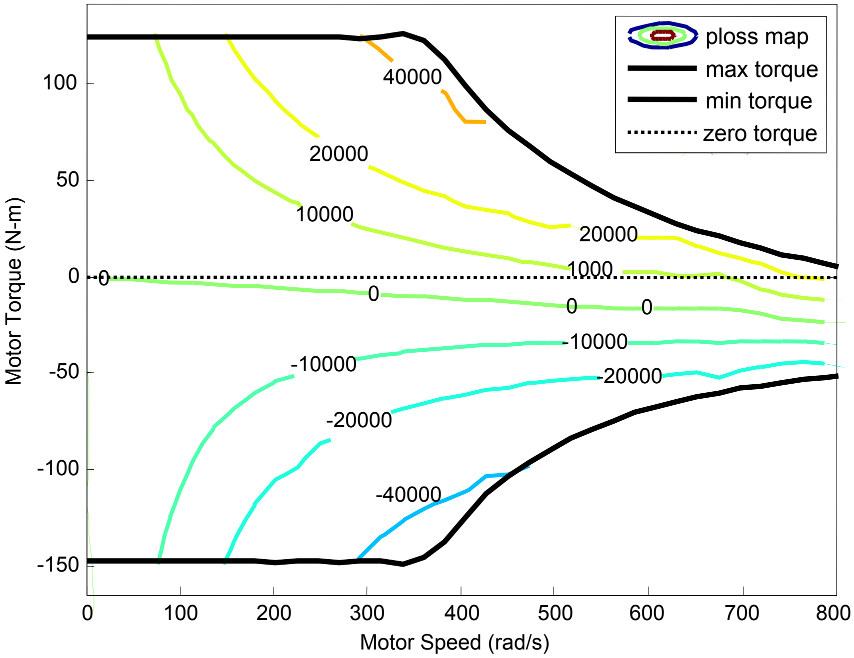

Figure 3.6 Sample Motor Map for IM

The final output from the electric traction motor analysis model is the maximum motor speed ω_{max}. For a given motor design, ω_{max} is determined by one of the following three criteria:

$$\omega_{max1} = \{\omega_m \mid \tau_{em,net}(\omega_m) = 0\} \tag{3.35}$$

$$\omega_{max2} = \sqrt{\frac{8\sigma_{Yr}}{SFr_m^2\rho_{fe}(3+\nu)}} \tag{3.36}$$

$$\omega_{max3} = 2\omega_{inv} / p \tag{3.37}$$

The first criterion ω_{max1} indicates that ω_{max} is limited by motor viscous drag and corresponds to the speed at which the maximum torque curve intersects the ω_m-axis. The second criterion ω_{max2} indicates that ω_{max} is the speed beyond which the structural integrity of the motor would diminish. The last criterion ω_{max3} indicates that ω_{max} is the speed beyond which the power inverter would be incapable of supplying a higher electrical frequency. Therefore, ω_{max} is selected as the minimum of these three criteria [*Bose* (2002)].

Another quantity of interest that is generated by the electric traction motor analysis model but is not used in this work is the efficiency map. In the forward motoring operating condition, the efficiency map is constructed by calculating the motor power output P_{out} over the speed and slip domains given by Equations (3.30) and (3.33) and dividing it by P_{in}:

$$\eta = P_{out} / P_{in} \tag{3.38}$$

The same procedure is performed in the forward regeneration operating condition over the speed and slip domains given by Equations (3.31) and (3.34), with the exception that the numerator and denominator in Equation (3.38) are switched. The power output is simply the product of the net developed torque $\tau_{e,net} = \tau_e - \tau_{loss}$ and ω_m, which involves an intermediate calculation of the developed torque:

$$\tau_e = \frac{3pR_r}{2s\omega_e} \cdot \frac{V_s^2}{(R_s + R_r / s)^2 + \omega_e^2 L_\ell^2} \tag{3.39}$$

Hence, the efficiency map can be generated with the power loss map concurrently.

3.1.2 Motor Mass Analysis Model

The motor mass analysis model is based in part on a model by Cuenca, Gains, and Vyas [*Cuenca et al.* (1999)] and was updated using scaled estimates for a similar motor type at Raser Technologies, Inc.'s corporate website [*Raser Technologies, Inc.* (2010)]. This was necessary in order to properly reflect current mass-reducing technologies. Because the updated model indicates that the ratio between the rotor mass m_r and the total mass m_m is approximately 0.90, the motor mass can be computed simply by dividing this ratio into the rotor mass as given in Equation (3.7):

$$m_m = m_r / 0.90 \tag{3.40}$$

Continuing with the assumption that the motor can be approximated geometrically as a solid cylinder, the motor pitch inertia I_{ym} and the motor yaw inertia I_{zm} can be calculated as

$$I_{ym} = \frac{m_m r_M^2}{2} \tag{3.41}$$

$$I_{zm} = \frac{m_m \left(3r_M^2 + \ell_M^2\right)}{12} \tag{3.42}$$

where the y-axis is parallel to the output shaft, the z-axis is perpendicular to the output shaft, and r_M and ℓ_M refer to the overall motor radius and length, respectively. These intermediate quantities are estimated as the following:

$$r_M = 1.9 r_m \tag{3.43}$$

$$\ell_M = 2\ell_s \tag{3.44}$$

Finally, the lateral center of mass location of the motor y_m (accounting for the clearance between the motor and the tire) is calculated as

$$y_m = \frac{W}{2} - \left(\frac{\ell_M}{2} + 0.1524 \right) \tag{3.45}$$

where $W = 1.27$ m is the track width of the vehicle.

3.1.3 Battery Size Analysis Model

The battery size analysis model is part of a simulation-based battery model for a lithium-ion battery chemistry that represents the energy storage system (ESS) for the EV. Specifically, this ESS harnesses electrical energy through a chemical reaction process and uses it for vehicle propulsion. Critical auxiliary functions, such as power steering and air conditioning, are also powered through the ESS [*Allison* (2008)]. The complete battery model has been developed by Han [*Han* (2008)] based on the work of Doyle, Fuller, and Newman [*Doyle et al.* (1993); *Fuller et al.* (1994)] and is dynamic to account for changes in the state of charge (SOC) as well as charging and discharging limits during simulation. In this section, only the physical characteristics of the battery, such as the length, width, and mass, are addressed; the performance-related characteristics will be discussed later in the vehicle-level analysis model as they directly impact its output quantities. All characteristics, however, are determined by battery design variables that are geometric scaling factors of battery cell components.

3.1.3.1 Battery Model: Physical Characteristics

The battery model consists of two battery pack pairs, with each pair containing battery packs placed in series. The battery pack pairs themselves are placed in parallel. Each pack consists of four battery modules placed in series, and each module consists of twelve battery cells placed in series [*Allison* (2008)]. Within these cells, a chemical reaction between the positive and negative electrodes occurs, which yields electrical energy [*Scrosati* (1992)]. Figure 3.7 shows a typical cell cross-section as well as its overall dimensions qualitatively.

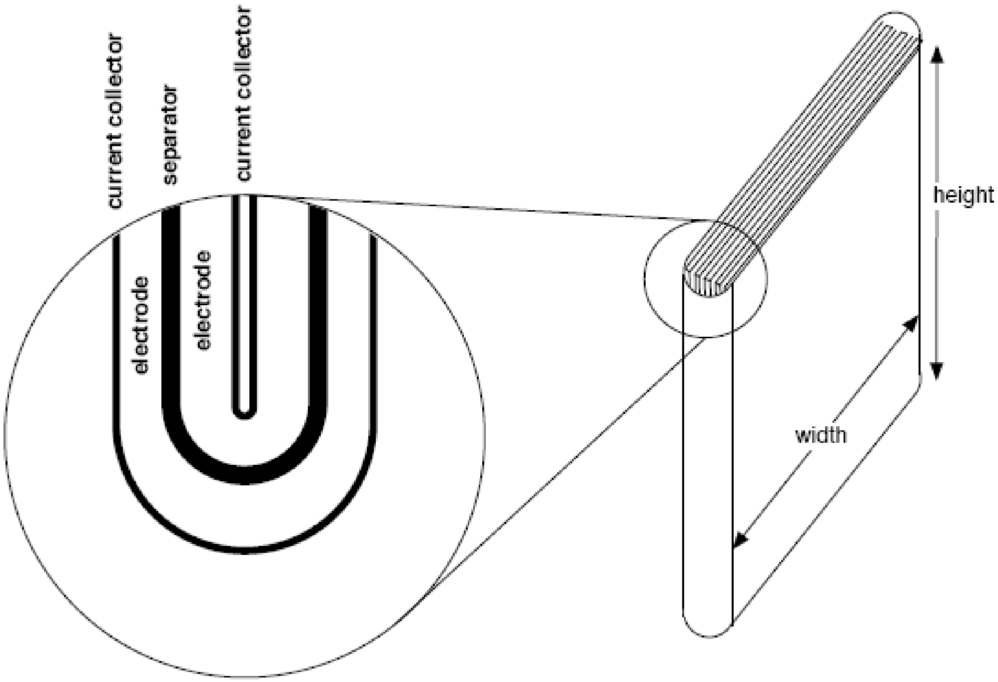

(a) Cell widings

(b) Flat-wound lithium-ion cell

Figure 3.7 Typical Flat-Wound Lithium-Ion Battery Cell [*Han* (2008)]

It should be observed that the rate of the chemical reaction in the separator is significantly affected by the material composition of the battery and the cell geometry. Assuming that the material composition in this model is fixed, it is possible to characterize changes in the battery's electrochemical process as well as its physical size through scaling factors of cell geometric-related variables [*Allison* (2008)]. The battery electrode insertion scale B_I, for example, determines the thickness of the electrodes and the separator. The battery cell width scale B_W determines the electrode and cell width as defined by Figure 3.7. Because the battery is mounted transversely in the EV, this variable ultimately affects the overall battery length b_ℓ. The final input variable B_L determines the number of windings, or folds, within the cell. This variable, along with

B_I, affects the overall battery width b_w. Only the cell height remains constant, which ultimately translates to a fixed overall battery height of 11 cm [*Allison* (2008)].

3.1.3.2 Overall Battery Size and Mass

In an effort to minimize computational expense, three RBF ANNs based on a hybrid pulse power characterization (HPPC) test [*PNGV Battery Test Manual Revision 3* (2001)] within the complete battery model have been developed and used to evaluate the battery pack width, length, and mass as a function of the input variables B_I, B_W, and B_L. After these quantities have been obtained for a single battery pack, the overall battery length, width, and mass can be determined as [*Allison* (2008)]

$$b_\ell = 2 f_{packWidth}(B_I, B_W, B_L) \tag{3.46}$$

$$b_w = 2 f_{packLength}(B_I, B_W, B_L) \tag{3.47}$$

$$m_{batt} = 4 f_{packMass}(B_I, B_W, B_L) \tag{3.48}$$

where $f_{packWidth}$, $f_{packLength}$, and $f_{packMass}$ are the RBF ANNs associated with the battery pack width, length, and mass. The coefficients in the above equations are based on the fact that the length of the battery is equivalent to the width of two battery packs, the width of the battery is equivalent to the length of two battery packs, and the mass of the battery is equivalent to the total number of battery packs, which is four [*Allison* (2008)].

3.1.4 EV Mass Analysis Model

The vehicle configuration in Figure 3.1 along with the model parameters listed in Table 3.2 provide the basis for the EV mass analysis model. In particular, the model parameters are estimated using a comparable size commercial vehicle known as the Smart Fortwo [*Smart USA* (2010)]. Note that some of the entries in Table 3.2 are termed “baseline” parameters, which indicates that they correspond to a Smart Fortwo vehicle that excludes the mass of the (conventional) powertrain, fuel tank, chassis, and frame. Therefore, the overall EV mass and related properties are computed using these baseline parameters along with the remaining model parameters and input variables that account for the mass of the EV powertrain (battery and motors) as well as its frame. Finally, observe that all longitudinal positions in the model are measured relative to the front axle, all vertical positions are measured relative to the ground, and all lateral positions are measured relative to the vehicle centerline.

Table 3.2 Estimated Values of Commercial EV Mass Analysis Model Parameters

Parameter	Description	Value
m_b	Baseline vehicle mass	423 kg
ℓ_b	Baseline vehicle longitudinal com location	0.935 m
h_b	Baseline vehicle vertical com location	0.610 m
I_{yb}	Baseline vehicle pitch inertia	268 kg-m^2
I_{zb}	Baseline vehicle yaw inertia	829 kg-m^2
m_{fr}	EV frame mass	295 kg
ℓ_{fr}	EV frame longitudinal com location	0.886 m
h_{fr}	EV frame vertical com location	0.632 m
I_{yfr}	EV frame pitch inertia	392 kg-m^2
I_{zfr}	EV frame yaw inertia	447 kg-m^2
$b_{\ell,max}$	Maximum allowable battery length	1.05 m
$b_{w,max}$	Maximum allowable battery width	1.20 m
b_h	Battery height	0.11 m
ℓ_{battc}	Distance to front of battery compartment	0.49 m
h_{batt}	Battery vertical com location	0.355 m
ℓ_m	Motor longitudinal com location	1.50 m
h_m	Motor longitudinal com location	0.45 m

The mass of the EV supported by its suspension, also known as its sprung mass m_s, is simply the sum of the baseline, frame, battery, and motor masses:

$$m_s = m_b + m_{fr} + m_{batt} + 2m_m \tag{3.49}$$

The associated longitudinal and vertical center of mass locations are

$$\ell_1 = \frac{1}{m_s}\left(m_b \ell_b + m_{fr} \ell_{fr} + m_{batt} \ell_{batt} + 2 m_m \ell_m\right) \tag{3.50}$$

$$h = \frac{1}{m_s}\left(m_b h_b + m_{fr} h_{fr} + m_{batt} h_{batt} + 2 m_m h_m\right) \tag{3.51}$$

where the battery longitudinal center of mass location ℓ_{batt} is determined from:

$$\ell_{batt} = \ell_{battc} + x_{batt} + b_\ell / 2 \tag{3.52}$$

Using the results from Equations (3.50)-(3.51), the EV pitch and yaw moments of inertia can be obtained by computing the corresponding moments of inertia of the baseline vehicle, frame, battery, and motors about the EV center of mass and adding them together. This is accomplished through the well-known parallel-axis theorem [*Cook and Young* (1999)]. Therefore, the pitch and yaw moments of inertia of the baseline vehicle about the center of mass are:

$$I_{yb,com} = I_{yb} + m_b\left(\left(\ell_b - \ell_1\right)^2 + \left(h_b - h\right)^2\right) \tag{3.53}$$

$$I_{zb,com} = I_{zb} + m_b\left(\ell_b - \ell_1\right)^2 \tag{3.54}$$

Similarly, the pitch and yaw moments of inertia of the frame about the center of mass are:

$$I_{yfr,com} = I_{yfr} + m_{fr}\left(\left(\ell_{fr} - \ell_1\right)^2 + \left(h_{fr} - h\right)^2\right) \tag{3.55}$$

$$I_{zfr,com} = I_{zfr} + m_{fr}\left(\ell_{fr} - \ell_1\right)^2 \tag{3.56}$$

An intermediate step involving the estimation of the pitch and yaw moments of inertia of the battery about its own center of mass is necessary before performing similar calculations about the EV center of mass. Due to its rectangular geometry, these moments of inertia are computed as:

$$I_{ybatt} = \frac{1}{12} m_{batt} \left(b_{\ell}^2 + b_h^2 \right) \tag{3.57}$$

$$I_{zbatt} = \frac{1}{12} m_{batt} \left(b_{\ell}^2 + b_w^2 \right) \tag{3.58}$$

The pitch and yaw moments of inertia of the battery about the EV center of mass are:

$$I_{ybatt,com} = I_{ybatt} + m_{batt} \left(\left(\ell_{batt} - \ell_1 \right)^2 + \left(h_{batt} - h \right)^2 \right) \tag{3.59}$$

$$I_{zbatt,com} = I_{zbatt} + m_{batt} \left(\ell_{batt} - \ell_1 \right)^2 \tag{3.60}$$

Likewise, the pitch and yaw moments of inertia of each motor about the center of mass are:

$$I_{ym,com} = I_{ym} + m_m \left(\left(\ell_m - \ell_1 \right)^2 + \left(h_m - h \right)^2 \right) \tag{3.61}$$

$$I_{zm,com} = I_{zm} + m_m \left(\left(\ell_m - \ell_1 \right)^2 + y_m^2 \right) \tag{3.62}$$

Finally, the EV pitch and yaw moments of inertia can be calculated as:

$$I_y = I_{yb,com} + I_{yfr,com} + I_{ybatt,com} + 2 I_{ym,com} \tag{3.63}$$

$$I_z = I_{zb,com} + I_{zfr,com} + I_{zbatt,com} + 2 I_{zm,com} \tag{3.64}$$

The last two outputs of the EV mass analysis model are the battery packaging constraint violations $b_{w,V}$ and $b_{\ell,V}$, which are given by [*Allison* (2008)]:

$$b_{w,V} = b_w - b_{w,max} \tag{3.65}$$

$$b_{\ell,V} = x_{batt} + b_\ell - b_{\ell,max} \tag{3.66}$$

3.1.5 Vehicle-Level Analysis Model

The vehicle-level analysis model uses two powertrain simulations followed by two battery simulations to estimate vehicle range, acceleration performance, and energy efficiency for the EV [*Allison* (2008)]. Additionally, these simulations facilitate the computation of constraints related to motor torque and speed capability as well as battery power capability and cost. Because there is no feedback between the powertrain and battery simulations, they can be executed independently. This model simplification allows for significant computational efficiency [*Allison* (2008)]. Because several modifications to the powertrain simulations have been made since the first version of this model, these simulations are described in detail in this dissertation. The battery simulations, however, are discussed from a high-level perspective but can be reviewed in more detail in Han [*Han* (2008)].

3.1.5.1 Powertrain Models

The powertrain simulations have been developed in Simulink® and consist of several submodels that are linked together in both backward-looking and forward-looking models, respectively. The backward-looking model uses a prescribed drive cycle along with analysis model input variables and parameters to predict motor torque, speed, and power requirements at each simulation time step. Motor constraint violations can then be evaluated using these requirements:

$$\tau_V = \max\{\tau_m(t,\omega_m) - \tau_{em,net}(\omega_m),\ \tau_{emR,net}(\omega_m) - \tau_m(t,\omega_m)\} \tag{3.67}$$

$$\omega_V = \omega_m(t) - \omega_{max} \tag{3.68}$$

The motor power requirements, however, are passed as inputs to a battery simulation that facilitates the vehicle range estimation. The forward-looking model uses the same submodels, input variables, and parameters but instead predicts the 0-60 mph acceleration time t_{60} by linearly increasing the velocity of the vehicle from zero at $t = 0$ to 60 mph (26.8 m/s).

Figure 3.8 shows a block diagram of the backward-looking powertrain model, which includes the input drive cycle. The drive cycle selected for the commercial EV powertrain design studies is the simplified federal urban drive schedule (SFUDS), which is a shortened version of the federal urban drive schedule (FUDS) [*Larminie and Lowry* (2003)]. Despite the differences in duration time (360 seconds for SFUDS, 1500 seconds for FUDS), both drive cycles possess the same average speed and maximum acceleration/braking values. A depiction of the SFUDS profile is shown in Figure 3.9.

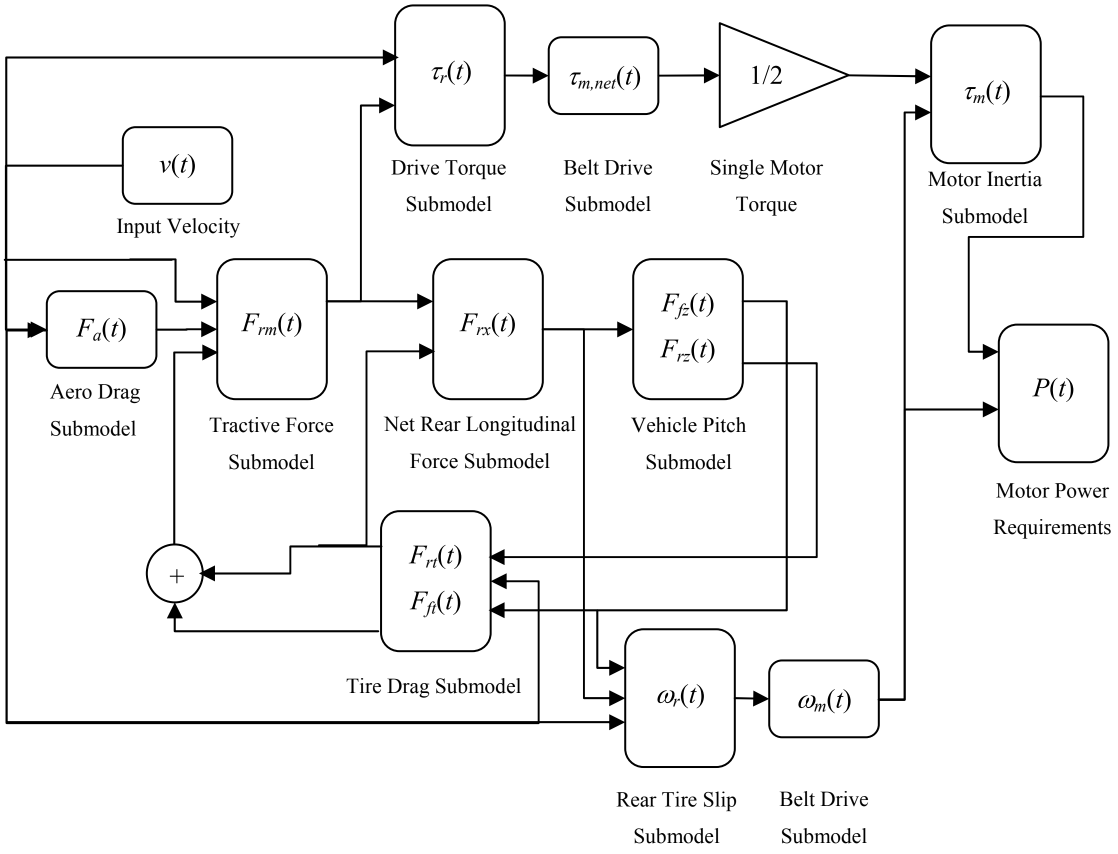

Figure 3.8 Block Diagram of Powertrain Simulation Submodels for Commercial EV

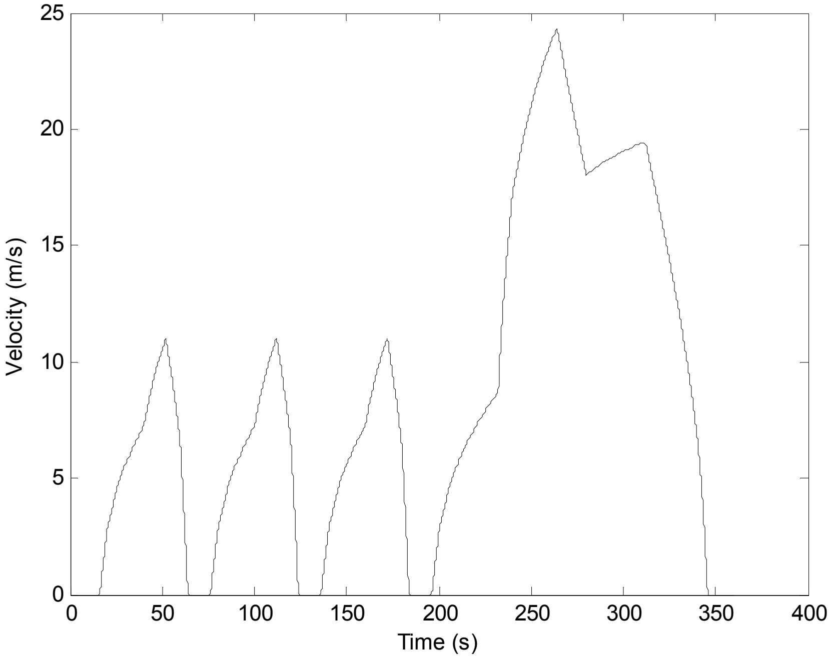

Figure 3.9 SFUDS Profile

Because the same submodels are used in the forward-looking powertrain model, the block diagram of this simulation is excluded. However, both simulations use the same model parameters as listed in Table 3.3. The remainder of this section describes each submodel for both simulations along with any associated assumptions.

Table 3.3 Estimated Values of Powertrain Model Parameters for Commercial EV

Parameter	Description	Value
m_{us}	Unsprung mass	154 kg
c_s	Suspension damping per wheel	800 N-s/m
k_s	Suspension stiffness per wheel	16000 N/m
L	Wheelbase	1.80 m
C_d	Drag coefficient	0.30
A_f	Frontal area	1.70 m^2
ρ_a	Air density	1.20 kg/m^3
r_w	Pulley radius, wheel side	0.16 m
I_{yt}	Tire/wheel assembly spin inertia per axle	0.72 kg-m^2
C_r	Tire rolling resistance	0.0069
C_{t1}	Constant r_t parameter	0.240
C_{t2}	Linear r_t parameter	2.57 x 10^{-7}
C_{t3}	Quadratic r_t parameter	2.55 x 10^{-6}
P_{acc}	Accessory power load	750 W

3.1.5.1.1 Aerodynamic Drag Submodel

The aerodynamic drag force that the vehicle must overcome is proportional to the square of its speed and is given by:

$$F_a(t) = \frac{1}{2} C_d \rho_a A_f v(t)^2 \tag{3.69}$$

3.1.5.1.2 Tractive Force Submodel

The tractive force of the vehicle is the total effort required to move the vehicle at any given instant during the drive cycle. It also represents the total force that the motors must provide (through torque relationships) to achieve vehicle propulsion. Because it is assumed that the vehicle can be characterized through a lumped parameter model, the tractive force of the EV is simply the sum of its inertial force as well as its aerodynamic and tire drag forces:

$$F_{rm}(t) = m_T \dot{v}(t) + F_t(t) + F_a(t) \tag{3.70}$$

In this equation, m_T denotes the total vehicle mass, which is the sum of the m_s and m_{us}, and $F_t(t)$ denotes the total tire drag force, which includes rolling resistance and inertial effects [*Larminie and Lowry* (2003)]. The latter term is the sum of its front and rear components $F_{ft}(t)$ and $F_{rt}(t)$ as indicated in Figure 3.8.

3.1.5.1.3 Drive Torque Submodel

Using the result from Equation (3.70), the total drive torque can be calculated as

$$\tau_r(t) = F_{rm}(t) r_t(v(t)) \tag{3.71}$$

where $r_t(v(t))$ is the dynamically-loaded tire radius. This quantity is estimated empirically through a second-order polynomial model based on a fictitious, low rolling resistance tire that is appropriate for this type of vehicle [*Allison* (2008)]:

$$r_t(v(t)) = C_{t1} + C_{t2} v(t) + C_{t3} v(t)^2 \tag{3.72}$$

3.1.5.1.4 Net Rear Longitudinal Force Submodel

The net longitudinal force on the rear tires is required as an input to the vehicle pitch and rear tire drag submodels. This quantity is simply found by applying force balance on the rear tires:

$$F_{rx}(t) = F_{rm}(t) - F_{rt}(t) \tag{3.73}$$

3.1.5.1.5 Vehicle Pitch Submodel

Since the vehicle pitch motion is dynamically coupled with several intermediate quantities used in the powertrain simulation, a submodel has been included to capture this behavior [*Allison* (2008)]. Figure 3.10 shows the two degree-of-freedom (DOF) model that provides the basis for the vehicle pitch submodel. Specifically, the vehicle pitch motion is characterized by its vertical displacement $z(t)$ from the static, vertical center of mass location h and its pitch angle $\theta_p(t)$. The key intermediate quantities that are necessary for other submodels are the front and rear suspension forces $F_{fz}(t)$ and $F_{rz}(t)$. These forces account for both stiffness and damping effects in the suspension. Finally, note that $\ell_2 = L - \ell_1$ is the longitudinal distance from the center of mass location to the rear axle.

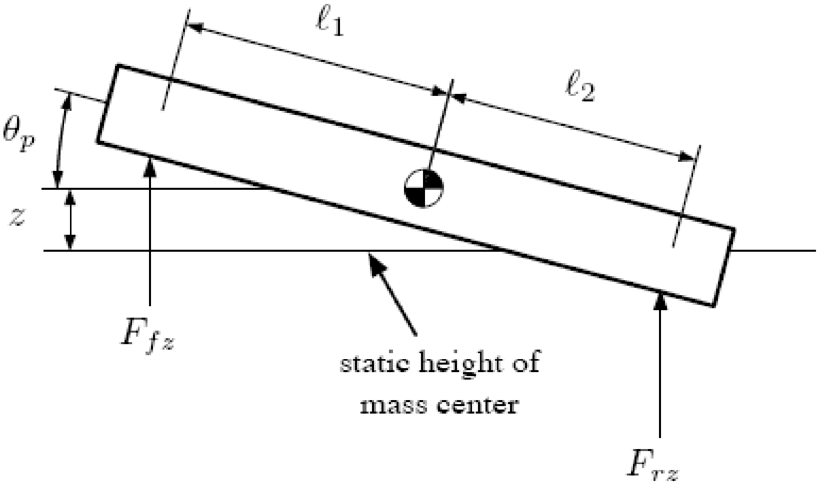

Figure 3.10 Two DOF Vehicle Pitch Model [*Allison* (2008)]

Four linearized equations of motion are used to define the dynamic behavior of this system. These equations have been put into state space form, where the states include $z(t)$, $\theta(t)$, $\dot{z}(t)$, and $\dot{\theta}(t)$:

$$\begin{bmatrix} \dot{z}(t) \\ \dot{\theta}(t) \\ \ddot{z}(t) \\ \ddot{\theta}(t) \end{bmatrix} = \begin{bmatrix} 0 & 0 & 1 & 0 \\ 0 & 0 & 0 & 1 \\ -\dfrac{k_f + k_r}{m_s} & \dfrac{\ell_2 k_r - \ell_1 k_f}{m_s} & -\dfrac{c_f + c_r}{m_s} & \dfrac{\ell_2 c_r - \ell_1 c_f}{m_s} \\ \dfrac{\ell_2 k_r - \ell_1 k_f}{I_y} & -\dfrac{\ell_2^2 k_r + \ell_1^2 k_f}{I_y} & \dfrac{\ell_2 c_r - \ell_1 c_f}{I_y} & -\dfrac{\ell_2^2 c_r + \ell_1^2 c_f}{I_y} \end{bmatrix} \begin{bmatrix} z(t) \\ \theta(t) \\ \dot{z}(t) \\ \dot{\theta}(t) \end{bmatrix} + \begin{bmatrix} 0 \\ 0 \\ 0 \\ \dfrac{M_p(t)}{I_y} \end{bmatrix} \tag{3.74}$$

In the above, $k_f = 2k_s$ and $k_r = 2k_s$ are the front and rear suspension stiffness coefficients, while $c_f = 2c_s$ and $c_r = 2c_s$ are the front and rear suspension damping coefficients. The net rear longitudinal force is the input to the vehicle pitch submodel by way of the normalized pitch moment $M_p(t)/I_y$:

$$M_p(t)/I_y = F_{rx}(t)\big(h + z(t)\big)/I_y \tag{3.75}$$

Note that the above equation produces an algebraic loop in the state space model as the full description of the system input ($M_p(t)/I_y$) is a function of the state variable $z(t)$. Finally, the outputs of interest, $F_{fz}(t)$ and $F_{rz}(t)$, are obtained by [*Allison* (2008)]:

$$F_{fz}(t) = -2\Big(k_f\big(z(t) + \theta_p(t)\ell_1\big) + c_f\big(\dot{z}(t) + \dot{\theta}_p(t)\ell_1\big)\Big) \tag{3.76}$$

$$F_{rz}(t) = -2\Big(k_r\big(z(t) - \theta_p(t)\ell_2\big) + c_r\big(\dot{z}(t) - \dot{\theta}_p(t)\ell_2\big)\Big) \tag{3.77}$$

3.1.5.1.6 Tire Drag Submodel

The tire drag forces account for rolling resistance and inertial forces that must be overcome for vehicle propulsion. In an effort to eliminate an additional algebraic loop, it is assumed that the angular velocity and acceleration of the front and rear tire/wheel assemblies are equal. This implies that the inertial forces, termed spin inertias, can be expressed in terms of the linear velocity $v(t)$. Therefore, the front and rear tire drag forces can be computed as

$$F_{ft}(t) = F_{fz}(t)C_r + \frac{I_{yt}}{r_t(v(t))^2}\dot{v}(t) \tag{3.78}$$

$$F_{rt}(t) = F_{rz}(t)C_r + \frac{I_{yt}}{r_t(v(t))^2}\dot{v}(t) \tag{3.79}$$

where the rolling resistance and spin inertia are given by the first and second terms, respectively, in each equation.

3.1.5.1.7 Rear Tire Slip Submodel

The rear tire slip submodel accounts for differences between the rear tire angular velocity $\omega_r(t)$ and the ratio $v(t)/r_t(v(t))$ so that the motor speed requirements $\omega_m(t)$ can be properly determined in the belt drive submodel. In particular, these differences are characterized through the tire slip i, which varies from zero when $v(t) = \omega_r(t)r_t(v(t))$ to 1 when $v(t) = 0$ [*Wong* (2001)]:

$$i = 1 - \frac{v(t)}{\omega_r(t) r_t\big(v(t)\big)} \tag{3.80}$$

Note that the above definition poses challenges for determining the slip under braking conditions. Therefore, a linearized, inverted model based on Equation (3.80) is constructed such that i is zero when $\omega_r(t) = v(t)/r_t(v(t))$ and -1 when $\omega_r(t) = 0$ [*Allison* (2008)]:

$$\omega_r(t) = \frac{v(t)\big(i+1\big)}{r_t\big(v(t)\big)} \tag{3.81}$$

This model is more useful as it directly predicts $\omega_r(t)$ as a function of i. However, i must be known in advance, and this is accomplished through a lookup table based on empirical tire data that uses $F_{rx}(t)$ and $F_{rz}(t)$ as inputs. Figure 3.11 displays the relationship between these forces and slip for the tires used on this vehicle.

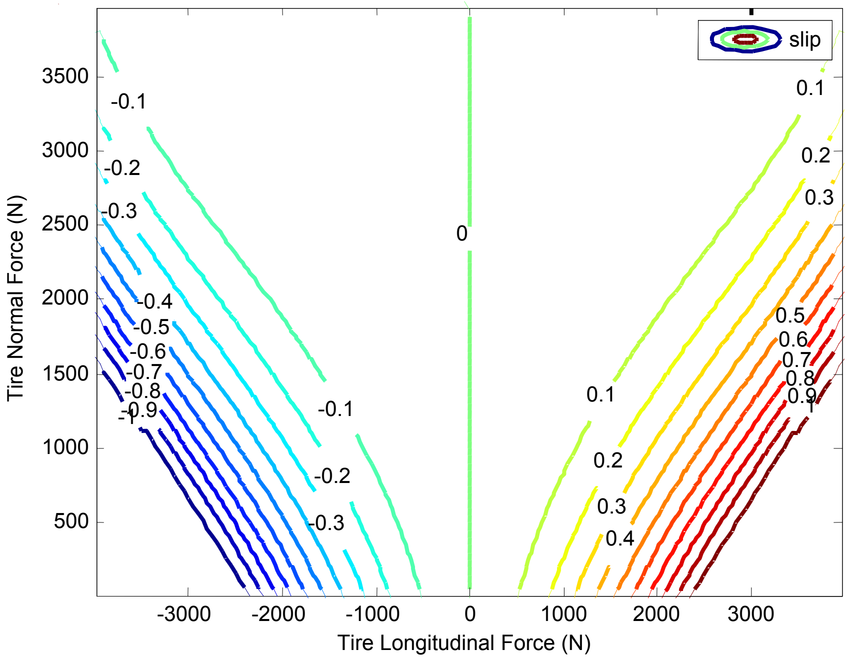

Figure 3.11 Tire Slip Data for Commercial EV [*Allison* (2008)]

3.1.5.1.8 Belt Drive Submodels

The net motor torque and speed requirements are determined through the belt drive submodels. It is assumed here that grooved H pulleys are used within the synchronous belt drive system and that the belt compliance is negligible [*Allison* (2008)]. Additionally, power transmission is idealized to be 100%, yielding the following belt drive relationships:

$$p_r = \frac{r_{po}}{r_{pi}} = \frac{\tau_r(t)}{\tau_{m,net}(t)} = \frac{\omega_m(t)}{\omega_r(t)} \tag{3.82}$$

In the above, r_{po} is the driven pulley radius, r_{pi} is the drive pulley radius, and $\tau_{m,net}(t)$ is the net motor torque requirement (i.e., for two motors). Therefore, rearranging the expressions in Equation (3.82) yields the following net torque and speed requirements:

$$\tau_{m,net}(t) = \tau_r(t) / p_r \tag{3.83}$$

$$\omega_m(t) = \omega_r(t) p_r \tag{3.84}$$

3.1.5.1.9 Motor Inertia Submodel

After passing $\tau_{m,net}(t)$ through a gain of 1/2, the torque requirement for a single motor $\tau_m(t)$ is finally determined in the motor inertia submodel. It should be observed that $\tau_m(t)$ is needed instead of $\tau_{m,net}(t)$ because the data used to determine the power requirement $P(t)$ ($\mathbf{z}_{pLoss}$) is based on a single motor. The motor torque requirement accounts for both the drive torque and the motor inertial torque that must be overcome to achieve vehicle propulsion:

$$\tau_m(t) = \frac{1}{2}\tau_{m,net}(t) + J_r \frac{d\omega_m(t)}{dt} \tag{3.85}$$

This quantity is used in conjunction with $\omega_m(t)$ to interpolate $P(t)$ from $\mathbf{z}_{pLoss}$, and $P(t)$ is doubled to obtain the net motor power requirements.

3.1.5.2 Battery Model: Performance Characteristics

The performance aspects of the lithium-ion battery model are captured through the following equation, which predicts the net battery voltage $v_{net}{}^{bt}$ for a single battery pack [*Doyle et al.* (1993); *Fuller et al.* (1994)]:

$$v_{net}^{bt} = E^{bt} - R_0 I_l^{bt} - R_p I_p^{bt} \tag{3.86}$$

Here, E^{bt} is the battery open circuit voltage, R_0 is the cell internal ohmic resistance, R_p is the polarization resistance, $I_l{}^{bt}$ is the cell load current, and $I_p{}^{bt}$ is the polarization current. The open circuit voltage is estimated as

$$E^{bt} = 193 \cdot SOC^4 - 574 \cdot SOC^3 + 575 \cdot SOC^2 - 170 \cdot SOC + 193 \tag{3.87}$$

where the state of charge (SOC) varies from a maximum of $SOC_{max} = 0.95$ to a minimum of $SOC_{min} = 0.30$ during the simulations. The cell load and polarization currents are determined by solving the following differential equation,

$$\frac{dI_p^{bt}}{dt} = \frac{\left(I_l^{bt} - I_p^{bt}\right)}{\tau_p} \tag{3.88}$$

where τ_p is the polarization time constant [*Allison* (2008)]. This parameter, along with R_0, R_p, and the battery pack capacity $C_{b,pack}$ ($C_{b,pack} = 1/4C_b$) is obtained through a hybrid pulse power characterization (HPPC) test. Based on the HPPC test, it is seen that all of these parameters except $C_{b,pack}$ are dependent on SOC. However, closer inspection reveals that τ_p and R_p are relatively flat with respect to SOC; therefore, only a single, scalar value is needed to represent these parameters during the battery simulations. Because R_0 also varies based on charging conditions (discharge/charge), the HPPC test is performed for each condition to obtain their respective functional data representations $\mathbf{R}_{0,d}$ and $\mathbf{R}_{0,c}$ (ohmic resistance-SOC curves). Note that the HPPC test, which is computationally expensive, is performed for each iteration of the battery design variables (B_I, B_W, B_L); therefore, RBF ANNs have been developed to facilitate the calculation of these parameters during design optimization:

$$\tau_p = f_{\tau_p}(B_I, B_W, B_L) \tag{3.89}$$

$$\mathbf{R}_{0,d} = \mathbf{f}_{R_{0,d}}(B_I, B_W, B_L) \tag{3.90}$$

$$\mathbf{R}_{0,c} = \mathbf{f}_{R_{0,c}}(B_I, B_W, B_L) \tag{3.91}$$

$$R_p = f_{R_p}(B_I, B_W, B_L) \tag{3.92}$$

$$C_b = 4C_{b,pack} = 4f_{C_{b,pack}}(B_I, B_W, B_L) \tag{3.93}$$

3.1.5.3 Vehicle Range, Battery Power Constraint Violations, and Fuel Economy

With the powertrain simulations and battery model performance characteristics defined, the remaining vehicle-level analysis model outputs (R, P_V, mpg_e) can be calculated. This first requires the execution of the battery simulations, which have been developed in Simulink® [*Han* (2008)]. As discussed earlier, these simulations can be performed after the powertrain simulations since there is no feedback between them. The battery power demand simulation takes the power requirements $P(t)$ from the powertrain simulations along with the accessory power load P_{acc} as inputs and satisfies the total system power requirements $P_T(t) = P(t) + P_{acc}$ as necessary. It should be observed that this simulation is performed separately for the power requirements obtained from the backward-looking and forward-looking powertrain models.

When using the power requirements from the backward-looking powertrain model, the power demand cycle is repeated until the battery reaches either its discharge limit or SOC_{min}. The vehicle range R, therefore, is simply the distance d traveled during a single power demand cycle (which is the distance traveled during the drive cycle) multiplied by the number of power demand cycles n_{cyc} completed during the simulation:

$$R = 6.21 \text{x} 10^{-4} n_{cyc} d \tag{3.94}$$

In the above, the coefficient represents a distance conversion factor from meters to miles. Because the number of cycles completed is a discrete value that may slightly underestimate R, this equation is augmented with an interpolation of the distance traveled over the period of time between the last completed cycle and the end of the battery simulation,

$$R = 6.21 \text{x} 10^{-4} n_{cyc} d + F(\mathbf{t}_{cyc}, \mathbf{d}_{cyc}, d) \tag{3.95}$$

where F is an interpolation function. Figure 3.12 illustrates the behavior of this battery simulation when using the power demand cycle from the backward-looking powertrain model. Note that $P_T(t)$ must always lie between the battery discharge and charge limits

$P_u(t)$ and $P_\ell(t)$, respectively, which can be used to define the battery power constraint violation P_V:

$$P_V = \max\{P_T(t) - P_u(t), P_\ell(t) - P_T(t)\} \tag{3.96}$$

However, this constraint is not enforced when using the power demand cycle from the backward-looking powertrain model since it is dominated by a similar constraint for the power demand cycle from the forward-looking powertrain model. In addition, it is assumed that overcharging ($P_T(t) < P_\ell(t)$) is accounted for through a heat-dissipative resistor since this behavior is minimal and only occurs at high SOC [*Allison* (2008)]. Therefore, P_V is only enforced for the discharging limit in the battery simulation when using the power demand cycle from the forward-looking powertrain model, which is only executed once.

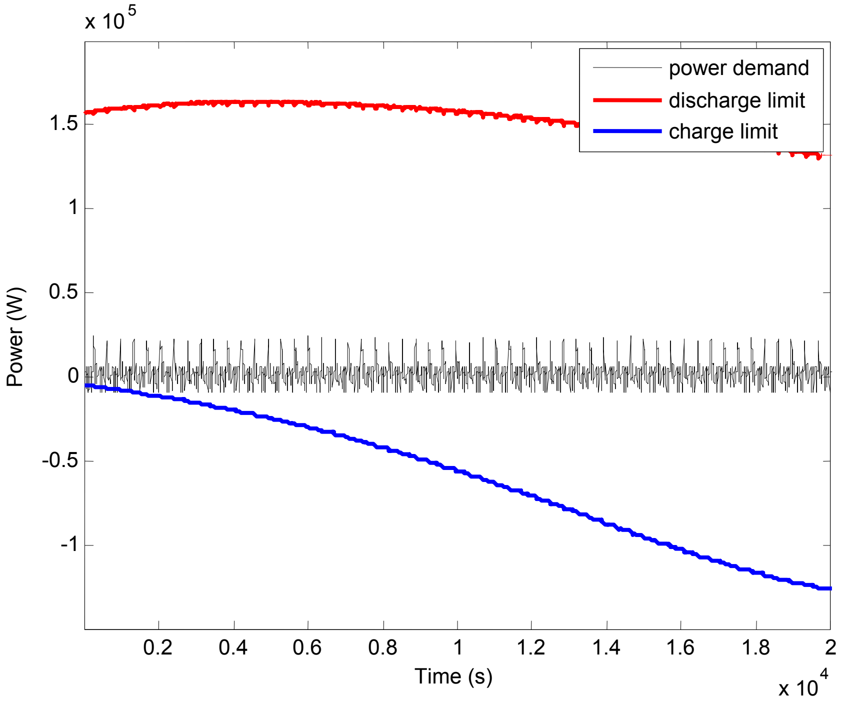

Figure 3.12 Battery Power Demand/Capability during Simulation

Finally, after completing the battery power demand simulations, the battery charging simulation is performed, which enables the fuel economy of the vehicle to be determined. This simulation takes the final SOC from the battery power demand simulation in which R was calculated and is executed until the battery reaches SOC_{max} at the beginning of the battery power demand simulation. The power demand required from the electrical grid to recharge the battery $P_c(t)$ is recorded, which enables the energy requirement to be determined as

$$E_c = \int_0^{t_r} P_c(t)dt \tag{3.97}$$

where t_r is the recharge time. Observe that E_c is also equivalent to the energy consumed during the vehicle range calculation. Therefore, the gasoline-equivalent fuel economy mpg_e can be approximated as

$$mpg_e = 1.317 \text{ x } 10^8 \frac{R}{E_c} \tag{3.98}$$

where the coefficient is an energy conversion factor from Joules to equivalent energy in gallons of gasoline.

3.2 Military Electric Vehicle Powertrain Model

The military electric vehicle was also developed in a MATLAB®/Simulink® environment and is a light-tactical vehicle (LTV) based on the High Mobility Multipurpose Wheeled Vehicle (HMMWV) platform. In this dissertation, however, the military electric vehicle will be referred to as a LTV instead of a HMMWV since it is well-known that the U.S. Army will be replacing the HMMWV with a new generation LTV within the next five years [*Hodge* (2010)]. This new generation LTV is expected to be more fuel-efficient, mobile, and survivable than the current design. Specifically, this vehicle should achieve significant range, maneuver well under significant payload and armor, and minimize visual/acoustic signatures in the battlefield as well as warfighter injuries from underbody blast. However, because detailed specifications for such a vehicle are not available, comparable specifications for the HMMWV M1025A2 have been used to facilitate the design studies in this work [*AM General LLC* (2009)]. A general plan view of the vehicle configuration can be seen in Figure 3.13. The model is for a four-passenger LTV that is designed to eventually support convoy escort and urban assault missions; however, it is recognized that with the current state of EV technology that this vehicle might be best suited for non-tactical missions, such as base operation. With a wheelbase of L = 3.30 m and an overall width of W_o = 2.18 m, this electric LTV still possesses the same overall dimensions as the HMMWV. Similar to the commercial vehicle, the electric LTV is powered by a lithium-ion battery ESS which can vary in length, width, and longitudinal location relative to the front end of the battery compartment such that it lies within the dashed region defined by $b_{\ell,max}$ = 1.5 m and width $b_{w,max}$ = 1.82 m. Four electric traction motors drive each of the wheels through shaft-mounted gearboxes, and design freedom is enabled such that the front motors and gearboxes can be distinct from the rear motors and gearboxes. Finally, each gearbox is connected to a geared hub with a ratio of g_h = 1.92, and 37 x 12.5 R16.5 LT load range “D” radial tires with low-profile runflat capability are used.

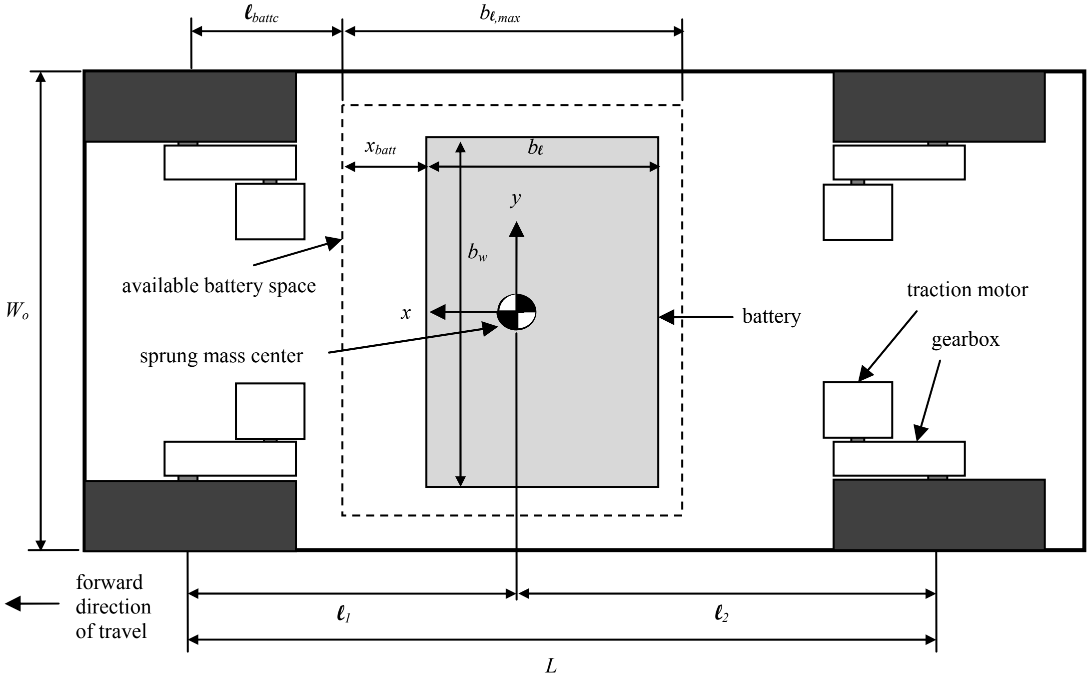

Figure 3.13 General Plan View of Military EV

Because much of the military electric vehicle model is a scaled-up version of the commercial electric vehicle model, most of the underlying analysis models remain the same with respect to their input/output variables. The exceptions to this are the vehicle mass and vehicle-level analysis models, which are redefined as

$$\begin{aligned}[m_s, I_y, I_z, \ell_1, h, b_{w,V}, b_{\ell,V}] = \mathbf{f}_{ltvMass}(x_{batt}, b_\ell, b_w, m_{batt}, m_{mf}, m_{mr}, I_{ym,f}, I_{ym,r}, \cdots \\ I_{zm,f}, I_{zm,r}, y_{m,f}, y_{m,r}, g_{b,f}, g_{b,r})\end{aligned} \tag{3.99}$$

$$\begin{aligned}[mpg_e, t_{50}, \tau_{V,f}, \tau_{V,r}, \omega_{V,f}, \omega_{V,r}, R, P_V, P_{V50}, C_b, d_s, P_{fail}] = \mathbf{f}_{ltv}(B_I, B_W, B_L, \cdots \\ m_{batt}, m_s, I_y, \ell_1, h, g_{b,f}, g_{b,r}, \mathbf{z}_{max,f}, \mathbf{z}_{min,f}, \mathbf{z}_{pLoss,f}, \cdots \\ \mathbf{z}_{max,r}, \mathbf{z}_{min,r}, \mathbf{z}_{pLoss,r}, \omega_{max,f}, \omega_{max,r}, J_{r,f}, J_{r,r})\end{aligned} \tag{3.100}$$

where $\mathbf{f}_{ltvMass}$ and $\mathbf{f}_{ltv}$ correspond to the electric LTV mass and LTV-level analysis models, respectively. With the exception of the front and rear gearbox ratios $g_{b,f}$ and $g_{b,r}$, all of the input/output variables for $\mathbf{f}_{ltvMass}$ are either identical to those for $\mathbf{f}_{evMass}$ or have the same meaning as those for $\mathbf{f}_{evMass}$ but applied to the front/rear drive systems as appropriate. The same is true when comparing the majority of the input/output variables for $\mathbf{f}_{ltv}$ with those for $\mathbf{f}_v$. The exceptions to this are $g_{b,f}$ and $g_{b,r}$, the 0-50 mph time t_{50}, the battery power constraint violations for the backward-looking and forward-looking powertrain models P_V and P_{V50}, the vehicle directional stability d_s, and the probability of failing to meet an underbody blast injury threshold P_{fail}. Note that d_s and P_{fail} are included in the electric LTV model to address design concerns regarding mobility under increased mass and survivability from improvised explosive devices (IEDs). Figure 3.14 illustrates the relationships among the analysis models as well as the problem decomposition for ATC design optimization.

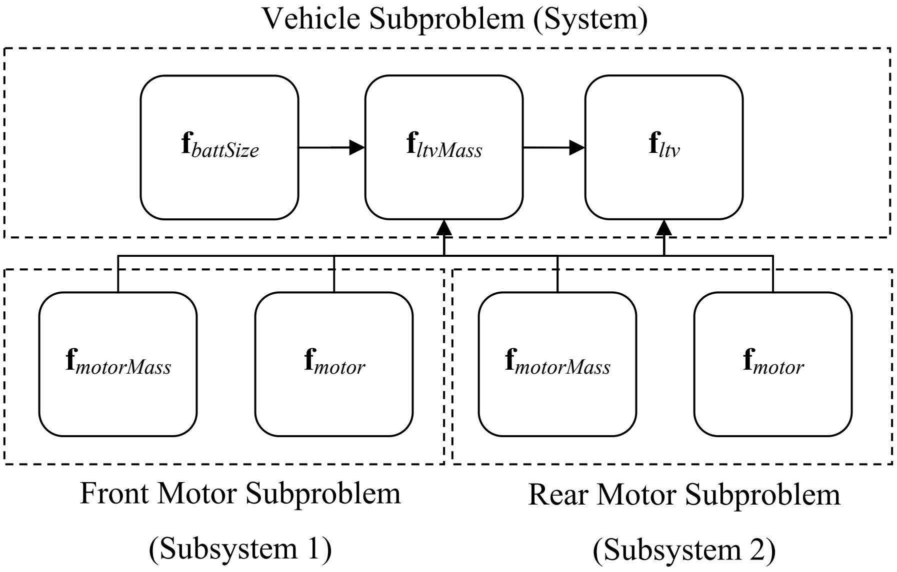

Figure 3.14 Military EV Analysis Model Relationships/Problem Decomposition

The remainder of this section highlights the modifications of the parameters within all of the analysis models and describes the more detailed changes within $\mathbf{f}_{ltvMass}$ and $\mathbf{f}_{ltv}$.

3.2.1 Electric Traction Motor Analysis Model

All of the parameters and equations for determining the intermediate and output variables within the electric traction motor analysis model remain the same for the military vehicle application with the exception of the stator radius proportionality factor t_s. Because the motor design is expected to have a larger rotor radius r_m, it is also reasonable to expect a larger stator radius. Therefore, the stator radius proportionality factor is increased to t_s = 0.5.

3.2.2 Motor Mass Analysis Model

Similarly, the majority of the parameters and equations for determining the intermediate and output variables within the motor mass analysis model remain the same with the exception of the motor lateral center of mass location y_m. This is redefined based on vehicle configuration changes as

$$y_m = \frac{W_o}{2} - \left(\frac{\ell_M}{2} + g_{bwo} + 0.6223 \right) \tag{3.101}$$

where W_o = 2.18 m is the overall width of the vehicle and g_{bwo} = 0.1651 m is the outer width of the gearbox. Observe that in this calculation, clearances between the motor and gearbox and the gearbox and tire are accounted for as well as the tire width.

3.2.3 Battery Size Analysis Model

The battery size analysis model for the military vehicle application remains exactly the same as in the commercial vehicle application.

3.2.4 Electric LTV Mass Analysis Model

The vehicle configuration in Figure 3.13 along with the model parameters listed in Table 3.4 provide the basis for the electric LTV mass analysis model. In particular, the model parameters are estimated using the HMMWV M1025A2 platform. Like the EV mass analysis model, some of the entries in Table 3.4 are termed “baseline” parameters, which indicate that they correspond to a HMMWV M1025A2 vehicle that excludes the mass of the (conventional) powertrain and fuel tank. Therefore, the overall electric LTV mass and related properties are computed using these baseline parameters along with the remaining model parameters and input variables that account for the mass of the electric LTV powertrain (battery, motors, and gearboxes) as well as two occupants (warfighters).

The inclusion of occupant mass is necessary as the output P_{fail} from the coupled analysis model $\mathbf{f}_{ltv}$ is most relevant when considering passengers in the vehicle. Finally, observe that all longitudinal positions in the model are measured relative to the front axle, all vertical positions are measured relative to the ground, and all lateral positions are measured relative to the vehicle centerline.

Table 3.4 Estimated Values of Military EV Mass Analysis Model Parameters

Parameter	Description	Value
m_b	Baseline LTV mass	1930 kg
ℓ_b	Baseline LTV longitudinal com location	1.83 m
h_b	Baseline LTV vertical com location	0.840 m
I_{yb}	Baseline LTV pitch inertia	4644 kg-m^2
I_{zb}	Baseline LTV yaw inertia	5346 kg-m^2
$b_{\ell,max}$	Maximum allowable battery length	1.5 m
$b_{w,max}$	Maximum allowable battery width	1.82 m
b_h	Battery height	0.11 m
ℓ_{battc}	Distance to front of battery compartment	0.66 m
h_{batt}	Battery vertical com location	0.485 m
r_{go}	Gearbox output gear radius	0.0508 m
$r_{go,i}$	Gearbox output idler gear radius	0.0254 m
$r_{gi,i}$	Gearbox input idler gear radius	0.0762 m
g_{fw}	Gear face width	0.0381 m
w_{Ti}	Titanium alloy weight density	44300 N/m^3
m_{occ}	Occupant mass	100 kg
o_ℓ	Occupant fore/aft length	0.635 m
o_w	Occupant width	0.457 m
o_h	Occupant sitting height	1.30 m
ℓ_{occ}	Occupant longitudinal com location	1.55 m
y_{occ}	Occupant lateral com location	0.67 m
L	Wheelbase	3.30 m
W_o	Overall vehicle width	2.18 m

In order to determine the sprung mass m_s of the electric LTV, the mass of the gearboxes must first be computed. Figure 3.15 shows a diagram of the gearbox design, which is loosely based on a similar, parallel shaft design by Rexnord [*Rexnord* (2010)].

Using the information in this figure along with the input variables $g_{b,f}$ and $g_{b,r}$, the front and rear gearbox input gear radii $r_{gi,f}$ and $r_{gi,r}$ can be calculated as:

$$r_{gi,f} = r_{gi,i} / g_{b,f} \tag{3.102}$$

$$r_{gi,r} = r_{gi,i} / g_{b,r} \tag{3.103}$$

The inner lengths of the front and rear gearboxes $g_{b\ell i,f}$ and $g_{b\ell i,r}$ are therefore

$$g_{b\ell i,f} = 2r_{go} + r_{go,i} + r_{gi,i} + 2r_{gi,f} + 0.0254 \tag{3.104}$$

$$g_{b\ell i,r} = 2r_{go} + r_{go,i} + r_{gi,i} + 2r_{gi,r} + 0.0254 \tag{3.105}$$

where the final term in each equation accounts for clearances between the inside of the gearbox and the input/output gears within each gearbox. The outer lengths of the front and rear gearboxes $g_{b\ell o,f}$ and $g_{b\ell o,r}$ are simply

$$g_{b\ell o,f} = g_{b\ell i,f} + 0.0127 \tag{3.106}$$

$$g_{b\ell o,r} = g_{b\ell i,r} + 0.0127 \tag{3.107}$$

where the final term in each equation accounts for the thickness of the gearbox frame in the longitudinal direction. Since the gear face width is the same for all gears, the inner width of the gearboxes g_{bwi} is

$$g_{bwi} = 2g_{fw} + 0.0381 \tag{3.108}$$

where the coefficient for g_{fw} accounts for the idler gear assembly and the last term accounts for clearances between the inside of the gearbox and the gears. The outer width of the gearbox g_{bwo} is

$$g_{bwo} = g_{bwi} + 0.0508 \tag{3.109}$$

where the final term accounts for the thickness of the gearbox frame in the lateral direction. Note that the thickness of the gearbox in this direction is made significantly larger in order to address the requirements for shaft-mounting. Also, observe that the value of g_{bwo} in Equation (3.109) is consistent with what is used in the motor mass analysis model. Because the inner heights of the front and rear gearboxes $g_{bhi,f}$ and $g_{bhi,r}$ depend on how large $r_{gi,i}$ is relative to the input gear radii, the following expressions are used:

$$g_{bhi,f} = 2\max\{r_{gi,i}, r_{gi,f}\} + 0.0254 \tag{3.110}$$

$$g_{bhi,r} = 2\max\{r_{gi,i}, r_{gi,r}\} + 0.0254 \tag{3.111}$$

Again, the final term in each equation accounts for clearances between the inside of the gearboxes and either $r_{gi,i}$ or the input gear radius. The outer heights of the front and rear gearboxes $g_{bho,f}$ and $g_{bho,r}$ are

$$g_{bho,f} = g_{bhi,f} + 0.0127 \tag{3.112}$$

$$g_{bho,r} = g_{bhi,r} + 0.0127 \tag{3.113}$$

where the final term in each equation denotes the thickness of the gearbox frame in the vertical direction. Finally, the mass of front and rear gearboxes $m_{gb,f}$ and $m_{gb,r}$ (assuming negligible shaft mass) are computed as

$$m_{gb,f} = \frac{w_{Ti}}{a_g}\left(\pi g_{fw}\left(r_{go}^2 + r_{go,i}^2 + r_{gi,i}^2 + r_{gi,f}^2\right) + \left(g_{b\ell o,f}\, g_{bwo}\, g_{bho,f}\right) - \left(g_{b\ell i,f}\, g_{bwi}\, g_{bhi,f}\right)\right) \quad (3.114)$$

$$m_{gb,r} = \frac{w_{Ti}}{a_g}\left(\pi g_{fw}\left(r_{go}^2 + r_{go,i}^2 + r_{gi,i}^2 + r_{gi,r}^2\right) + \left(g_{b\ell o,r}\, g_{bwo}\, g_{bho,r}\right) - \left(g_{b\ell i,r}\, g_{bwi}\, g_{bhi,r}\right)\right) \quad (3.115)$$

where $a_g = 9.81$ is the gravitational acceleration in m/s^2.

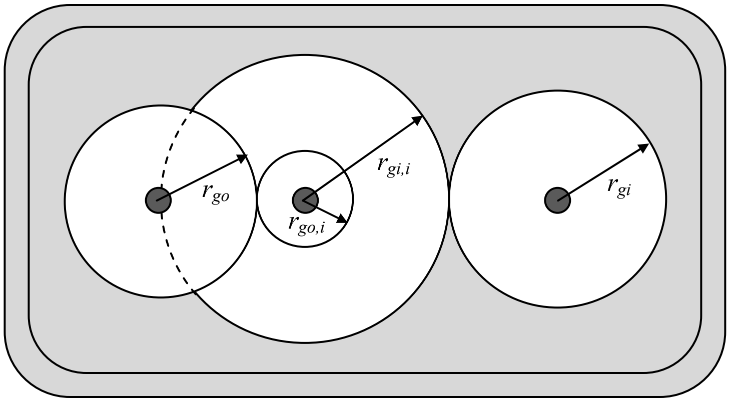

Figure 3.15 Diagram of Parallel Shaft Gearbox

Using these results, the sprung mass m_s of the electric LTV can be expressed as the sum of the baseline, battery, motor, gearbox, and occupant masses:

$$m_s = m_b + m_{batt} + 2(m_{m,f} + m_{m,r} + m_{gb,f} + m_{gb,r} + m_{occ}) \quad (3.116)$$

The longitudinal center of mass location ℓ_1 associated with m_s is

$$\ell_1 = \frac{1}{m_s}\left(m_b \ell_b + m_{batt}\ell_{batt} + 2\left(m_{m,f}\ell_{m,f} + m_{m,r}\ell_{m,r} + m_{gb,f}\ell_{gb,f} + m_{gb,r}\ell_{gb,r} + m_{occ}\ell_{occ}\right)\right) \quad (3.117)$$

where the respective longitudinal center of mass locations for the battery, front/rear motors, and front/rear gearboxes are determined from the following:

$$\ell_{batt} = \ell_{battc} + x_{batt} + b_{\ell} / 2 \tag{3.118}$$

$$\ell_{m,f} = r_{go} + r_{go,i} + r_{gi,i} + r_{gi,f} \tag{3.119}$$

$$\ell_{m,r} = L - (r_{go} + r_{go,i} + r_{gi,i} + r_{gi,r}) \tag{3.120}$$

$$\ell_{gb,f} = \frac{g_{b\ell o,f}}{2} - \left(r_{go} + 0.0127\right) \tag{3.121}$$

$$\ell_{gb,r} = L - \left(\frac{g_{b\ell o,r}}{2} - \left(r_{go} + 0.0127\right)\right) \tag{3.122}$$

Similarly, the vertical center of mass location h associated with m_s is

$$h = \frac{1}{m_s}\left(m_b h_b + m_{batt} h_{batt} + 2\left(m_{m,f} h_{m,f} + m_{m,r} h_{m,r} + m_{gb,f} h_{gb,f} + m_{gb,r} h_{gb,r} + m_{occ} h_{occ}\right)\right) \tag{3.123}$$

where the respective vertical center of mass locations for the front/rear motors, front/rear gearboxes, and occupants are determined from the following:

$$h_{m,f} = h_{gb,f} = \frac{1}{2}\max\left\{g_{bho,f}, \sqrt{\frac{2I_{ym,f}}{m_{m,f}}}\right\} + 0.43 \tag{3.124}$$

$$h_{m,r} = h_{gb,r} = \frac{1}{2}\max\left\{g_{bho,r}, \sqrt{\frac{2I_{ym,r}}{m_{m,r}}}\right\} + 0.43 \tag{3.125}$$

$$h_{occ} = o_h / 2 + 0.43 \tag{3.126}$$

In Equations (3.124)-(3.125), observe that the vertical center of mass locations are dependent on the relative sizes of the motors and gearboxes. Also, note that the final term in each of the above equations accounts for ground clearance.

The electric LTV pitch and yaw moments of inertia are calculated in the same manner as those in the EV mass analysis model. In particular, the corresponding moments of inertia are computed for the baseline LTV, battery, motors, gearboxes, and occupants about the electric LTV center of mass and then combined together to obtain aggregate pitch and yaw moments of inertia. Therefore, $I_{yb,com}$, $I_{zb,com}$, $I_{ybatt,com}$, and $I_{zbatt,com}$ are determined exactly as given in Equations (3.53)-(3.54) and Equations (3.57)-(3.60), while $I_{ym,f,com}$, $I_{ym,r,com}$, $I_{zm,f,com}$, and $I_{zm,r,com}$ are determined by applying Equations (3.61)-(3.62) to the front and rear motors as appropriate. The only new moments of inertia are for the gearboxes and occupants, which require intermediate calculations of their moments of inertia about their own respective centers of mass. Because the gearboxes are rectangular, the pitch and yaw moments of inertia for the front and rear gearboxes are given by:

$$I_{ygb,f} = \frac{1}{12} m_{gb,f} \left(g_{b\ell o,f}^2 + g_{bho,f}^2 \right) \tag{3.127}$$

$$I_{ygb,r} = \frac{1}{12} m_{gb,r} \left(g_{b\ell o,r}^2 + g_{bho,r}^2 \right) \tag{3.128}$$

$$I_{zgb,f} = \frac{1}{12} m_{gb,f} \left(g_{b\ell o,f}^2 + g_{bwo}^2 \right) \tag{3.129}$$

$$I_{zgb,r} = \frac{1}{12} m_{gb,r} \left(g_{b\ell o,r}^2 + g_{bwo}^2 \right) \tag{3.130}$$

This leads to the following moments of inertia for the front and rear gearboxes about the electric LTV center of mass:

$$I_{ygb,f,com} = I_{ygb,f} + m_{gb,f}\left(\left(\ell_{gb,f} - \ell_1\right)^2 + \left(h_{gb,f} - h\right)^2\right) \tag{3.131}$$

$$I_{ygb,r,com} = I_{ygb,r} + m_{gb,r}\left(\left(\ell_{gb,r} - \ell_1\right)^2 + \left(h_{gb,r} - h\right)^2\right) \tag{3.132}$$

$$I_{zgb,f,com} = I_{zgb,f} + m_{gb,f}\left(\left(\ell_{gb,f} - \ell_1\right)^2 + y_{gb}^2\right) \tag{3.133}$$

$$I_{zgb,r,com} = I_{zgb,r} + m_{gb,r}\left(\left(\ell_{gb,r} - \ell_1\right)^2 + y_{gb}^2\right) \tag{3.134}$$

The yaw moments of inertia for the gearboxes about the electric LTV center of mass require knowledge of their lateral center of mass location y_{gb}, which is computed as

$$y_{gb} = \frac{W_o}{2} - \left(\frac{g_{bwo}}{2} + 0.6223\right) \tag{3.135}$$

where the last term accounts for the tire width and the clearance between the tire and gearbox due to the half-shaft. Similarly, it is assumed that the occupants can be approximated through rectangular geometry when seated in the vehicle. Therefore, the pitch and yaw moments of inertia for the occupants are:

$$I_{yocc} = \frac{1}{12} m_{occ}\left(o_\ell^2 + o_h^2\right) \tag{3.136}$$

$$I_{zocc} = \frac{1}{12} m_{occ}\left(o_\ell^2 + o_w^2\right) \tag{3.137}$$

Applying the parallel-axis theorem, the pitch and yaw moments of inertia for the occupants about the electric LTV center of mass are:

$$I_{yocc,com} = I_{yocc} + m_{occ}\left((\ell_{occ} - \ell_1)^2 + (h_{occ} - h)^2\right) \tag{3.138}$$

$$I_{zocc,com} = I_{zocc} + m_{occ}\left((\ell_{occ} - \ell_1)^2 + y_{occ}^2\right) \tag{3.139}$$

Finally, the electric LTV pitch and yaw moments of inertia can be computed as:

$$I_y = I_{yb,com} + I_{ybatt,com} + 2(I_{ym,f,com} + I_{ym,r,com} + I_{ygb,f,com} + I_{ygb,r,com} + I_{yocc,com}) \tag{3.140}$$

$$I_z = I_{zb,com} + I_{zbatt,com} + 2(I_{zm,f,com} + I_{zm,r,com} + I_{zgb,f,com} + I_{zgb,r,com} + I_{zocc,com}) \tag{3.141}$$

The last two outputs of the electric LTV mass analysis model are the battery packaging constraint violations $b_{w,V}$ and $b_{\ell,V}$, which are already given by Equations (3.65)-(3.66).

3.2.5 LTV-Level Analysis Model

The LTV-level analysis model is very similar to the vehicle-level analysis model for the commercial vehicle application in that it uses two powertrain simulations followed by two battery simulations to estimate vehicle range, acceleration performance, and energy efficiency for the LTV. However, in addition to facilitating the calculation of constraints related to motor torque and speed capability along with battery power capability and cost, the model also enables the computation of constraints related to directional stability and the probability of failing to meet an underbody blast injury threshold. Although many of the powertrain simulation modifications from the commercial vehicle application are merely size related, several configuration changes have been made for the military vehicle. These adjustments are discussed in detail in the following subsections, along with the calculations for new analysis model outputs d_s and P_{fail}. Since the battery simulations remain exactly the same, they are excluded from the discussion in these subsections.

3.2.5.1 Powertrain Models

The powertrain simulations have been developed in Simulink® again and consist of several submodels that are linked together in both backward-looking and forward-looking models, respectively. Recall that the backward-looking model uses a prescribed drive cycle along with analysis model input variables and parameters to predict motor torque, speed, and power requirements at each simulation time step. Front and rear motor constraint violations can then be evaluated by using these requirements and applying Equations (3.67)-(3.68) as appropriate. The combined motor power requirements, however, are passed as inputs to the battery power demand simulation to facilitate the vehicle range estimation. The forward-looking model uses the same submodels, input variables, and parameters but instead predicts the 0-50 mph acceleration time t_{50} by linearly increasing the velocity of the vehicle from zero at $t = 0$ to 50 mph (22.2 m/s).

Figure 3.16 shows a block diagram of the backward-looking powertrain model, which includes the input drive cycle. The drive cycle selected for the military EV powertrain design studies is a standard, convoy escort cycle that the HMMWV is tested on currently. Because of the sensitive nature of this information, the drive cycle is not shown in this dissertation; however, it is noted that it covers a range of 42 miles (67.2 km) in approximately 1.14 hours (4100 seconds) with an average speed of 37 mph (16.4 m/s).

Since the same submodels are used in the forward-looking powertrain model, the block diagram of this simulation is excluded. However, both simulations use the same model parameters as listed in Table 3.5. The remainder of this section describes each submodel for both simulations along with any associated assumptions.

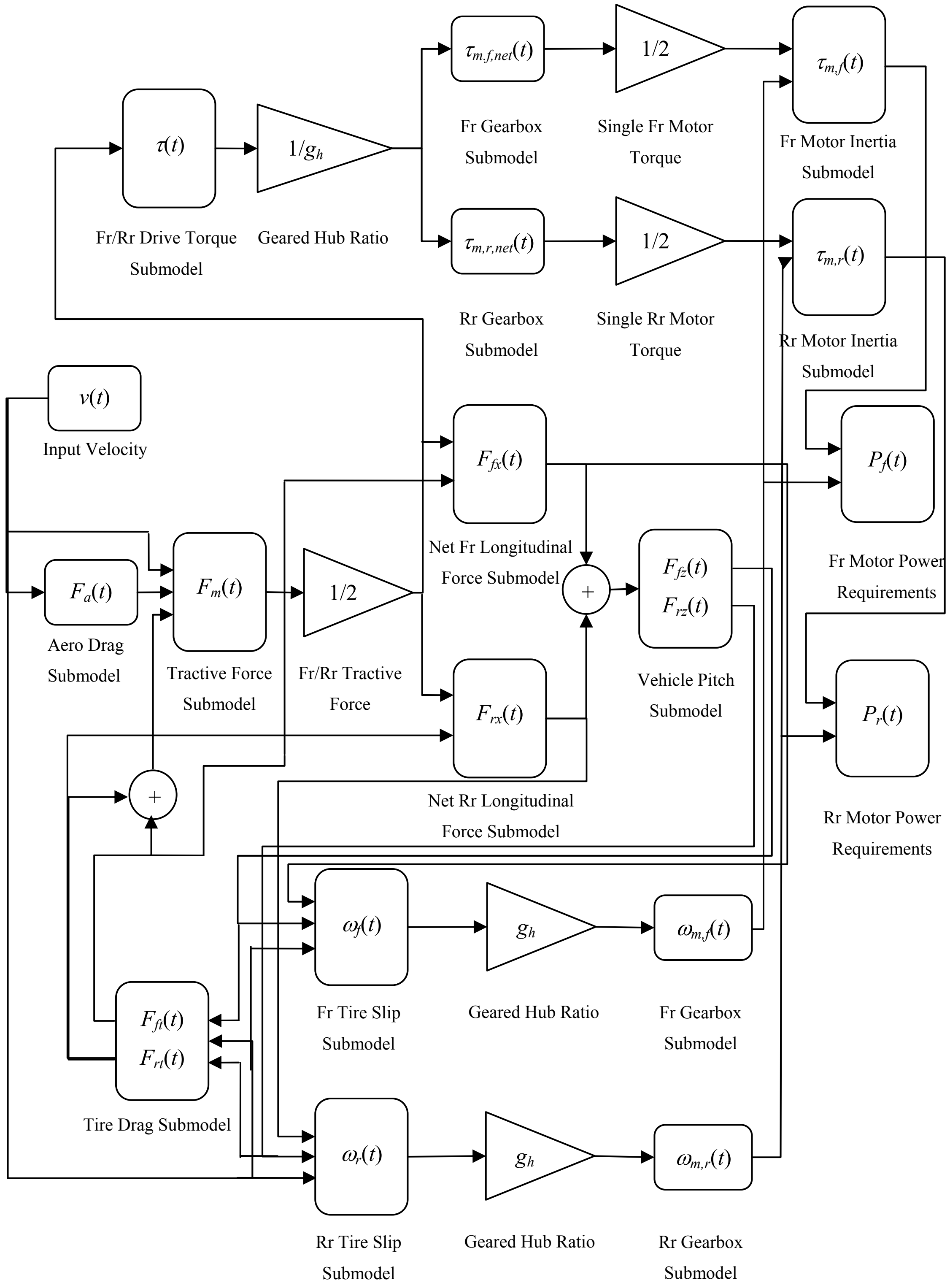

Figure 3.16 Block Diagram of Powertrain Simulation Submodels for Military EV

Table 3.5 Estimated Values of Powertrain Model Parameters for Military EV

Parameter	Description	Value
m_{us}	Unsprung mass	440 kg
ζ	Damping ratio per wheel	83500 N-s/m
k_s	Suspension stiffness per wheel	16000 N/m
L	Wheelbase	3.30 m
C_d	Drag coefficient	0.70
A_f	Frontal area	3.58 m^2
ρ_a	Air density	1.10 kg/m^3
g_h	Geared hub ratio	1.92
r_{go}	Gearbox output gear radius	0.0508 m
$r_{go,i}$	Gearbox output idler gear radius	0.0254 m
$r_{gi,i}$	Gearbox input idler gear radius	0.0762 m
I_{yt}	Tire/wheel assembly spin inertia per axle	14.22 $kg\text{-}m^2$
C_r	Tire rolling resistance	0.01
r_t	Tire radius	0.470 m
P_{acc}	Accessory power load	11200 W

3.2.5.1.1 Aerodynamic Drag Submodel

The aerodynamic drag force on the electric LTV is given by the same equation (Equation (3.69)) that was used for the commercial EV.

3.2.5.1.2 Tractive Force Submodel

The tractive force of the electric LTV, which is now denoted as $F_m(t)$, is also given by the same equation (Equation (3.70)) that was used for the commercial EV. Note that the difference in the use of notation is to reflect the fact that the tractive force must be provided by all motors, not just the rear motors.

3.2.5.1.3 Front/Rear Drive Torque Submodel

Assuming the tractive force is split evenly among the front and rear motors, the drive torque for the front or rear motors can be calculated by modifying Equation (3.71) as:

$$\tau(t) = \tau_f(t) = \tau_r(t) = \frac{1}{2}F_m(t)r_t \tag{3.142}$$

Observe that for the electric LTV model, r_t is assumed to be constant as there is no readily available data for the development of a dynamically-loaded tire radius model. This simplification is expected to have a minor impact on the quality of the powertrain models.

3.2.5.1.4 Net Longitudinal Force Submodels

Similarly, the net longitudinal forces on both the front and rear tires is found by slightly modifying Equation (3.73) and applying it as appropriate:

$$F_{fx}(t) = \frac{1}{2} F_m(t) - F_{ft}(t) \tag{3.143}$$

$$F_{rx}(t) = \frac{1}{2} F_m(t) - F_{rt}(t) \tag{3.144}$$

These quantities are used as inputs to the front and rear tire slip models, respectively.

3.2.5.1.5 Vehicle Pitch Submodel

With the exception of the normalized pitch moment $M_p(t)/I_y$, the vehicle pitch submodel remains exactly the same as in the commercial EV model. This quantity is modified as:

$$M_p(t)/I_y = \left(F_{fx}(t) + F_{rx}(t)\right)\left(h + z(t)\right)/I_y \tag{3.145}$$

Also, because the suspension damping coefficient c_s could not determined directly, it was assumed that the suspension was lightly-damped and that its damping coefficient could be obtained using basic dynamic systems analysis:

$$c_s = 2\varsigma\sqrt{k_s m_s} \tag{3.146}$$

3.2.5.1.6 *Tire Drag Submodel*

The tire drag forces are calculated in the same manner as in Equations (3.78)-(3.79) with the exception that r_t is constant.

3.2.5.1.7 *Tire Slip Submodels*

The front and rear tire slip submodels apply Equation (3.81) as appropriate to predict the front and rear tire angular velocities as a function of the tire slip. Since the tires used for the electric LTV are different than those used for the commercial EV, a new slip lookup table has been developed for these submodels. Figure 3.17 displays the data for this lookup table, which is based on an analytical model cited in [*Ersal et al.* (2009)]. Because of the properties of this model, only slip data between -0.25 and 0.25 could be recorded, which is sufficient for the design studies in this dissertation.

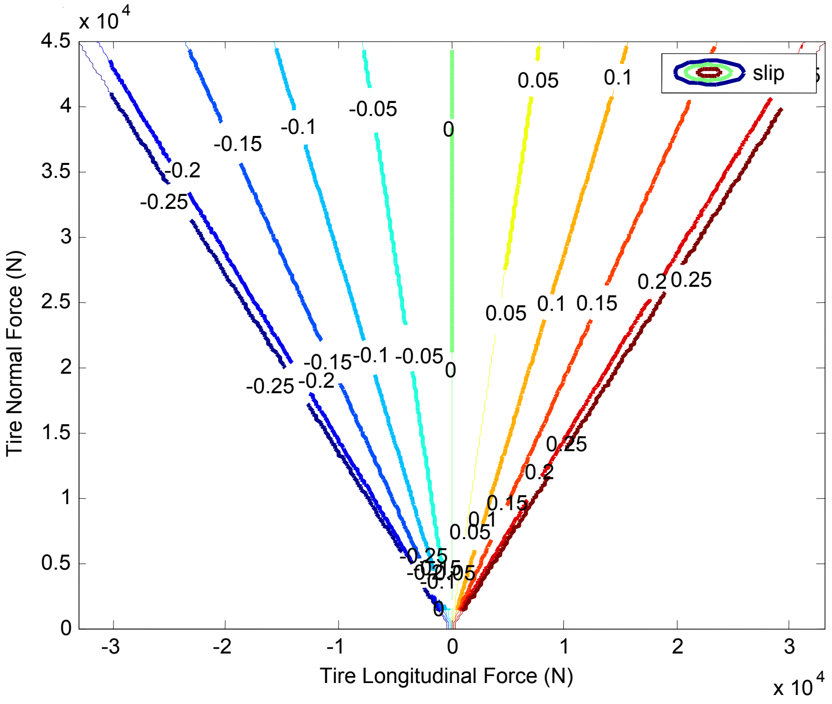

Figure 3.17 Tire Slip Data for Military EV

3.2.5.1.8 Gearbox Submodels

After passing $\tau(t)$, $\omega_f(t)$, and $\omega_r(t)$ through the geared hubs, the net torque and speed requirements for the front and rear motors are determined through the gearbox submodels. These submodels, which have been discussed in the electric LTV mass analysis model, are similar to the belt drive submodels for the commercial EV in that power transmission is idealized to be 100%. Therefore, net torque and speed requirements for the front and rear motors are given by:

$$\tau_{m,f,net}(t) = \frac{\tau(t)}{g_h}\left(\frac{r_{go,i}}{r_{go}g_{b,f}}\right) \tag{3.147}$$

$$\tau_{m,r,net}(t) = \frac{\tau(t)}{g_h}\left(\frac{r_{go,i}}{r_{go}g_{b,r}}\right) \tag{3.148}$$

$$\omega_{m,f}(t) = \omega_f(t)g_h\left(\frac{r_{go}g_{b,f}}{r_{go,i}}\right) \tag{3.149}$$

$$\omega_{m,r}(t) = \omega_r(t)g_h\left(\frac{r_{go}g_{b,r}}{r_{go,i}}\right) \tag{3.150}$$

3.2.5.1.9 Motor Inertia Submodels

Finally, Equation (3.85) is reapplied to the front and rear motors as appropriate to determine the torque requirements for a single front and rear motor. Like the powertrain simulations for the commercial EV, these torque requirements along with $\omega_{m,f}(t)$ and $\omega_{m,r}(t)$ are used to interpolate the motor power requirements $P_f(t)$ and $P_r(t)$ from $\mathbf{z}_{pLoss,f}$ and $\mathbf{z}_{pLoss,r}$.

3.2.5.2 Vehicle Range, Battery Power Constraint Violations, and Fuel Economy

The vehicle range, battery power constraint violations, and fuel economy for the electric LTV are computed in nearly the same manner as described by Equations (3.95)-(3.98) for the commercial EV. Specifically, the battery power demand simulation takes the total system power requirements $P_T(t) = P_f(t) + P_r(t) + P_{acc}$ from the backward-looking powertrain model and determines the vehicle range R through the number of times this power demand cycle can be repeated until reaching either the battery discharge limit $P_u(t)$ or SOC_{min}. However, unlike the commercial EV, a battery power constraint violation P_V for the backward-looking powertrain model is calculated as the battery often risks significant overcharging during the repeated power demand cycles. To account for the high SOC at the beginning of this simulation, the violation of the battery charge limit $P_\ell(t)$ is relaxed with the assumption that the excess energy is absorbed by a heat-dissipative resistor. The battery power constraint violation for the backward-looking powertrain model is therefore

$$P_V = \max\{P_T(t) - P_u(t), (P_\ell(t) - 10000) - P_T(t)\} \tag{3.151}$$

The same battery simulation is performed again using $P_T(t)$ from the forward-looking powertrain model to calculate the associated battery power constraint violation P_{V50} as given by Equation (3.96). Note that this simulation is only executed for a single power demand cycle since no vehicle range calculations are associated with the forward-looking powertrain model. Finally, the battery charging simulation uses the final SOC from the battery power demand simulation for the backward-looking powertrain model to determine the energy consumption E_c over R. The gasoline-equivalent fuel economy mpg_e is then computed according to Equation (3.98).

3.2.5.3 Vehicle Directional Stability and Probability of Injury Threshold Failure

The vehicle directional stability d_s is actually calculated through an analysis submodel within the LTV-level analysis model. Given prescribed loading conditions, tire stiffness properties, and a desired, maximum stable vehicle speed, this analysis submodel predicts whether the vehicle would remain directionally stable (i.e., not risk spinning out) at the desired maximum stable speed. Although d_s could be evaluated as a separate entity in some cases, it is intentionally incorporated within $\mathbf{f}_{ltv}$ because it is a vehicle-level quantity and some of its critical parameters are a function of $F_{fz}(t)$ and $F_{rz}(t)$ from the backward-looking powertrain model. The electric LTV directional stability analysis submodel f_{dsLTV} takes the sprung mass m_s, longitudinal center of mass location ℓ_1, and the average front and rear tire normal forces $F_{fz,avg}$ and $F_{rz,avg}$ and computes d_s based on a model in [*Wong* (2001)]:

$$d_s = f_{dsLTV}(m_s, \ell_1, F_{fz,avg}, F_{rz,avg}) \tag{3.152}$$

The first step is to calculate the weight of the vehicle w_v and its distribution on the front and rear tires $w_{v,f}$ and $w_{v,r}$:

$$w_v = (m_s + m_{us})a_g \tag{3.153}$$

$$w_{v,f} = w_v\left(\frac{L-\ell_1}{2L}\right) \tag{3.154}$$

$$w_{v,r} = w_v\left(\frac{\ell_1}{2L}\right) \tag{3.155}$$

In the above, $a_g = 9.81$ is the gravitational acceleration constant in m/s^2. From here, the front and rear tire cornering stiffnesses $C_{\alpha,f}$ and $C_{\alpha,r}$ are evaluated based on a lateral tire slip model for a similar application cited in [*Ersal et al.* (2009)]:

$$C_{\alpha,f} = \left(\frac{2.5}{\alpha_n}\right)F_{fz,avg} \tag{3.156}$$

$$C_{\alpha,r} = \left(\frac{2.5}{\alpha_n}\right)F_{rz,avg} \tag{3.157}$$

Note that $\alpha_n = 0.5$ is the saturation condition for lateral tire slip and that $C_{\alpha,f}$ and $C_{\alpha,r}$ are expressed in N/rad. This enables the understeer coefficient K_{us} to be computed, which indirectly determines the stability of the vehicle:

$$K_{us} = \frac{w_{v,f}}{C_{\alpha,f}} - \frac{w_{v,r}}{C_{\alpha,r}} \tag{3.158}$$

Finally, the directional stability of the vehicle is given by

$$d_s = L + K_{us} \frac{v_{max}^2}{a_g} \tag{3.159}$$

where $v_{max} = 70$ mph (31.3 m/s) is the desired maximum stable speed of the electric LTV based on the maximum speed of the HMMWV. Observe that directional stability of the electric LTV is guaranteed as long as $d_s \geq 0$. This always occurs when $K_{us} \geq 0$ regardless of the vehicle speed. In particular, when $K_{us} > 0$, the electric LTV is understeer, which means that the steering system response is less than the steering input. This is the condition under which most vehicles are designed. When $K_{us} = 0$, the electric LTV is neutral steer, which means that the steering system response matches the steering input exactly. When $K_{us} < 0$, the electric LTV is oversteer, which means that the steering system response is greater than the steering input. This often occurs in larger vehicles that transport heavy loads such as trucks and tractor-trailers. Under this condition, directional stability is speed-dependent, with the limit being v_{max} when $d_s = 0$.

The final output of the LTV-level analysis model is the probability of failure to meet injury thresholds for underbody blast due to IEDs. This is a critical quantity to design for as one of the leading causes of death for U.S. warfighters is from IEDs while operating LTVs. Even when such explosions are not fatal, they often leave warfighters severely injured or maimed. Therefore, the U.S. Army has set design targets that require current LTVs to protect against a 10% chance of severe injury on the abbreviated injury scale (AIS) for the neck, lumbar/spine, and tibia of occupants. These thresholds are usually met for heavy vehicles such as up-armored HMMWVs, but the weight of these vehicles can also significantly limit their mobility in terms of range and acceleration performance. Conversely, lighter vehicles such as the electric LTV in this dissertation are more mobile but run a greater risk of failing to satisfy the injury thresholds. A metric has therefore been developed to address this tradeoff between the probability of failing to satisfy the injury thresholds and mobility:

$$P_{fail} = 1 - \frac{1}{2}\left(1 + erf\left(\frac{\left(1757 - \dfrac{4\text{x}10^6}{m_T^{1.02}}\right)}{\sqrt{2\left(\dfrac{2\text{x}10^6}{m_T^{1.04}}\right)^2}}\right)\right) \tag{3.160}$$

Note that mobility is reflected in this equation through the total vehicle mass $m_T = m_s + m_{us}$, which is ultimately dependent on m_s.

3.3 Summary

This chapter went into exhaustive detail describing two electric vehicle models for commercial and military applications, respectively. Specifically, the manner in which the input/output variables are calculated for each of the underlying analysis models in both applications was discussed in depth. Such detail is necessary for a thorough understanding of the design studies that will be performed later in this dissertation. Although the initial commercial EV model was developed by Allison, several corrections and modifications were made to improve the quality of the model as well as its relevance to the current design studies. These improvements facilitated the development of the military EV model, which is largely a scaled-up version of the commercial EV model. Both models will provide the basis for the design studies in Chapters 4-7 that make use of POD, AVASIM, and constraint management approaches for the coupled, functional data in decomposition-based design optimization.

Chapter 4

Commercial Electric Vehicle Design Optimization

In Chapter 1, it was mentioned that recent work involving the decomposition-based design optimization of an EV powertrain identified POD as an attractive reduced representation method for coupled, functional data variables. This was because it utilized data samples exclusively to generate a functional form of its approximation model, required limited assumptions regarding the number of reduced representation variables (POD coefficients), and used a relatively small number of such variables for approximations [*Alexander et al.* (2010a)]. However, it was also acknowledged that there was a need to further explore the effect of the cumulative percentage variation (CPV) on the resulting performance of the ATC optimization strategy.

Recall that the CPV is a tuning parameter within POD that controls both the amount of information captured by the approximation as well as the number of POD coefficients necessary for the reduced representation. It is well known that as the CPV is reduced, less information (or accuracy) is required for the approximation and hence fewer POD coefficients are needed for the model. Nevertheless, it is uncertain how these adjustments would affect a decomposition-based optimization strategy like ATC. While it is hypothesized that reducing the CPV would accelerate ATC convergence via fewer decision variables, it is not clear whether this would provide an inaccurate or suboptimal design solution given the fact that ATC would enforce some degree of accuracy on the VVCVs via an updated, weighted penalty function. The current literature, including the closely-related work by LeGresley and Alonso [*LeGresley and Alonso* (2004)], does not explore this problem for any decomposition-based optimization strategy. This chapter, therefore, investigates this issue by constructing POD representations for three CPV values, implementing them in ATC, and observing their impact on the optimal design solutions. Also, to facilitate comparisons among the three sets of POD representations, an all-in-one (AiO) optimization problem formulation and solution for the commercial EV powertrain model is introduced at the beginning of this chapter.

4.1 AiO Problem Formulation and Solution

The AiO problem formulation uses the same analysis models as those described in Equations (3.1)-(3.5) for the commercial EV with the exception that the electric traction motor analysis model $\mathbf{f}_{motor}$ is integrated as a sub-analysis model within the vehicle-level analysis model $\mathbf{f}_v$. This was necessary because in the AiO problem, the motor design is not considered separately; instead, all of the key design components of the EV powertrain—the battery, belt-drive system, and motors—are considered simultaneously. Therefore, Equation (3.5) is modified as

$$[mpg_e, t_{60}, \tau_V, \omega_V, R, P_V, C_b] = \mathbf{f}_v(B_I, B_W, B_L, m_{batt}, m_s, I_y, \boldsymbol{\ell}_1, h, p_r, \ell_s, r_m, n_c, R_r) \quad (4.1)$$

where the input variables to $\mathbf{f}_{motor}$ are now shared with $\mathbf{f}_v$. Figure 4.1 illustrates the relationships among the remaining analysis models that were described in Chapter 3 for the commercial EV powertrain, with the dashed box indicating that all analysis models are integrated into a single optimization problem formulation.

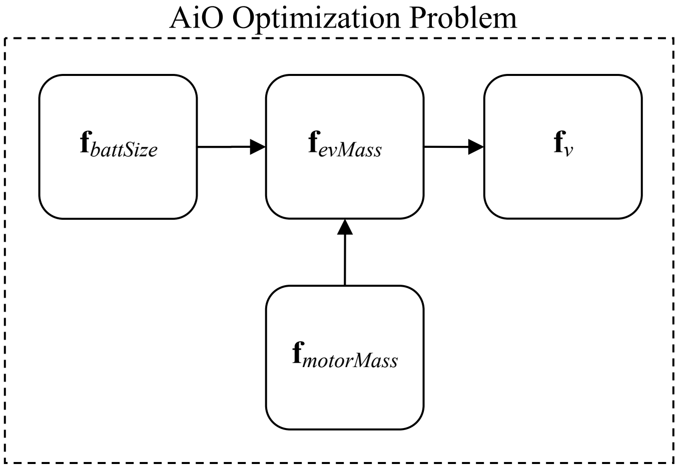

Figure 4.1 Analysis Model Relationships for Commercial EV AiO Problem

The objective of the AiO problem formulation is to maximize the gasoline-equivalent fuel economy of the commercial EV while satisfying constraints related to battery packaging, performance, motor feasibility, vehicle range, power availability, and battery capacity:

$$
\begin{aligned}
&\min_{\mathbf{x}} \; -mpg_e(\mathbf{x}) \\
&\textit{subject to} \\
&\qquad g_1 = b_{w,V}(\mathbf{x}) \le 0 \qquad\qquad g_5 = \omega_V(\mathbf{x}) \le 0 \\
&\qquad g_2 = b_{\ell,V}(\mathbf{x}) \le 0 \qquad\qquad g_6 = R_{min} - R(\mathbf{x}) \le 0 \\
&\qquad g_3 = t_{60}(\mathbf{x}) - t_{60max} \le 0 \quad g_7 = P_V(\mathbf{x}) \le 0 \\
&\qquad g_4 = \tau_V(\mathbf{x}) \le 0 \qquad\qquad g_8 = C_b(\mathbf{x}) - C_{bmax}(\mathbf{x}) \le 0 \\
&\textit{where} \\
&\qquad \mathbf{x} = [B_I, B_W, B_L, x_{batt}, p_r, \ell_s, r_m, n_c, R_r]
\end{aligned}
\tag{4.2}
$$

In the above, g_1 and g_2 are battery packaging constraints, g_3 is a performance (0-60 mph acceleration time) constraint, g_4 and g_5 are motor feasibility constraints, g_6 is a vehicle range constraint, g_7 is a power availability constraint, and g_8 is a battery capacity constraint. Note that appropriate bound constraints are included for the decision variables in **x**. Due to the presence of non-smoothness in the optimization problem, a derivative-free optimization software package known as NOMADm [*Abramson* (2007)] was used to solve the problem. This optimizer is based on mesh-adaptive search algorithms and was developed and implemented in a MATLAB® environment. Finally, in solving the AiO optimization problem, observe that the default settings for NOMADm were appropriate.

The results from the AiO problem formulation are shown in Table 4.1. It should be noted that the only active constraints in this problem were the lower bound on B_I, the performance constraint g_3, and the vehicle range constraint g_6; these were limited to $B_I = 0.70$, $t_{60max} = 10$ s, and $R_{min} = 100$ miles, respectively. Such behavior is expected given the objective of energy efficiency for the commercial EV. Specifically, maximizing the gasoline-equivalent fuel economy of the vehicle compromises its ability to achieve superior performance and range capability. Additionally, the aggressive power requirements for a reasonable 0-60 mph acceleration time are related to the battery design, which requires large electrode surface areas and a thin separator for high-power applications. Finally, observe that the design solution suggests the use of 43 kW motors (Figure 4.2) to propel a 1080 kg vehicle, with approximately 11.9% (128 kg) of the mass associated with the battery. These design conditions indicate that the commercial EV could achieve a gasoline-equivalent fuel economy of nearly $mpg_e = 195$ mpg.

Table 4.1 Optimal Decision Vector for Commercial EV AiO Problem

B_I	B_W	B_L	x_{batt}	p_r	l_s	r_m	n_c	R_r
0.70	1.10	19.75	0.10	2.91	0.096	0.124	20.85	0.052

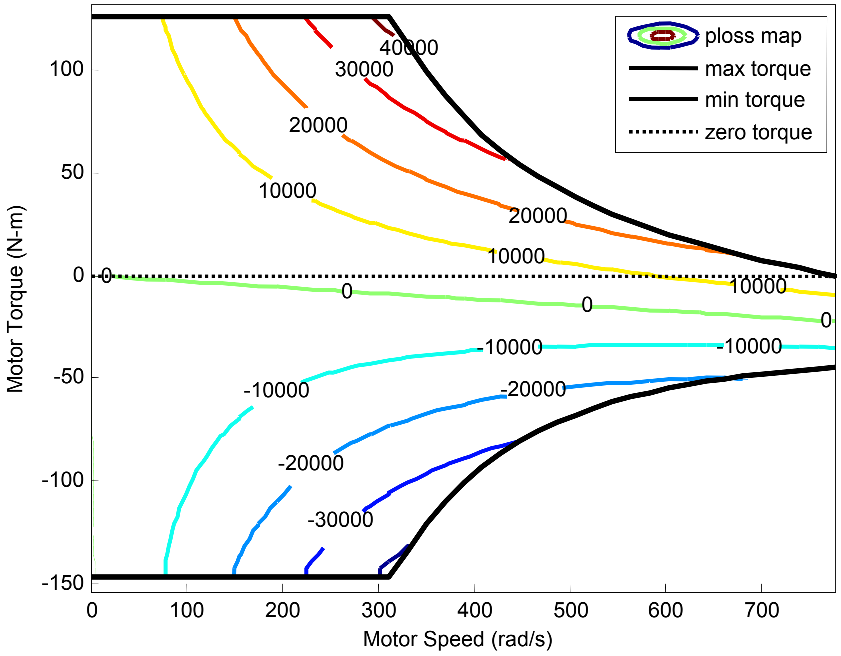

Figure 4.2 Optimal Motor Map, Commercial EV AiO Problem

4.2 POD Representations and Accuracy Assessment

In preparation for the ATC problem formulation, POD representations were developed *a priori* to approximate the VVCVs associated with the maximum and minimum motor torque curves and power loss map:

$$\mathbf{z}_{max} \approx \mathbf{\Phi}_{p,max}\mathbf{z}_{r,max} + \bar{\mathbf{z}}_{max} \tag{4.3}$$

$$\mathbf{z}_{min} \approx \mathbf{\Phi}_{p,min}\mathbf{z}_{r,min} + \bar{\mathbf{z}}_{min} \tag{4.4}$$

$$\mathbf{z}_{pLoss} \approx \mathbf{\Phi}_{p,pLoss}\mathbf{z}_{r,pLoss} + \bar{\mathbf{z}}_{pLoss} \tag{4.5}$$

From the discussion on POD in Chapter 2, it is known that the reduced basis function matrices $\mathbf{\Phi}_{p,max}$, $\mathbf{\Phi}_{p,min}$, and $\mathbf{\Phi}_{p,pLoss}$ were constructed using column-wise functional data samples in $\mathbf{Z}_{max}$, $\mathbf{Z}_{min}$, and $\mathbf{Z}_{pLoss}$, respectively. The functional data samples themselves were generated through a Latin hypercube sample (LHS) design of experiments consisting of $m = 500$ motor map samples from $\mathbf{f}_{motor}$. An intermediate, yet critical, part of the sampling process was the interpolation of all sampled motor maps onto a prescribed, standard torque-speed mesh. This was necessary as the motor maps produced by $\mathbf{f}_{motor}$ use different torque-speed meshes for different values of the input variables to $\mathbf{f}_{motor}$. The use of a standard mesh would facilitate both ATC consistency evaluations and POD accuracy assessment through error metrics such as RMSE and/or AVASIM. Additionally, a standard mesh would eliminate the need to develop POD representations for the independent variables associated with the functional data discretizations since the mesh region would be the same for all motor maps regardless of their corresponding motor design.

Because the primary motivation for establishing a standard mesh was effective ATC consistency evaluations, the torque-speed mesh region was loosely based on the motor maps at the initial decision vector $\mathbf{x}_0^{AiO}$ and the optimal decision vector $\mathbf{x}_*^{AiO}$ from the AiO optimization problem. It is recognized that such a heuristic for setting the standard mesh region would either truncate or extrapolate the functional data for some of the sampled motor maps; however, these samples capture the entire motor design space, and it is more important to accurately capture the motor maps along the expected search direction of the optimizer since this would directly impact solution accuracy. Therefore, it was reasonable to set the standard mesh region using this heuristic given the fact that the ATC problem formulation begins at $\mathbf{x}_0^{AiO}$ and is expected to converge to $\mathbf{x}_*^{AiO}$ as $\mathbf{c}$ converges to $\mathbf{0}$. Finally, the number of torque and speed mesh points $n_{p,\tau}$ and $n_{p,\omega}$ specified for the standard mesh were identical to the number of torque and speed mesh points used for the original motor maps produced by $\mathbf{f}_{motor}$. Hence, the standard mesh used for the sampled motor maps was defined as

$$\tau_i^{mesh} = -315 + \left(\frac{730}{n_{p,\tau} - 1}(i-1) \right), \quad i = 1 \cdots 81 \tag{4.6}$$

$$\omega_i^{mesh} = \frac{800}{n_{p,\omega} - 1}(i-1), \quad i = 1 \cdots 41 \tag{4.7}$$

where $n_{p,\tau} = 81$ and $n_{p,\omega} = 41$.

Based on the definition of the standard mesh, the number of discretized points in $\mathbf{z}_{max}$, $\mathbf{z}_{min}$, and $\mathbf{z}_{pLoss}$ were $q_{max} = 41$, $q_{min} = 41$, and $q_{pLoss} = 3321$, respectively. Since $q_{max} = q_{min} << m$, the direct method outlined in Equations (2.6)-(2.9) was used to develop the POD representations for the maximum and minimum motor torque curves. Conversely, the method of snapshots described in Equations (2.10)-(2.12) was used to develop the POD representation for the motor power loss map since $q_{pLoss} >> m$. Table 4.2 lists the number of POD coefficients (and hence reduced representation variables) required for three distinct values of CPV_{goal}: 99.99%, 99.95%, and 99.85%. These values were selected partially based on the literature, which suggests that $CPV_{goal} \geq 99\%$ [*Bui-Thanh et al.* (2004)], and partially based on the development of a meaningful study that would demonstrate significant differences in the number of POD coefficients for each case while satisfying accuracy requirements per the liberal validity criterion in AVASIM for an independent (non-sample) set of motor maps. In each case, it is evident that the combined dimensionality Q of the VVCVs was dramatically reduced from $Q = q_{max} + q_{min} + q_{pLoss} = 3403$ to $Q = p_{max} + p_{min} + p_{pLoss} = 116$, $Q = 77$, and $Q = 58$, respectively [*Alexander et al.* (2010c)]. Note that although different values of CPV_{goal} were used, the computational effort (excluding motor map sample generation) remained nearly the same (approximately 0.97 s) in constructing each model.

Table 4.2 Number of POD Coefficients for Distinct CPV_{goal} Values

POD Coefficient Vector	CPV_{goal}		
	99.99%	99.95%	99.85%
$\mathbf{z}_{r,max}$	14	9	7
$\mathbf{z}_{r,min}$	13	9	7
$\mathbf{z}_{r,pLoss}$	89	59	44

The accuracy of the POD representations for each value of CPV_{goal} was quantified through AVASIM. In particular, both 1D and 2D formulations were applied as appropriate using a uniform tolerance of $tol_i = 0.10$ to assess the accuracy of the torque curves and power loss map produced by the POD representations against the optimal torque curves and power loss map produced by $\mathbf{f}_{motor}$ from the AiO optimization problem. Note that like the demonstration in Chapter 2, all phase threshold coefficients were set to zero, and division-by-zero errors were avoided by setting $\delta = 10^{-4}$ for the torque curves and $\delta = 1$ for the power loss map based on experience. Also, observe that selecting the AiO optimal motor map as the basis for comparison was reasonable given the fact that it is most desirable to have high motor map accuracy at the design solution. Finally, Tables 4.3-4.5 show the results from AVASIM, which are supplemented by visual comparisons in Figures 4.3-4.8. Using this information, it is evident that the most accurate POD representation for this work occurs at CPV_{goal} = 99.99% [*Alexander et al.* (2010c)].

Table 4.3 AVASIM Results for POD, CPV_{goal} = 99.99%

Index	Max-Torque	Min-Torque	Power Loss
E_{local}	0.951	0.979	0.686
E_{global}	0.976	0.979	0.932
E_{comb}	0.964	0.979	0.809

Table 4.4 AVASIM Results for POD, CPV_{goal} = 99.95%

Index	Max-Torque	Min-Torque	Power Loss
E_{local}	0.920	0.967	0.399
E_{global}	0.940	0.958	0.862
E_{comb}	0.930	0.963	0.630

Table 4.5 AVASIM Results for POD, CPV_{goal} = 99.85%

Index	Max-Torque	Min-Torque	Power Loss
E_{local}	0.772	0.934	0.039
E_{global}	0.899	0.928	0.830
E_{comb}	0.836	0.931	0.435

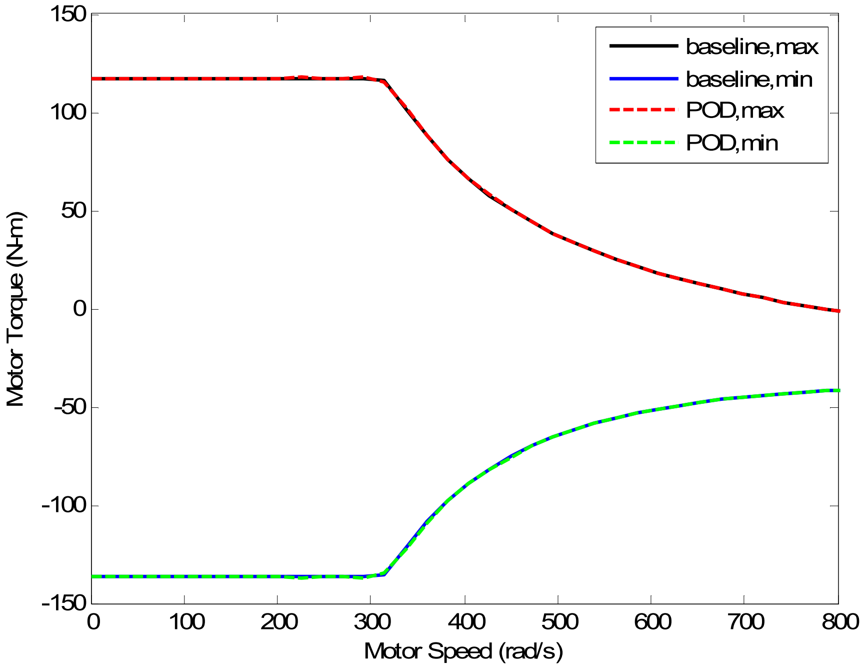

Figure 4.3 Torque Curve Comparison at CPV_{goal} = 99.99%

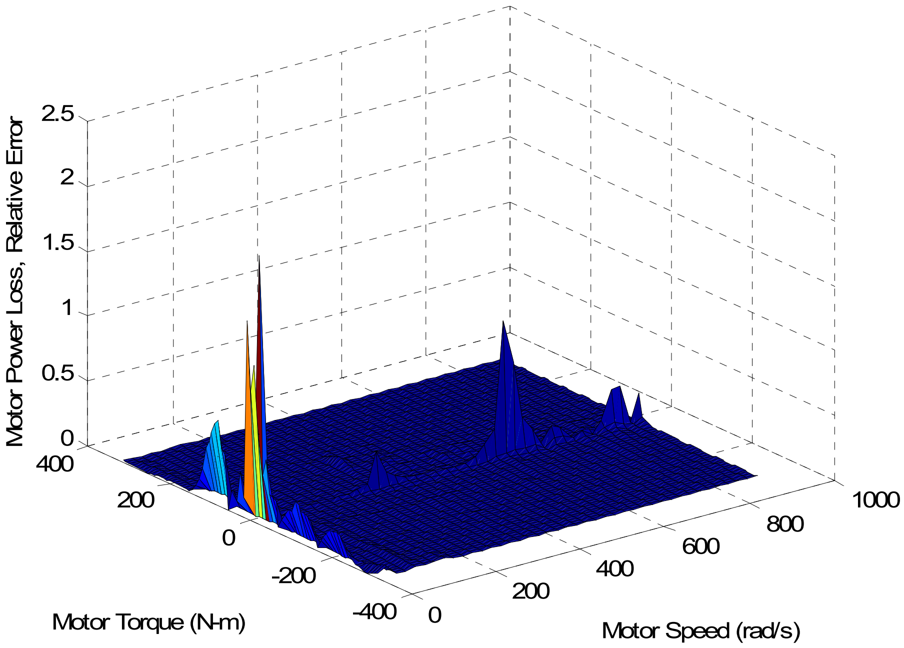

Figure 4.4 Power Loss Map Relative Error at CPV_{goal} = 99.99%

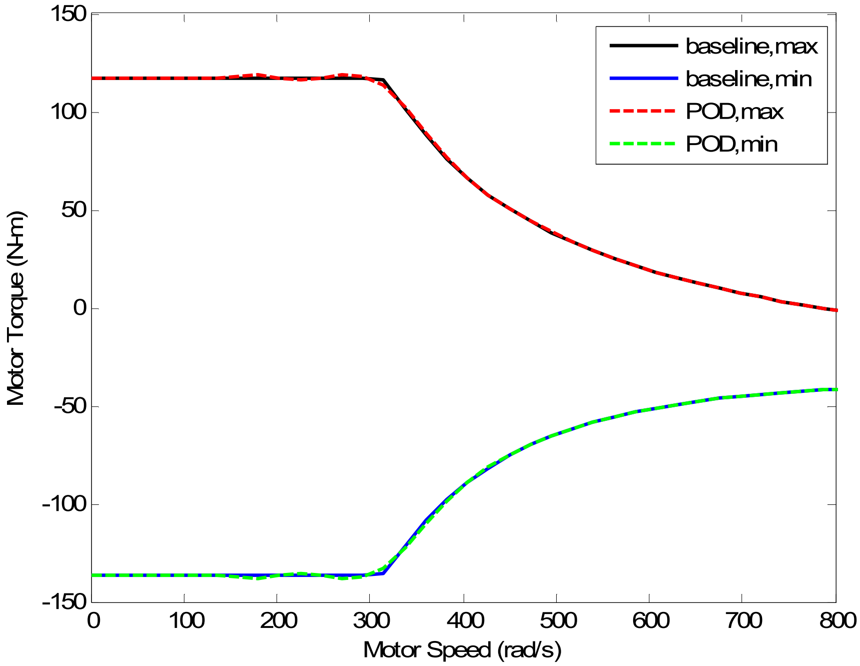

Figure 4.5 Torque Curve Comparison at CPV_{goal} = 99.95%

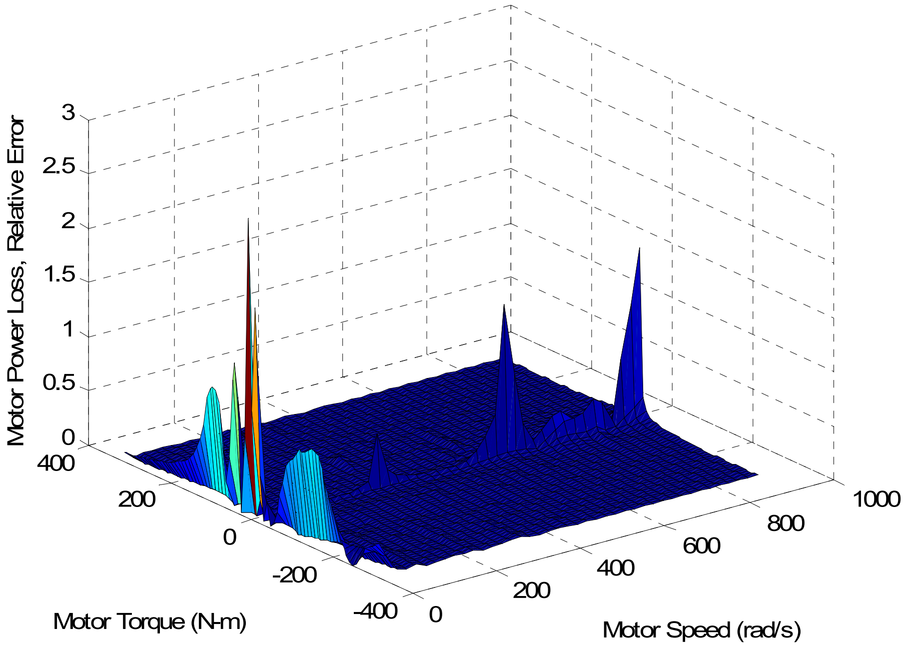

Figure 4.6 Power Loss Map Relative Error at CPV_{goal} = 99.95%

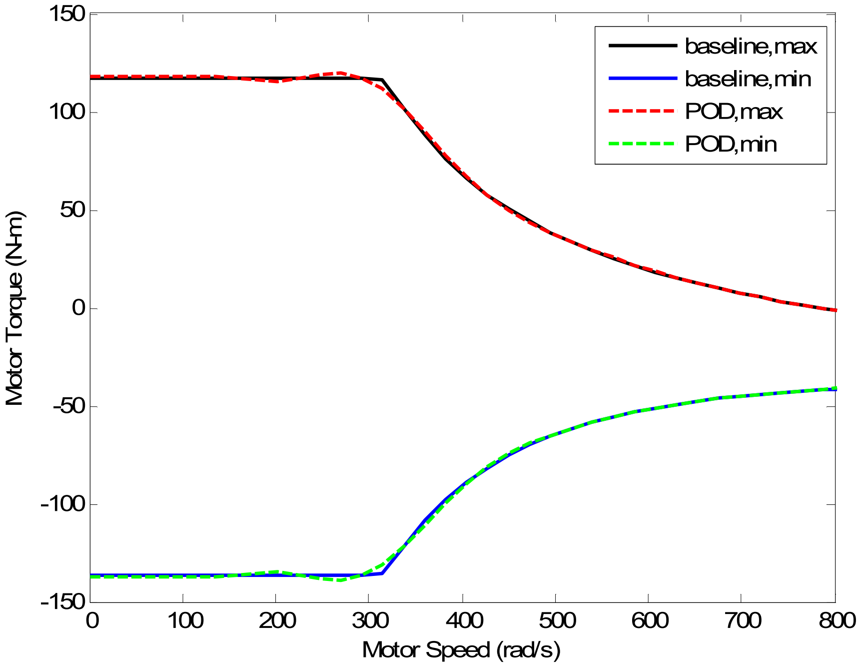

Figure 4.7 Torque Curve Comparison at CPV_{goal} = 99.85%

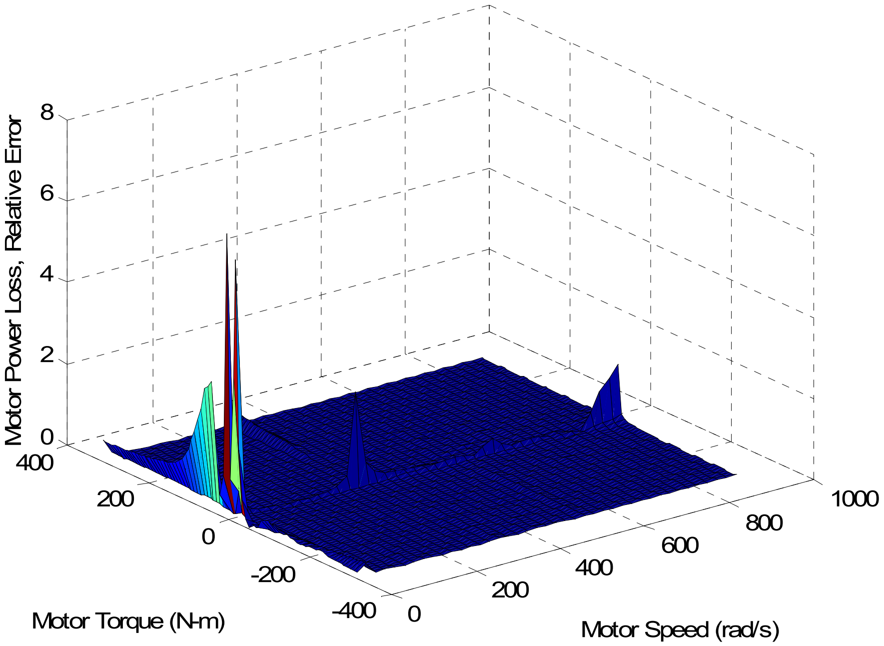

Figure 4.8 Power Loss Map Relative Error at CPV_{goal} = 99.85%

4.3 ATC Problem Formulation and Solutions

The ATC problem formulation for the commercial EV consists of a two-level hierarchical decomposition based on Figure 3.2. In this study, the objective of the vehicle subproblem is to maximize the gasoline-equivalent fuel economy while minimizing the AL penalty function, whereas the objective of the motor subproblem is to minimize the AL penalty function exclusively. Recall that these penalty functions ensure consistency, or agreement, among the coupled quantities from the vehicle and motor subproblems. Although both subproblems are subject to decision variable bound constraints, only the vehicle subproblem contains additional constraints based on battery packaging, performance, motor feasibility, vehicle range, power availability, and battery capacity.

Applying Equation (2.2) directly, the vehicle subproblem P_{11}, excluding decision variable bound constraints, is formulated as

$$
\begin{aligned}
&\min_{\bar{\mathbf{x}}_{11}} \; -mpg_e(\bar{\mathbf{x}}_{11}) + \mathbf{v}_{22}^T(\mathbf{t}_{22} - \mathbf{r}_{22}) + \left\| \mathbf{w}_{22} \circ (\mathbf{t}_{22} - \mathbf{r}_{22}) \right\|_2^2 \\
&\textit{subject to} \\
&\qquad \begin{array}{ll}
g_{11,1} = b_{w,V}(\bar{\mathbf{x}}_{11}) \le 0 & g_{11,5} = \omega_V(\bar{\mathbf{x}}_{11}) \le 0 \\
g_{11,2} = b_{\ell,V}(\bar{\mathbf{x}}_{11}) \le 0 & g_{11,6} = R_{min} - R(\bar{\mathbf{x}}_{11}) \le 0 \\
g_{11,3} = t_{60}(\bar{\mathbf{x}}_{11}) - t_{60max} \le 0 & g_{11,7} = P_V(\bar{\mathbf{x}}_{11}) \le 0 \\
g_{11,4} = \tau_V(\bar{\mathbf{x}}_{11}) \le 0 & g_{11,8} = C_b(\bar{\mathbf{x}}_{11}) - C_{bmax}(\bar{\mathbf{x}}_{11}) \le 0
\end{array} \\
&\textit{where} \\
&\qquad \bar{\mathbf{x}}_{11} = [B_I, B_W, B_L, x_{batt}, p_r, \mathbf{z}_{r,comb}^T, \omega_{max}^T, m_m^T, J_r^T, I_{ym}^T, I_{zm}^T, y_m^T] \\
&\qquad \mathbf{t}_{22} = [\mathbf{z}_{comb}^T, \omega_{max}^T, m_m^T, J_r^T, I_{ym}^T, I_{zm}^T, y_m^T],\; \mathbf{z}_{comb}^T = \mathbf{f}(\mathbf{z}_{r,comb}^T) \\
&\qquad \mathbf{r}_{22} = [\mathbf{z}_{comb}^R, \omega_{max}^R, m_m^R, J_r^R, I_{ym}^R, I_{zm}^R, y_m^R]
\end{aligned}
\tag{4.8}
$$

where the constraints $g_{11,1}$-$g_{11,8}$ are identical to the constraints g_1-g_8 from the AiO problem formulation. The vectors $\mathbf{z}_{comb} = [\mathbf{z}_{max}, \mathbf{z}_{min}, \mathbf{z}_{pLoss}]$ and $\mathbf{z}_{r,comb} = [\mathbf{z}_{r,max}, \mathbf{z}_{r,min}, \mathbf{z}_{r,pLoss}]$ refer to the combined vector of original VVCVs and the combined vector of reduced representation variables, which are POD coefficients. Additionally, the vectors $\mathbf{t}_{22}$ and $\mathbf{r}_{22}$ include six scalar-valued coupling variables: ω_{max}, m_m, J_r, I_{ym}, I_{zm}, and y_m. Finally, the superscripts T and R denote target and response versions of the same coupling variable, respectively. The motor subproblem P_{22}, excluding decision variable bound constraints, is formulated in a similar manner as:

$$\begin{aligned}
&\min_{\bar{\mathbf{x}}_{22}} \mathbf{v}_{22}^T(\mathbf{t}_{22}-\mathbf{r}_{22}) + \left\|\mathbf{w}_{22}\circ(\mathbf{t}_{22}-\mathbf{r}_{22})\right\|_2^2 \\
&where\ \ \bar{\mathbf{x}}_{22} = [\ell_s, r_m, n_c, R_r] \\
&\qquad\quad \mathbf{t}_{22} = [\mathbf{z}_{comb}^T, \omega_{max}^T, m_m^T, J_r^T, I_{ym}^T, I_{zm}^T, y_m^T] \\
&\qquad\quad \mathbf{r}_{22} = [\mathbf{z}_{comb}^R, \omega_{max}^R, m_m^R, J_r^R, I_{ym}^R, I_{zm}^R, y_m^R] = \mathbf{f}(\bar{\mathbf{x}}_{22})
\end{aligned} \tag{4.9}$$

Recent work [*Alexander et al.* (2010a)] indicated that the assumption that only bound constraints were necessary for the reduced representation variables was incorrect; instead, the model validity region (and hence decision space) defined by these variables was highly-nonlinear. As mentioned in Chapter 1, such an erroneous assumption initially resulted in powertrain simulation failures at decision vectors selected outside the model validity region. Because it was challenging to formulate explicit constraints for these abstract variables, a penalty value-based heuristic [*Alexander et al.* (2010a); *Alexander et al.* (2010b)] was developed through a MATLAB® "try-catch" statement to help keep the optimizer within the model validity region. NOMADm was selected as the optimizer again in order to facilitate consistent results with the AiO problem formulation and to effectively implement the penalty value-based heuristic. In the P_{11} subproblem, the default settings for NOMADm were adjusted such that only a Latin hypercube search was performed and 1,000 function evaluations were permitted. This was necessary to alleviate computational issues associated with memory availability. However, in the P_{22} subproblem, the default settings for NOMADm were appropriate. Finally, in the ATC coordination strategy, the weight update parameter was set to $\beta = 2.75$, the initial weight vectors were set to $\mathbf{v} = \mathbf{0}$ and $\mathbf{w} = \mathbf{1}$, and the tolerance on $\|\mathbf{c}^{(K)} - \mathbf{c}^{(K-1)}\|_\infty$ for outer loop convergence was set to 10^{-2}. Note that all computational work was performed on a 3 GHz, 4 MB RAM, Intel® Core™ 2 Duo CPU.

4.3.1 ATC-AL-POD at $CPV_{goal} = 99.99\%$

In Tables 4.6-4.8, the ATC optimization results using the POD representations at $CPV_{goal} = 99.99\%$ are shown. The algorithm converged after 12 ATC iterations with a runtime of approximately 10.72 hours and resulted in a system solution that was reasonably consistent between both subproblems. The only active constraints were the upper bound on ω_{max}^T, the performance constraint $g_{11,3}$, and the battery capacity constraint $g_{11,8}$ in the P_{11} subproblem; these were limited to $\omega_{max}^T = 755$ rad/s, $t_{60max} = 10$ s, and $C_{bmax} = 200$ Ah, respectively. Note that the battery capacity limit is meaningful as it is used indirectly to avoid excessive battery cost. The optimal values of the POD coefficients are not listed here as they are too numerous and not physically meaningful; however, the optimal motor map computed by these reduced representation variables is shown in Figure 4.9. Finally, the total mass of the vehicle was 1111 kg, with approximately 14.3% (158 kg) of the mass associated with the battery. Under these design conditions, the commercial EV is expected to have a gasoline-equivalent fuel economy of $mpg_e = 184$ mpg and a range of $R = 134$ miles.

Table 4.6 Optimal Decision Vector for P_{11} Subproblem, $CPV_{goal} = 99.99\%$

B_I	B_W	B_L	x_{batt}	p_r	ω_{max}^T	m_m^T	J_r^T	I_{ym}^T	I_{zm}^T	y_m^T
0.74	1.43	19.75	0.25	3.13	755	40.39	0.28	1.12	1.20	0.39

Table 4.7 Optimal Decision Vector for P_{22} Subproblem, $CPV_{goal} = 99.99\%$

ζ_s	r_m	n_c	R_r
0.098	0.123	17.62	0.053

Table 4.8 Optimal Consistency Constraint Vector/Weights, $CPV_{goal} = 99.99\%$

Consistency Constraint	c_{opt}	v_{opt}	w_{opt}
$c_{z,max}$	0.45	6.37×10^{8}	6.80×10^{4}
$c_{z,min}$	0.41	5.82×10^{8}	6.80×10^{4}
$c_{z,pLoss}$	0.73	1.01×10^{9}	6.80×10^{4}
$c_{\omega max}$	0	0	6.80×10^{4}
c_{mm}	-0.46	-6.53×10^{8}	6.80×10^{4}
c_{Jr}	0	1.51×10^{6}	6.80×10^{4}
c_{Iym}	0	5.93×10^{6}	6.80×10^{4}
c_{Izm}	-0.02	-3.21×10^{7}	6.80×10^{4}
c_{ym}	0	3.67×10^{6}	6.80×10^{4}

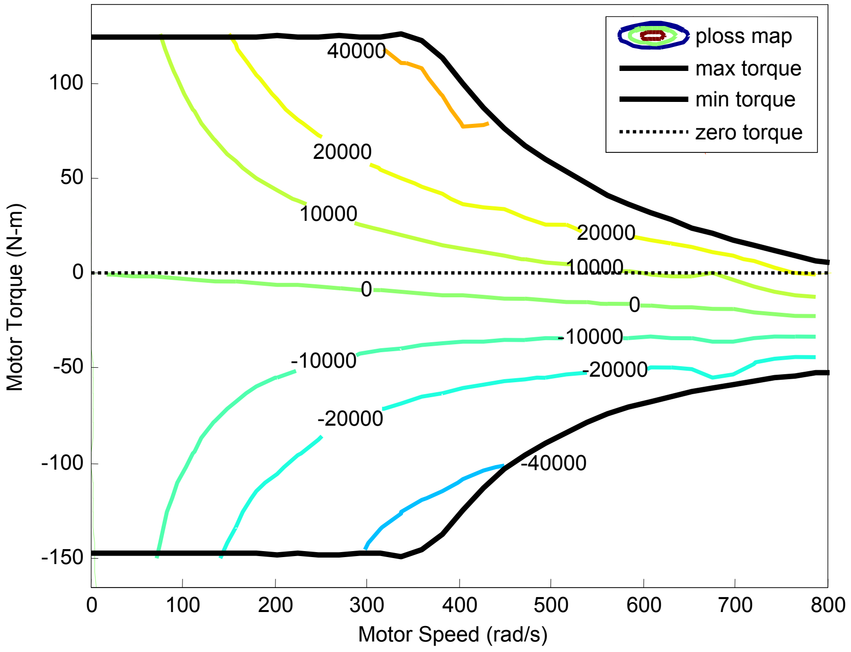

Figure 4.9 Optimal Motor Map, $CPV_{goal} = 99.99\%$

4.3.2 ATC-AL-POD at $CPV_{goal} = 99.95\%$

Similarly, in Tables 4.9-4.11, the ATC optimization results using the POD representations at $CPV_{goal} = 99.95\%$ are shown. The algorithm converged after 18 ATC iterations with a runtime of approximately 16.81 hours and resulted in a system solution that was reasonably consistent between both subproblems. Again, the only active constraints were the upper bound on $\omega_{max}{}^{T}$, the performance constraint $g_{11,3}$, and the battery capacity constraint $g_{11,8}$ in the P_{11} subproblem; these were limited to $\omega_{max}^T = 755$ rad/s, $t_{60max} = 10$ s, and $C_{bmax} = 200$ Ah, respectively. The optimal motor map computed by the POD coefficients is shown in Figure 4.10. Finally, the total mass of the vehicle was 1111 kg, with approximately 14.3% (158 kg) of the mass associated with the battery. Under these design conditions, the EV is expected to have a gasoline-equivalent fuel economy of $mpg_e = 180$ mpg and a range of $R = 132$ miles.

Table 4.9 Optimal Decision Vector for P_{11} Subproblem, CPV_{goal} = 99.95%

B_I	B_W	B_L	x_{batt}	p_r	ω_{max}^T	m_m^T	J_r^T	I_{ym}^T	I_{zm}^T	y_m^T
0.74	1.43	19.75	0.05	3.13	755	40.39	0.28	1.12	1.20	0.39

Table 4.10 Optimal Decision Vector for P_{22} Subproblem, CPV_{goal} = 99.95%

ζ_s	r_m	n_c	R_r
0.104	0.121	17.08	0.057

Table 4.11 Optimal Consistency Constraint Vector/Weights, CPV_{goal} = 99.95%

Consistency Constraint	c_{opt}	v_{opt}	w_{opt}
$c_{z,max}$	0.76	3.09×10^{14}	2.94×10^{7}
$c_{z,min}$	0.74	3.17×10^{14}	2.94×10^{7}
$c_{z,pLoss}$	1.59	4.49×10^{14}	2.94×10^{7}
$c_{\omega max}$	0	0	2.94×10^{7}
c_{mm}	-1.42	-2.95×10^{14}	2.94×10^{7}
c_{Jr}	0	1.35×10^{12}	2.94×10^{7}
c_{Iym}	0.01	5.37×10^{12}	2.94×10^{7}
c_{Izm}	-0.07	-1.54×10^{13}	2.94×10^{7}
c_{ym}	0.01	1.92×10^{12}	2.94×10^{7}

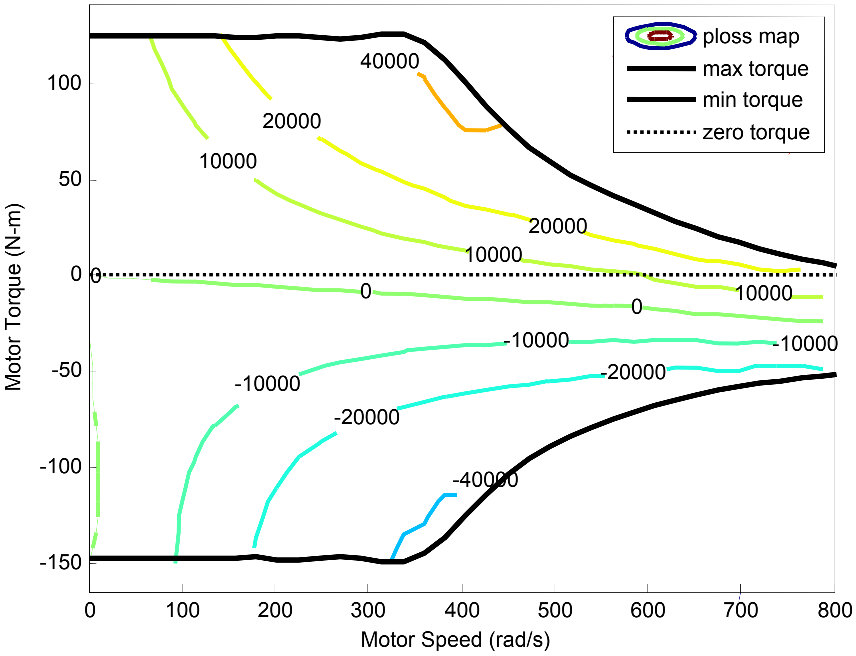

Figure 4.10 Optimal Motor Map, $CPV_{goal} = 99.95\%$

4.3.3 ATC-AL-POD at $CPV_{goal} = 99.85\%$

Finally, in Tables 4.12-4.14, the ATC optimization results using the POD representations at $CPV_{goal} = 99.85\%$ are shown. The algorithm converged after 66 ATC iterations with a runtime of approximately 59.41 hours and resulted in a system solution that was reasonably consistent between both subproblems. Once again, the only active constraints were the upper bound on ω_{max}^T, the performance constraint $g_{11,3}$, and the battery capacity constraint $g_{11,8}$ in the P_{11} subproblem; these were limited to $\omega_{max}^T = 755$ rad/s, $t_{60max} = 10$ s, and $C_{bmax} = 200$ Ah, respectively. The optimal motor map computed by the POD coefficients is shown in Figure 4.11. Finally, the total mass of the vehicle was 1124 kg, with approximately 14.1% (158 kg) of the mass associated with the battery. Under these design conditions, the EV is expected to have a gasoline-equivalent fuel economy of $mpg_e = 181$ mpg and a range of $R = 132$ miles.

Table 4.12 Optimal Decision Vector for P_{11} Subproblem, $CPV_{goal} = 99.85\%$

B_I	B_W	B_L	x_{batt}	p_r	ω_{max}^T	m_m^T	J_r^T	I_{ym}^T	I_{zm}^T	y_m^T
0.74	1.43	19.75	0.25	3.13	755	46.79	0.28	1.12	1.20	0.39

Table 4.13 Optimal Decision Vector for P_{22} Subproblem, CPV_{goal} = 99.85%

ℓ_s	r_m	n_c	R_r
0.121	0.116	15.67	0.095

Table 4.14 Optimal Consistency Constraint Vector/Weights, CPV_{goal} = 99.85%

Consistency Constraint	c_{opt}	v_{opt}	w_{opt}
$c_{z,max}$	1.11	4.42×10^{56}	3.60×10^{28}
$c_{z,min}$	0.95	3.85×10^{56}	3.60×10^{28}
$c_{z,pLoss}$	1.59	2.50×10^{56}	3.60×10^{28}
$c_{\omega max}$	0	0	3.60×10^{28}
c_{mm}	1.91	7.55×10^{56}	3.60×10^{28}
c_{Jr}	0.01	2.34×10^{54}	3.60×10^{28}
c_{Iym}	0.02	9.34×10^{54}	3.60×10^{28}
c_{Izm}	-0.05	-1.84×10^{55}	3.60×10^{28}
c_{ym}	0.03	9.89×10^{54}	3.60×10^{28}

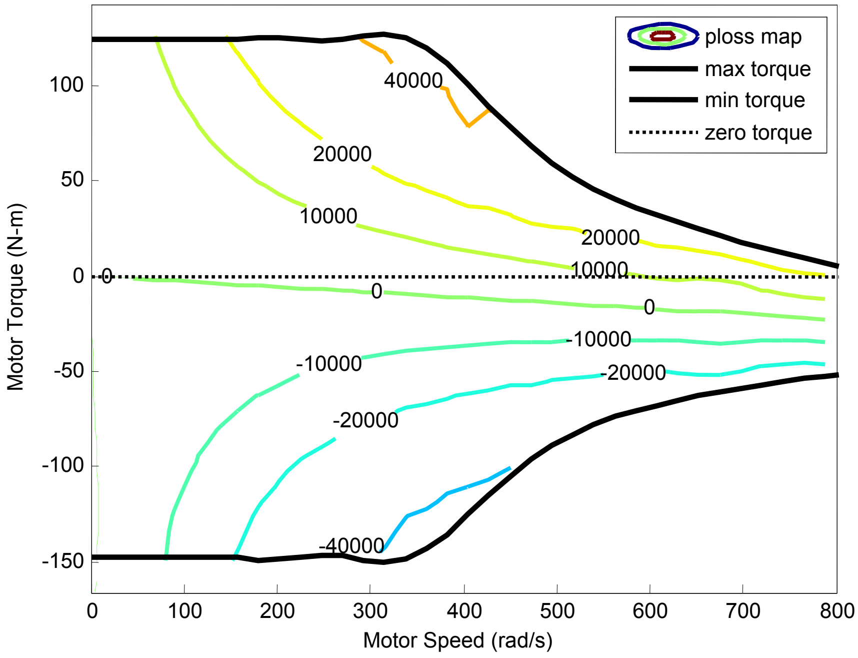

Figure 4.11 Optimal Motor Map, CPV_{goal} = 99.85%

4.3.4 Summary of ATC Results

It is evident from the optimization results that a relaxation in CPV_{goal} leads to a reduction in the accuracy of the ATC design solutions, which are given by $\mathbf{x}_*^{ATC} = [B_I, B_W, B_L, x_{batt}, p_r, \ell_s, r_m, n_c, R_r]$. In particular, it is seen that the errors between the expected design solution (AiO) and the ATC design solutions are $\frac{\left\|\mathbf{x}_*^{AiO} - \mathbf{x}_*^{ATC}\right\|_2}{\left\|\mathbf{x}_*^{AiO}\right\|_2} = 0.113$, $\frac{\left\|\mathbf{x}_*^{AiO} - \mathbf{x}_*^{ATC}\right\|_2}{\left\|\mathbf{x}_*^{AiO}\right\|_2} = 0.131$, and $\frac{\left\|\mathbf{x}_*^{AiO} - \mathbf{x}_*^{ATC}\right\|_2}{\left\|\mathbf{x}_*^{AiO}\right\|_2} = 0.180$ for CPV_{goal} = 99.99%, CPV_{goal} = 99.95%, and CPV_{goal} = 99.85%, respectively. Note that this measure for solution accuracy is preferred for ATC instead of $\frac{| f_*^{AiO} - f_*^{ATC} |}{| f_*^{AiO} |}$ since it does not require exact system consistency (**c** = **0**) and it assesses the error in the design, which can be directly modified, rather than the error in the prediction, which cannot be directly modified and is dependent on the fidelity of the analysis models. Moreover, similar measures have been used in well-established literature [*Tosserams et al.* (2006)] when comparing multiple ATC solutions. Hence, using this measure, it can be seen that the loss of accuracy in the ATC design solutions is linked to the loss of accuracy in the POD representations as indicated by the AVASIM results.

An interesting outcome from this study is that a reduction in CPV_{goal} does not necessarily accelerate ATC convergence; instead, the optimization strategy may become more inefficient. This is clearly observed through the ATC runtimes, which were 10.72 hours, 16.81 hours, and 59.41 hours for CPV_{goal} = 99.99%, CPV_{goal} = 99.95%, and CPV_{goal} = 99.85%, respectively. However, the average ATC convergence rate for each case, which is the total number of ATC iterations divided by the runtime, suggests that the longer runtimes for lower CPV values were caused by an increase in the number of ATC iterations. In particular, the average ATC convergence rates were 1.12 iterations/hr, 1.07 iterations/hr, and 1.11 iterations/hr for CPV_{goal} = 99.99%, CPV_{goal} = 99.95%, and CPV_{goal} = 99.85%, respectively. Since these convergence rates were relatively constant for each case (within 5% of each other at worst), it can be reasonably concluded that the cause of the longer runtimes was in fact the increased number of ATC iterations.

Recall that the number of ATC iterations is driven by $||\mathbf{c}^{(K)} - \mathbf{c}^{(K-1)}||_\infty$, which must be less than 10^{-2} for outer loop convergence in these studies. Closer inspection of the consistency values and associated penalty weights in Tables 4.8, 4.11, and 4.14 reveals that the outer loop convergence (and hence the number of ATC iterations) was ultimately dictated by the consistency of $\mathbf{z}_{max}$, $\mathbf{z}_{min}$, $\mathbf{z}_{pLoss}$, and m_m. These variables had the largest consistency values and weights in terms of magnitude for each case. Also, note that the consistency values for these variables were on the order of at least 10^{-1}, which implies that the reductions in these values during an ATC iteration could have been as large as 10^{-1}. Such behavior would inhibit outer loop convergence and hence require more ATC iterations. However, this behavior alone does not explain the counterintuitive results with respect to optimization efficiency when using lower fidelity POD representations. This instead can be traced back to the available degrees of freedom for achieving consistency of $\mathbf{z}_{max}$, $\mathbf{z}_{min}$, $\mathbf{z}_{pLoss}$, and m_m in both subproblems as well as the relationship among the local design variables that compute them in the motor subproblem. In the P_{11} subproblem, $\mathbf{z}_{max}$, $\mathbf{z}_{min}$, and $\mathbf{z}_{pLoss}$ are functions of the decision variables $\mathbf{z}_{r,max}$, $\mathbf{z}_{r,min}$, and $\mathbf{z}_{r,pLoss}$, whereas m_m is treated as an independent decision variable. However, in the P_{22} subproblem, $\mathbf{z}_{max}$, $\mathbf{z}_{min}$, and $\mathbf{z}_{pLoss}$ are functions of the local design variables ℓ_s, r_m, n_c, and R_r, whereas the m_m is a function the local design variables ℓ_s and r_m. This means that there are $(p_{max} + p_{min} + p_{pLoss} + 4)$ degrees of freedom to achieve consistency for the motor map ($[\mathbf{z}_{max}, \mathbf{z}_{min}, \mathbf{z}_{pLoss}]$) and 3 degrees of freedom to achieve consistency for the motor mass. Using this information, it becomes clear why the lower fidelity POD representations required more ATC iterations: these approximations had fewer degrees of freedom to match the high-fidelity motor maps generated by the P_{22} subproblem, and the optimizer had to balance the requirements for achieving consistency for both the motor map and motor mass. Specifically, as the number of reduced representation variables decreased in the P_{11} subproblem, the sensitivity of the motor map and motor mass consistencies increased with respect to ℓ_s and r_m in the P_{22} subproblem. It is believed that this behavior led to large, frequent fluctuations in $||\mathbf{c}^{(K)} - \mathbf{c}^{(K-1)}||_\infty$ and thus resulted in more ATC iterations and longer runtimes.

4.4 Conclusions

Based on the accuracy of the ATC solutions and their corresponding runtimes, it can be concluded that the best POD representation within ATC for this study is associated with CPV_{goal} = 99.99% [*Alexander et al.* (2010c)]. This case had both the highest accuracy and the fastest runtime. From a broader perspective, it can be reasonably concluded that high-fidelity POD representations are generally more appropriate for reduced representation of VVCVs in ATC. This is because low-fidelity POD representations will usually lead to less accurate design solutions and will frequently lead to longer runtimes via more outer loop iterations. The exceptions to this might be for design problems in which there is less interaction among the VVCVs and other coupling variables, or for design problems in which extremely low-fidelity POD representations (CPV_{goal} << 99%) are used. For example, in the former case, if the motor mass would have been eliminated as a coupling variable, then perhaps the runtimes for the low-fidelity POD representations would have been nearly the same or even slightly faster than the high-fidelity POD representation. In the latter case, using extremely low-fidelity POD representations might decrease the runtime directly through significantly faster approximations per ATC iteration. However, in both cases, the design solution accuracy would still be compromised, and one would have to assess whether this would be worth any additional computational savings. Hence, in the future, this work can be made more comprehensive by experimenting with these design scenarios and examining other optimization metrics, like the problem condition, as a function of CPV_{goal}. Additionally, from a design perspective, this study can be enhanced by developing an explicit cost model that explores tradeoffs between extended range/improved performance and battery cost.

4.5 Summary

This chapter explored the design optimization of a commercial EV powertrain. Specifically, an AiO problem formulation was introduced and solved as well as an ATC problem formulation that used POD for the reduced representation of motor map functional data. In an effort to identify the effect of the POD representation accuracy on the ATC solution accuracy, the latter problem formulation was solved three times using different sets of POD representations based on the CPV. It was hypothesized that as the CPV (and hence POD representation accuracy) was reduced, the ATC solution time would significantly decrease due to the use of fewer reduced representation variables (POD coefficients). However, it was discovered that as the CPV was reduced, the ATC solution time was significantly compromised as well as the design solution accuracy. This led to the conclusion that high-fidelity POD representations would be most appropriate for the reduced representation of VVCVs in ATC because of their good accuracy and enhanced capability of achieving functional data consistency through additional degrees of freedom (reduced representation variables). The next chapter will build off of these results by examining how different measures of consistency will impact the ATC solution with respect to the interpretation of functional data consistency and overall solution accuracy.

Chapter 5

Consistency Measures for Functional Data in Analytical Target Cascading

The importance of identifying appropriate error metrics for the validation of functional data approximations against their high-fidelity counterparts was discussed in Chapter 1. Specifically, it was mentioned that many of the existing error metrics were developed for 1D applications and that their performance and suitability for higher dimensional functional data was largely unexplored. In recent work [*Alexander and Papalambros* (2010)], this problem was addressed by extending an error metric known as AVASIM to 2D applications as this algorithm systematically, objectively and efficiently provides a clear indication of local and global functional data accuracy with respect to preset thresholds [*Sohns et al.* (2006)]. The results from this work as presented in Chapter 2 demonstrated that both the 1D and 2D AVASIM formulations provide reasonable predictions of local and global functional data accuracy. However, the primary motivation for exploring the capability of AVASIM for higher dimensional functional data is its potential impact on decomposition-based design optimization strategies containing coupled, functional data. Since ATC convergence, for example, is ultimately based on the discrepancy between coupled quantities from distinct subproblems, it is necessary to implement accurate and meaningful consistency measures for functional data that lead to physically realizable optimal design solutions. As mentioned earlier, no well-established consistency measure exists for coupled functional data within decomposition-based optimization strategies in the literature, and so previous work has somewhat arbitrarily used a RMSE consistency measure [*Alexander* (2008); *Alexander et al.* (2009); *Alexander et al.* (2010a); *Alexander et al.* (2010b); *Alexander et al.* (2010c)].

Nevertheless, such a measure may not be appropriate for higher dimensional functional data (such as 2D motor power loss maps) and lacks a clear definition of consistency among coupled functional data. The current chapter therefore explores this issue by implementing RMSE, AVASIM, and a generalized version of AVASIM independently in an ATC problem formulation for the commercial EV powertrain model and comparing their respective design solutions.

5.1 Consistency Measures

As originally developed, the definition for the relaxed consistency constraints in ATC ($\mathbf{c}_{ij} = \mathbf{t}_{ij} - \mathbf{r}_{ij}$) is only applicable for scalar-valued coupling variables; when these terms consist of functional data, the definition must be modified based on the error metric desired for measuring consistency. For example, in the previous chapter and in other related work [*Alexander* (2008); *Alexander et al.* (2009); *Alexander et al.* (2010a); *Alexander et al.* (2010b); *Alexander et al.* (2010c)], the consistency between functional data was measured through RMSE as

$$c_{ij,l} = \sqrt{\frac{\sum_{m=1}^{Q}(t_{ij,m} - r_{ij,m})^2}{Q}} \tag{5.1}$$

for the l^{th}-component of $\mathbf{c}_{ij}$, where Q denotes the number of discretized points defining the functional data. Because functional data consistency in this study will also be measured through AVASIM and generalized AVASIM, an alternative definition [*Alexander and Papalambros* (2010)] for the relaxed consistency constraints is

$$c_{ij,l} = 1 - E_{comb,l} \tag{5.2}$$

where $E_{comb,l}$ is computed through Equations (2.13)-(2.22) with $t_{ij,m}$ and $r_{ij,m}$ substituted for y_i and $\hat{y}_i$ and w_{local} and w_{global} set as appropriate. Observe that for both RMSE and the AVASIM approaches, the definition of consistency is similar to that of the scalar-valued case; that is, when $c_{ij,l} = 0$, the coupling variables match exactly, whereas if $c_{ij,l} \neq 0$, some discrepancy exists between the coupling variables. However, using AVASIM or generalized AVASIM enhances the meaning of consistency since $c_{ij,l} = 1$ indicates that the functional data are consistent and at the threshold, and $c_{ij,l} > 1$ indicates that the functional data are inconsistent [*Alexander and Papalambros* (2010)].

5.2 ATC Problem Formulation and Solutions

The ATC problem formulation for the commercial EV powertrain model shown in Equations (4.8)-(4.9) provides the basis for this study. Because the problem structure requires reduced representations for VVCVs associated with the motor torque curves and power loss map, the POD representations developed at CPV_{goal} = 99.99% were used. Like the previous chapter, the design problem for each consistency measure was solved using NOMADm. The default settings of this optimizer were modified for the P_{11} subproblem such that only a Latin hypercube search was performed and 1,000 function evaluations were permitted. This was necessary to alleviate computational issues associated with memory availability. However, for the P_{22} subproblem, the default settings were sufficient. In the ATC coordination strategy, the weight update parameter was set to $\beta = 2.75$, and the initial weight vectors for both subproblems were set to $\mathbf{v} = \mathbf{0}$ and $\mathbf{w} = \mathbf{1}$. Since the RMSE consistency measure served as the baseline in this study, its associated tolerance on $||\mathbf{c}^{(K)} - \mathbf{c}^{(K-1)}||_\infty$ for outer loop convergence was set to 10^{-2}; for the other consistency measures, the coordination strategy was repeated until the number of ATC iterations was identical to the RMSE case. Such a modification was necessary for an equitable comparison of the optimization results [*Alexander and Papalambros* (2010)]. Once again, all computational work was performed on a 3GHz, 4 MB RAM, Intel® Core™ 2 Duo CPU.

5.2.1 RMSE Consistency Measure in ATC

The ATC optimization results using RMSE as a consistency measure for the functional data are shown in Tables 5.1-5.3. Note that these results are identical to those in Chapter 4 for POD at CPV_{goal} = 99.99% but are repeated here to facilitate comparisons with the other consistency measures. Also, to avoid ill-performance of the RMSE consistency measure due to the vast difference in magnitudes between the torque curves and power loss map, Equation (5.1) was modified for the power loss map such that ($t_{ij,m} - r_{ij,m}$) was normalized by its associated baseline power loss value before being squared when the baseline power loss value exceeded 1 W in magnitude. Convergence was achieved after 12 ATC iterations with a runtime of approximately 10.72 hours and resulted in a system solution that was reasonably consistent between both subproblems. Recall that the only active constraints were the upper bound on ω_{max}^T, the performance constraint $g_{11,3}$, and the battery capacity constraint $g_{11,8}$ in the P_{11} subproblem; these were limited to ω_{max}^T = 755 rad/s, t_{60max} = 10 s, and C_{bmax} = 200 Ah, respectively. The optimal motor map computed by the POD coefficients is shown in Figure 5.1. Finally, the total mass of the vehicle was 1111 kg, with approximately 14.3% (158 kg) of the mass associated with the battery. With such a design, the EV could achieve a gasoline-equivalent fuel economy of mpg_e = 184 mpg and a range of R = 134 miles.

Table 5.1 Optimal Decision Vector for P_{11} Subproblem, RMSE Consistency

B_I	B_W	B_L	x_{batt}	p_r	ω_{max}^T	m_m^T	J_r^T	I_{ym}^T	I_{zm}^T	y_m^T
0.74	1.43	19.75	0.25	3.13	755	40.39	0.28	1.12	1.20	0.39

Table 5.2 Optimal Decision Vector for P_{22} Subproblem, RMSE Consistency

l_s	r_m	n_c	R_r
0.098	0.123	17.62	0.053

Table 5.3 Optimal Consistency Constraint Vector/Weights, RMSE Consistency

Consistency Constraint	c_{opt}	v_{opt}	w_{opt}
$c_{z,max}$	0.45	6.37×10^8	6.80×10^4
$c_{z,min}$	0.41	5.82×10^8	6.80×10^4
$c_{z,pLoss}$	0.73	1.01×10^9	6.80×10^4
$c_{\omega max}$	0	0	6.80×10^4
c_{mm}	-0.46	-6.53×10^8	6.80×10^4
c_{Jr}	0	1.51×10^6	6.80×10^4
c_{Iym}	0	5.93×10^6	6.80×10^4
c_{Izm}	-0.02	-3.21×10^7	6.80×10^4
c_{ym}	0	3.67×10^6	6.80×10^4

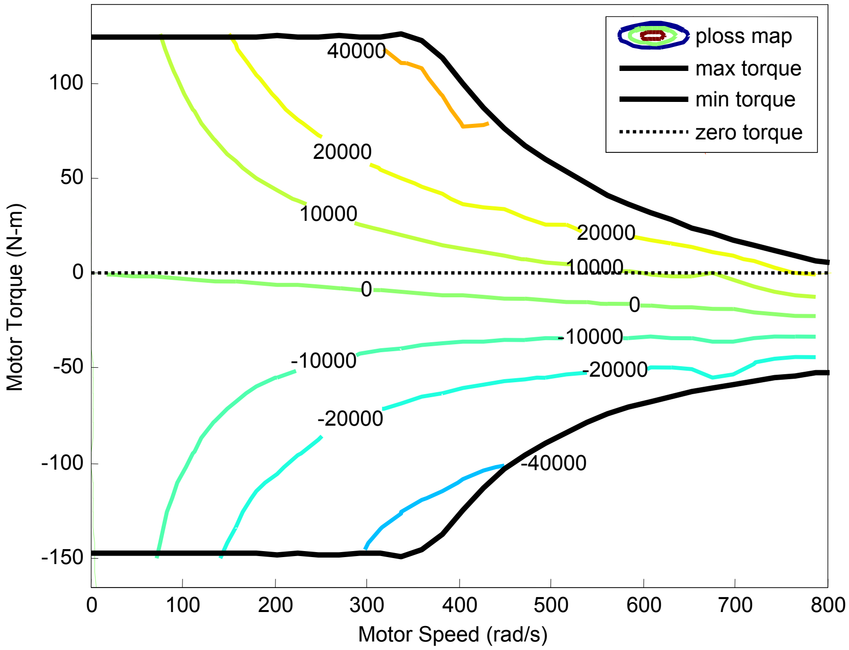

Figure 5.1 Optimal Motor Map, RMSE Consistency

5.2.2 AVASIM Consistency Measure in ATC

Similarly, the ATC optimization results using AVASIM as a consistency measure for the functional data are shown in Tables 5.4-5.6. As indicated earlier, the coordination strategy was repeated until the number of ATC iterations was identical to that of the RMSE case. The runtime for this case was 9.36 hours and also resulted in a system solution that was reasonably consistent between both subproblems. This time, the active constraints included the upper bound on $\omega_{max}{}^{T}$ and the vehicle range constraint $g_{11,6}$ in the P_{11} subproblem, which were limited to $\omega_{max}{}^{T}$ = 755 rad/s and R_{min} = 100 miles, respectively. The optimal motor map computed by the POD coefficients is shown in Figure 5.2. Finally, the total mass of the vehicle was 1078 kg, with approximately 11.6% (125 kg) of the mass associated with the battery. With such a design, the EV is predicted to have a gasoline-equivalent fuel economy of mpg_e = 190 mpg and a 0-60 mph acceleration time of t_{60} = 9.29 s.

Table 5.4 Optimal Decision Vector for P_{11} Subproblem, AVASIM Consistency

B_I	B_W	B_L	x_{batt}	p_r	$\omega_{max}{}^{T}$	$m_m{}^{T}$	$J_r{}^{T}$	$I_{ym}{}^{T}$	$I_{zm}{}^{T}$	$y_m{}^{T}$
0.74	1.03	19.75	0.25	3.13	755	40.39	0.28	1.12	1.20	0.39

Table 5.5 Optimal Decision Vector for P_{22} Subproblem, AVASIM Consistency

ζ_s	r_m	n_c	R_r
0.105	0.119	17.59	0.054

Table 5.6 Optimal Consistency Constraint Vector/Weights, AVASIM Consistency

Consistency Constraint	c_{opt}	v_{opt}	w_{opt}
$c_{z,max}$	0.66	9.25×10^{8}	6.80×10^{4}
$c_{z,min}$	0.56	7.90×10^{8}	6.80×10^{4}
$c_{z,pLoss}$	0.49	6.89×10^{9}	6.80×10^{4}
$c_{\omega max}$	0	0	6.80×10^{4}
c_{mm}	-0.69	-9.70×10^{8}	6.80×10^{4}
c_{Jr}	0.02	2.43×10^{7}	6.80×10^{4}
c_{Iym}	0.07	9.72×10^{7}	6.80×10^{4}
c_{Izm}	-0.04	-6.11×10^{7}	6.80×10^{4}
c_{ym}	0.01	1.38×10^{7}	6.80×10^{4}

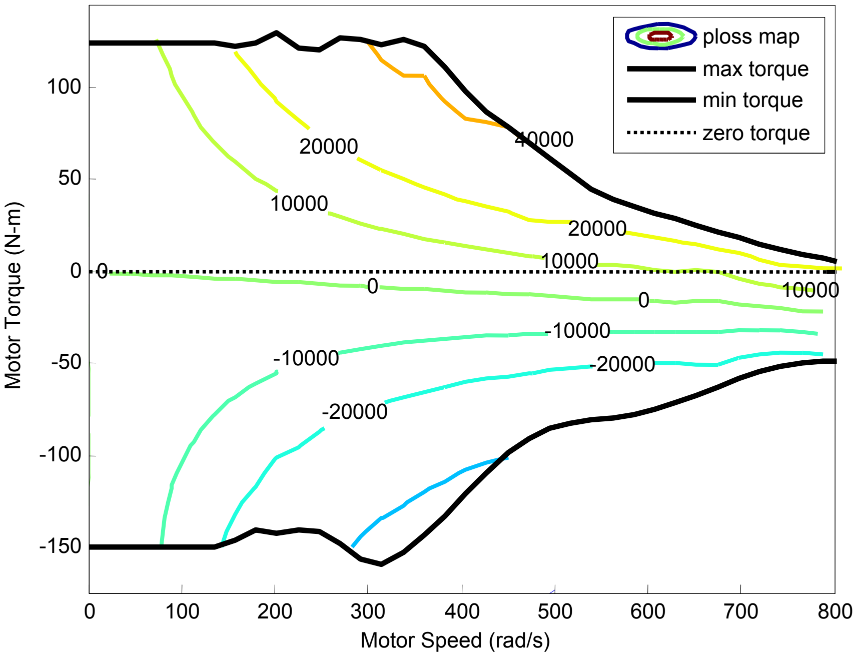

Figure 5.2 Optimal Motor Map, AVASIM Consistency

5.2.3 Generalized AVASIM Consistency Measure in ATC

Finally, the ATC optimization results using generalized AVASIM as a consistency measure for the functional data are shown in Tables 5.7-5.9. Because the results from using the AVASIM consistency measure appeared to indicate that the global accuracy of the functional data was more important, the weights for generalized AVASIM were set to w_{local} = 1/3 and w_{global} = 2/3, respectively. The runtime for this case was approximately 8.61 hours and resulted in a system solution that was reasonably consistent between both subproblems. Like the RMSE case, the only active constraints were the upper bound on ω_{max}^T, the performance constraint $g_{11,3}$, and the battery capacity constraint $g_{11,8}$ in the P_{11} subproblem; these were limited to ω_{max}^T = 755 rad/s, t_{60max} = 10 s, and C_{bmax} = 200 Ah, respectively. The optimal motor map produced by the POD coefficients is illustrated in Figure 5.3. Additionally, the total mass of the vehicle was 1111 kg, with approximately 14.3% (158 kg) of the mass associated with the battery. With such a design, the EV could achieve a gasoline-equivalent fuel economy of mpg_e = 185 mpg and a range of R = 135 miles.

Table 5.7 Optimal Decision Vector for P_{11} Subproblem, G-AVASIM Consistency

B_I	B_W	B_L	x_{batt}	p_r	ω_{max}^T	m_m^T	J_r^T	I_{ym}^T	I_{zm}^T	y_m^T
0.74	1.03	19.75	0.15	3.13	755	40.39	0.28	1.12	1.20	0.39

Table 5.8 Optimal Decision Vector for P_{22} Subproblem, G-AVASIM Consistency

l_s	r_m	n_c	R_r
0.0978	0.123	17.77	0.055

Table 5.9 Optimal Consistency Constraint Vector/Weights, G-AVASIM Consistency

Consistency Constraint	c_{opt}	v_{opt}	w_{opt}
$c_{z,max}$	0.16	2.36×10^8	6.80×10^4
$c_{z,min}$	0.16	2.28×10^8	6.80×10^4
$c_{z,pLoss}$	0.62	6.70×10^8	6.80×10^4
$c_{\omega max}$	0	0	6.80×10^4
c_{mm}	0	8.42×10^6	6.80×10^4
c_{Jr}	0.01	8.73×10^6	6.80×10^4
c_{Iym}	0.02	3.49×10^7	6.80×10^4
c_{Izm}	0	-2.58×10^6	6.80×10^4
c_{ym}	0	3.04×10^6	6.80×10^4

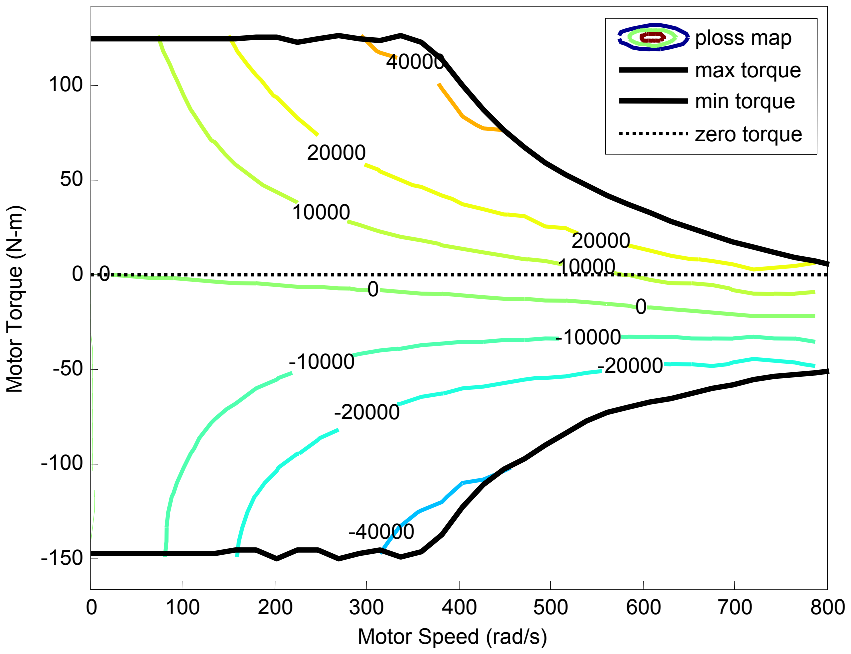

Figure 5.3 Optimal Motor Map, G-AVASIM Consistency

5.2.4 Summary of ATC Results

Using the same definitions for $\mathbf{x}_*^{AiO}$ and $\mathbf{x}_*^{ATC}$ that were presented in Chapter 4, it is seen that the errors between the AiO and ATC design solutions are $\frac{\left\|\mathbf{x}_*^{AiO}-\mathbf{x}_*^{ATC}\right\|_2}{\left\|\mathbf{x}_*^{AiO}\right\|_2}=0.113$, $\frac{\left\|\mathbf{x}_*^{AiO}-\mathbf{x}_*^{ATC}\right\|_2}{\left\|\mathbf{x}_*^{AiO}\right\|_2}=0.113$, and $\frac{\left\|\mathbf{x}_*^{AiO}-\mathbf{x}_*^{ATC}\right\|_2}{\left\|\mathbf{x}_*^{AiO}\right\|_2}=0.108$ for the RMSE, AVASIM, and generalized AVASIM consistency measures, respectively. Hence, the results clearly show that implementing the generalized AVASIM consistency measure provides the most accurate design solution in this work. The most reasonable explanation for this outcome is that the emphasis on global functional data accuracy within generalized AVASIM improved the functional data consistency between the ATC subproblems, which in turn reduced the inconsistencies of the remaining scalar-valued coupling variables and improved the accuracy of the design solution. Conversely, RMSE only addresses local functional data accuracy, which limits its ability to capture the global characteristics of functional data unless the number of discretized points is extremely large. Such a limitation may have ultimately reduced the functional data consistency between the ATC subproblems, which in turn would have reduced the consistencies of the remaining scalar-valued coupling variables and limited the accuracy of the design solution. The fact that implementing the AVASIM consistency measure did not yield an improvement over the RMSE consistency measure is surprising since it addresses both local and global functional data accuracy; however, it is posited that this may have been due to the instability of the E_{local} measure within AVASIM, which can be filtered out with generalized AVASIM by allocating more weight to global functional data accuracy.

Note that the consistency values of the scalar-valued coupling variables are affected by this new consistency measure since all of the coupling variables are related through at least a subset of the local design variables (ℓ_s, r_m, n_c, R_r) in the P_{22} subproblem. The relationship between improved consistency and improved design solution accuracy can be seen by calculating $\left\|\mathbf{c}_{opt}\right\|_2$ for each solution, which is 1.06, 1.21, and 0.66 for the RMSE, AVASIM, and generalized AVASIM consistency measures, respectively. Observe that this vector norm is only used for comparison purposes as it is not physically meaningful on an independent basis. Since the trend in $\left\|\mathbf{c}_{opt}\right\|_2$ nearly follows that of $\frac{\left\|\mathbf{x}_*^{AiO}-\mathbf{x}_*^{ATC}\right\|_2}{\left\|\mathbf{x}_*^{AiO}\right\|_2}$, the explanation provided for the improvement in design solution accuracy is adequately supported.

In addition, an interesting trend that is seen in this study is that the use of the AVASIM and generalized AVASIM consistency measures improved the efficiency of ATC. Indeed, the runtimes while using the RMSE, AVASIM, and generalized AVASIM consistency measures were 10.72 hours, 9.36 hours, and 8.61 hours, respectively. This result was somewhat unexpected given the fact that the computational effort required by the AVASIM and generalized AVASIM consistency measures was greater than that of the RMSE consistency measure. Since all aspects of the design problem, including the number of ATC iterations, was identical for each case, the only reasonable explanation for the reduced runtimes is that fewer function evaluations were required for each of the subproblems per ATC iteration. In turn, the reduced number of function evaluations was likely due to the greater overall stability of the AVASIM and generalized AVASIM consistency measures. Recall that the RMSE consistency measure only addresses local functional data accuracy, which in general may fluctuate much than global functional data accuracy over the course of design optimization. The AVASIM and generalized AVASIM consistency measures both address global functional data accuracy, with the latter measure having the most flexibility to emphasize global functional data accuracy. Because this functional data accuracy component is more likely to be stable during design optimization, it is believed that this led to fewer function evaluations and thus contributed to faster runtimes.

5.3 Conclusions

It is evident based on the results that the generalized AVASIM consistency measure (with an emphasis on global accuracy) is the best choice for this work as it predicted the most accurate design solution in the least amount of time. This is true for most ATC problems since the global measure is usually more important and stable than the local measure within generalized AVASIM and will generally provide more accurate designs solutions using fewer function evaluations. Moreover, unlike RMSE, generalized AVASIM (as well as AVASIM) can provide meaningful information regarding the consistency of functional data in a decomposition-based optimization strategy. For example, in Table 5.9, the generalized AVASIM consistency measure indicates that the consistencies of the maximum/minimum motor torque curves and the power loss map exchanged between the subproblems are (1 – 0.16) x 100% = 84%, (1 – 0.16) x 100% = 84%, and (1 – 0.62) x 100% = 38%, respectively. The values associated with the RMSE consistency measure in Table 5.3 for the same functional data are incapable of providing such information. However, despite the success of the generalized AVASIM consistency measure for this design problem, a couple of items should be investigated in future work. First, it should be determined if a systematic approach can be developed to assign values to w_{local} and w_{global}. This clearly had a significant impact on both the accuracy and efficiency of the ATC solution, and it is unknown whether a different weighting could further improve the optimization strategy. While it was sufficient in this study to rely on extensive experience with the model and design problem to set values for these weights, such an approach may not be appropriate or efficient in more general problem applications. Second, other error metrics should continue to be explored in terms of their ability to support decomposition-based optimization strategies through the accuracy assessment of 1D and higher dimensional functional data. Such exploration may reveal other competitive alternatives and could help to specify the conditions under which generalized AVASIM is a suitable consistency measure more precisely. Nevertheless, the present study is the first formal attempt to explore the capability of any functional data error metric as a consistency measure within a decomposition-based optimization strategy [*Alexander and Papalambros* (2010)] and provides compelling evidence for the superiority of generalized AVASIM.

5.4 Summary

This chapter explored the use of three different error metrics as consistency measures for coupled, functional data in an ATC problem formulation. After applying RMSE, AVASIM, and generalized AVASIM as consistency measures in the ATC optimization of a commercial EV powertrain, it was found that the generalized AVASIM consistency measure (with an emphasis on global accuracy) was superior as it provided the most accurate design solution in the least amount of time. Furthermore, it was stated that this would be the most appropriate consistency measure in the majority of ATC design problems since the global measure is usually more important and stable than the local measure within generalized AVASIM and would provide more accurate design solutions using fewer function evaluations. Moreover, unlike RMSE, generalized AVASIM (as well as AVASIM) can provide clear definitions of functional data consistency among ATC subproblems. Nevertheless, since this study is the first of its kind, more work must be completed regarding the weighting strategy of generalized AVASIM as well as the investigation of competitive alternatives before more specific conditions can be cited for its general application. The next chapter will investigate the final research question of this dissertation, which deals with the effective constraint management of reduced representation variables within an ATC framework.

Chapter 6

Constraint Management of Reduced Representation Variables

As mentioned in Chapter 1, the approximations of the motor performance curves via POD are valid only within the sampling domain of the original representations. This is true not only for POD, but for the majority of similar applications; that is, data approximation models are usually effective for interpolation, but rarely, if ever, for extrapolation. In the context of design optimization, one can ensure that such data extrapolation, and hence ill-behaved analysis and optimization, does not occur by introducing appropriate constraints on the approximation models. In some cases, simply identifying the maximum and minimum attainable values for the parameters within these models is sufficient; however, in general, one cannot assume that the parameter space is a hypercube constrained by simple upper and lower bounds. Rather, the parameter space can, in many cases, be highly-nonlinear, resulting in a generalized volume in hyperspace. The fact that these parameters often lack physical meaning further complicates this situation, since it is often impossible to practically construct constraints that define the validity domain of high-dimensional, non-convex, abstract quantities [*Alexander et al.* (2010b)]. This is evident in the ATC problem formulation for the commercial EV powertrain, where the parameters are POD coefficients serving as reduced representation variables.

Recall that in recent work, a penalty-value based heuristic was implemented as a temporary solution to this problem and led to reasonable results. However, it also produced an ill-conditioned ATC problem which led to many ATC iterations and extensive runtimes. Although more direct approaches such as probability density-based models [*Tarassenko et al.* (1995)] and convex hulling algorithms [*Barber et al.* (1996)]

were considered, each of these methods had significant shortcomings that made them unsuitable as strong, alternative solutions. Nevertheless, a technique known as support vector domain description (SVDD) [*Tax and Duin* (1999a); *Tax and Duin* (1999b)] did emerge from the literature as a viable candidate and was initially explored as part of this dissertation work. This chapter completes this work by comparing the penalty value-based heuristic to an alternative that uses SVDD as a potential constraint management method for the model validity region of the reduced representation variables.

6.1 Penalty Value-Based Heuristic

The penalty value-based heuristic constrains the model validity region indirectly by assigning large penalty values to objective function and constraint function outputs that depend on reduced representation variables outside the parameter space. It is expected that this would force the optimizer to select reduced representation variables that lie within the parameter space or model validity region. A key assumption for the successful implementation of this method is that a non-gradient-based optimizer will be used instead of a gradient-based optimizer [*Alexander et al.* (2010b)]. This is because penalizing outputs such as the objective function with large values in gradient-based optimizers can result in ill-conditioned optimization problems due to large gradients.

One way the penalty value-based heuristic can be executed is through a conditional statement that attempts to compute all quantities that depend on the reduced representation variables and, if unable to perform the computation, returns penalty values for the appropriate quantities and continues solving the optimization problem. When programming in MATLAB®, a reasonable approach would be to use a "try-catch" statement [*MATLAB® Function Reference*]. In this technique, MATLAB® attempts to execute the code between the keywords "try" and "catch", and in most cases will return the results between these keywords. However, if the code between "try" and "catch" fails and produces an error, then MATLAB® can execute an alternative code between the keywords "catch" and "end". Therefore, in the context of the penalty value-based heuristic, an attempt can be made to compute all quantities that depend on the reduced representation variables between "try" and "catch" and, if the computations cannot be performed, penalty values can be assigned to the appropriate quantities between “catch” and “end”. Figure 6.1 shows an excerpt from the MATLAB® code for the commercial EV powertrain model in which an attempt can be made to perform the powertrain simulations and, upon failing, will return infinite values as appropriate for mpg_e, t_{60}, R, and P_V.

```
try
   % If simulation works, set error message to zero
   sim(‘pt’,[],options)
   pterr = 0;
   varargout{1} = pterr;
catch
   % Set simulation outputs to penalty values
   mpge = -inf;
   t60 = inf;
   R = -inf;
   PV = inf;
   return
end
```

Figure 6.1 Penalty Value-Based Heuristic: MATLAB® Try-Catch Statement

6.2 Support Vector Domain Description

SVDD [*Tax and Duin* (1999a); *Tax and Duin* (1999b); *Malak and Paredis* (2009)] is a classification method that uses a machine learning algorithm to approximate the boundary of a set of data points and to identify whether new data points lie inside the boundary description. In particular, SVDD can be used to represent data set boundaries that are nonlinear, non-convex, and even disconnected without adding much complexity or computational burden. It is also distinct from other machine learning algorithms in that it requires only one class of data for classification since it aims to identify the minimum radius hypersphere enclosing the data. This feature is advantageous for classification problems in which a second class of data is either unknown or difficult to generate, as is the case for the reduced representation variables.

In the context of constraint management for the reduced representation variables in optimization, SVDD can be used to augment the penalty value-based heuristic through the inclusion of explicit constraints representing the boundary of the model validity region. Note that the penalty value-based heuristic is still necessary as the majority of optimizers enable the selection of decision vectors that may periodically violate constraints during optimization; in the case of the current problem, this can lead to failure of the underlying analysis models. However, it is expected that the boundary definitions (and hence constraints) generated by SVDD would directly minimize the possibility of analysis model failure since all feasible decision vectors would have to satisfy these constraints.

6.2.1 Theory

Because it is assumed that the data space can be effectively characterized by a hypersphere, the objective is to solve the following primal optimization problem [*Tax and Duin* (1999a); *Tax and Duin* (1999b); *Malak* (2008); *Malak and Paredis* (2009)]:

$$\begin{aligned}&\min_{R_{hyp},\mathbf{a},\xi_i} R_{hyp}^2 + C_p \sum_i \xi_i \\ &\textit{subject to } \left\|\mathbf{z}_{r,i} - \mathbf{a}\right\|_2^2 \le R_{hyp}^2 + \xi_i, \quad i = 1 \cdots m\end{aligned} \tag{6.1}$$

Here, R_{hyp} denotes the hypersphere radius, ξ denotes a hypersphere radius slack variable, C_p denotes the slack variable penalty constant, $\mathbf{z}_r$ denotes a data sample (which is a p-dimensional vector of reduced representation variables in this application), $\mathbf{a}$ denotes the hypersphere center, and m denotes the number of samples. The second term in the objective function of Equation (6.1) relaxes the optimization problem and permits the inclusion of outliers. In practice, this optimization problem is never solved for reasons given in [*Vapnik* (1995)]; instead, its dual is formulated by constructing the Lagrangian

$$L(R_{hyp}, \mathbf{a}, B_i, \xi_i, \mu_i) = R_{hyp}^2 + C_p \sum_i \xi_i - \sum_i B_i \left(R_{hyp}^2 + \xi_i - \left\|\mathbf{z}_{r,i} - \mathbf{a}\right\|_2^2 \right) - \sum_i \mu_i \xi_i \tag{6.2}$$

with nonnegative Lagrange multipliers B_i and μ_i. Applying Karush-Kuhn-Tucker (KKT) conditions to Equation (6.2) yields the following constraints [*Malak* (2008)]:

$$\sum_i B_i = 1 \tag{6.3}$$

$$\mathbf{a} = \frac{\sum_i B_i \mathbf{z}_{r,i}}{\sum_i B_i} = \sum_i B_i \mathbf{z}_{r,i} \tag{6.4}$$

$$C_p - B_i - \mu_i = 0, \quad i = 1 \cdots m \tag{6.5}$$

The new Wolfe dual optimization problem is then stated as [*Malak* (2008)]

$$\begin{aligned} &\max_{B_i} \sum_i B_i (\mathbf{z}_{r,i}^T \mathbf{z}_{r,i}) - \sum_i \sum_j B_i B_j (\mathbf{z}_{r,i}^T \mathbf{z}_{r,j}) \\ &\mathit{subject\,to} \quad 0 \le B_i \le C_p, \quad i = 1 \cdots m \\ &\qquad \sum_i B_i = 1 \end{aligned} \tag{6.6}$$

where each μ_i is eliminated through the bound constraints on each B_i. The dual solutions are categorized according to three conditions: $B_i = 0$, $0 < B_i < C_p$, and $B_i = C_p$. The first condition ($B_i = 0$) is satisfied by the majority of the dual variables for large m [*Malak* (2008)] and implies that the associated data sample $\mathbf{z}_{r,i}$ lies within the hypersphere. The second condition ($0 < B_i < C_p$) implies that the associated data sample $\mathbf{z}_{r,i}$ lies at the boundary of hypersphere and is essential to its description; these samples are termed support vectors [*Tax and Duin* (1999a); *Tax and Duin* (1999b); *Malak* (2008); *Malak and Paredis* (2009)]. The third condition ($B_i = C_p$) implies that the associated data sample $\mathbf{z}_{r,i}$ lies outside the hypersphere and is an outlier.

Using the dual variables and Equation (6.4), the squared distance R^2_{dist} from **a** to any arbitrary data point **y** is calculated as

$$R^2_{dist}(\mathbf{y}) = \|\mathbf{y} - \mathbf{a}\|_2^2 = \mathbf{y}^T \mathbf{y} - 2\sum_i B_i (\mathbf{y}^T \mathbf{z}_{r,i}) + \sum_i \sum_j B_i B_j (\mathbf{z}_{r,i}^T \mathbf{z}_{r,j}) \tag{6.7}$$

where the indices i and j run over the support vectors and their associated Lagrange multipliers. With this definition, R_{hyp} can be calculated by setting $\mathbf{y} = \mathbf{z}_{r,i}$ for any data sample that is a support vector, and in turn this information can be used to determine whether an arbitrary data point lies inside the boundary description:

$$R_{dist}^{2}(\mathbf{y}) \leq R_{hyp}^{2} \tag{6.8}$$

Such a condition can be added to the ATC problem formulation for the commercial EV powertrain to constrain the POD model directly.

A key limitation in the nominal SVDD problem formulation is that it assumes a hyperspherical data space. Since this is rarely the case, one must usually map the data into some higher-dimensional "feature space" through a nonlinear transformation where the hyperspherical domain assumption is more appropriate [*Malak* (2008)]. Because these nonlinear transformations can be difficult to develop explicitly, Mercer kernel functions [*Scholkopf and Smola* (2002)] are used to represent the dot product between any two nonlinear transformations. Although several kernel functions exist, the most preferred in the literature is the Gaussian kernel function

$$K_G(\mathbf{z}_{r,i}, \mathbf{z}_{r,j}) = e^{-q_0 \left\| \mathbf{z}_{r,i} - \mathbf{z}_{r,j} \right\|_2^2} \tag{6.9}$$

where q_0 is the kernel width parameter. Equation (6.9) can then be substituted for the dot product terms in Equations (6.6)-(6.7), yielding the following dual optimization problem and squared distance formulations:

$$\begin{aligned} &\max_{B_i} \sum_i B_i K_G(\mathbf{z}_{r,i}, \mathbf{z}_{r,i}) - \sum_i \sum_j B_i B_j K_G(\mathbf{z}_{r,i}, \mathbf{z}_{r,j}) \\ &\textit{subject to} \quad 0 \leq B_i \leq C_p, \quad i = 1 \cdots m \\ &\qquad\qquad \sum_i B_i = 1 \end{aligned} \tag{6.10}$$

$$R_{dist}^{2}(\mathbf{y}) = K_G(\mathbf{y},\mathbf{y}) - 2\sum_i B_i K_G(\mathbf{y},\mathbf{z}_{r,i}) + \sum_i \sum_j B_i B_j K_G(\mathbf{z}_{r,i},\mathbf{z}_{r,j}) \tag{6.11}$$

The parameters q_0 and C_p in Equations (6.10)-(6.11) must be tuned to construct an appropriate SVDD. In practice, however, modifications to C_p have a minimal impact on the solution [*Tax and Duin* (1999b); *Malak* (2008)], leaving only q_0 to be tuned. This parameter is adjusted such that overfitting of the data is minimized. Here, overfitting is defined as the rejection of an arbitrary data point y that is in fact within the data sample domain. Although overfitting can be monitored visually [*Malak* (2008)] by examining contour plots, this is normally insufficient for most applications and impossible for high-dimensional ($p > 3$) data sets. A more formal approach that makes use of the leave-one-out method [*Vapnik* (1995)] is usually more appropriate. This method essentially states that the probability of overfitting, which is also known as the error of the first kind [*Tax and Duin* (1999a); *Tax and Duin* (1999b)], can be estimated by determining the proportion of data samples that are support vectors [*Tax and Duin* (1999a); *Tax and Duin* (1999b)]:

$$E[P(error)] = \frac{n_{SV}}{m} \tag{6.12}$$

Note that in the above, n_{SV} refers to the number of support vectors. Hence, q_0 can be determined by setting an acceptable target for overfitting P_{target} and minimizing the ℓ_2-norm on the difference between this target and the estimated performance of the SVDD:

$$\begin{aligned} &\min_{q_0} \left\| \frac{n_{SV}}{m} - P_{target} \right\|_2^2 \\ &\textit{subject to} \quad -q_0 < 0 \end{aligned} \tag{6.13}$$

The optimal SVDD therefore requires the solution of Equation (6.13), which in turn requires the solution of Equation (6.10) to determine n_{SV} for a given q_0. Observe that underfitting, or error of the second kind, cannot be addressed for SVDD as this requires data samples outside the target domain and hence directly violates the assumption of a single data class for SVDD.

6.2.2 Application

Three SVDD models were developed to approximate the boundaries of the POD model validity regions associated with the maximum and minimum motor torque curves and power loss map in the ATC problem formulation for the commercial EV powertrain model. This first required the generation of data sample vectors, which were identical to those used for the POD representations but mapped appropriately into POD-space:

$$\mathbf{Z}_{r,max} = \mathbf{\Phi}^T_{p,max}(\mathbf{Z}_{max} - \overline{\mathbf{Z}}_{max}) \tag{6.14}$$

$$\mathbf{Z}_{r,min} = \mathbf{\Phi}^T_{p,min}(\mathbf{Z}_{min} - \overline{\mathbf{Z}}_{min}) \tag{6.15}$$

$$\mathbf{Z}_{r,pLoss} = \mathbf{\Phi}^T_{p,pLoss}(\mathbf{Z}_{pLoss} - \overline{\mathbf{Z}}_{pLoss}) \tag{6.16}$$

The data sample vectors in $\mathbf{Z}_{r,max}$, $\mathbf{Z}_{r,min}$, and $\mathbf{Z}_{r,pLoss}$ were then normalized through the MATLAB® function *mapminmax* [*MATLAB® Function Reference*] prior to constructing the models. Such data sample preprocessing is typical of most machine learning algorithms as this helps to improve the performance of their associated models. From here, the slack variable penalty constants were set to $C_p = 0.5$, the overfitting targets were set to $P_{target} = 0.10$, and the kernel width parameter bounds were set to $q_{0,min} = 10^{-6}$ and $q_{0,max} = 10$ based on experience for each SVDD problem formulation. Note that such bounds for q_0 were necessary to satisfy the problem structure required by the optimizer. In an effort to obtain the global optimum for the tuning problem in Equation (6.13), the non-gradient-based optimizer NOMADm was selected again. However, because of the convexity of the SVDD optimization problem in Equation (6.10), the MATLAB® gradient-based optimizer *fmincon* [*MATLAB® Function Reference*] was selected. In both cases, the default settings were appropriate for the optimizers. Figures 6.2-6.4 illustrate portions of the optimal

SVDD boundaries for two dimensions of the POD model validity regions associated with the torque curves and power loss map.

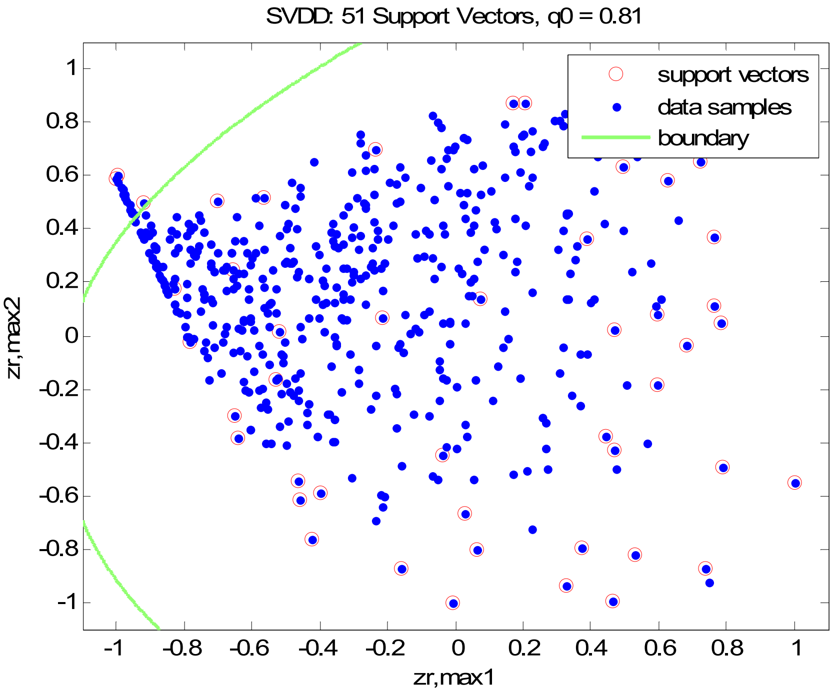

Figure 6.2 Partial SVDD Boundary, Max-Torque POD Model Validity Region

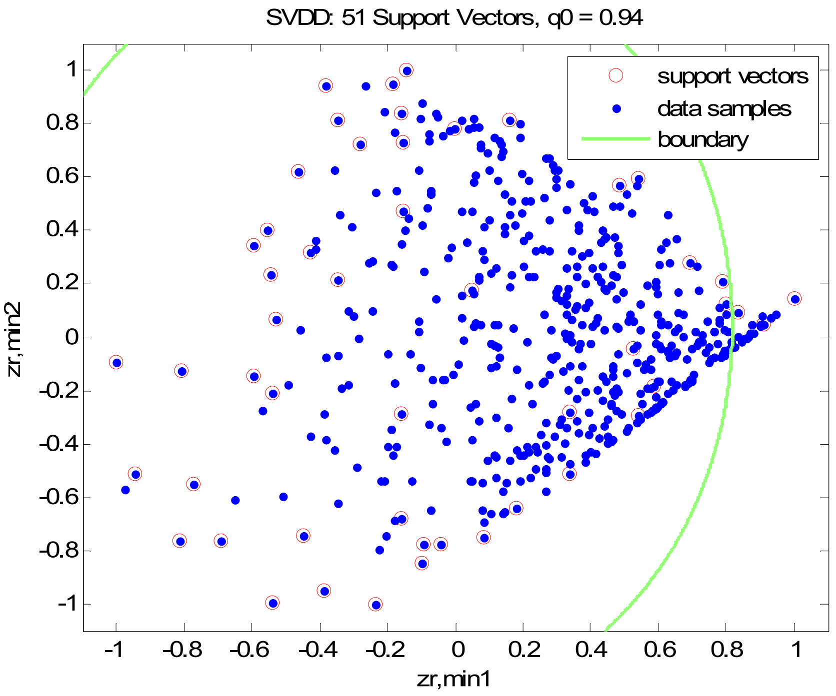

Figure 6.3 Partial SVDD Boundary, Min-Torque POD Model Validity Region

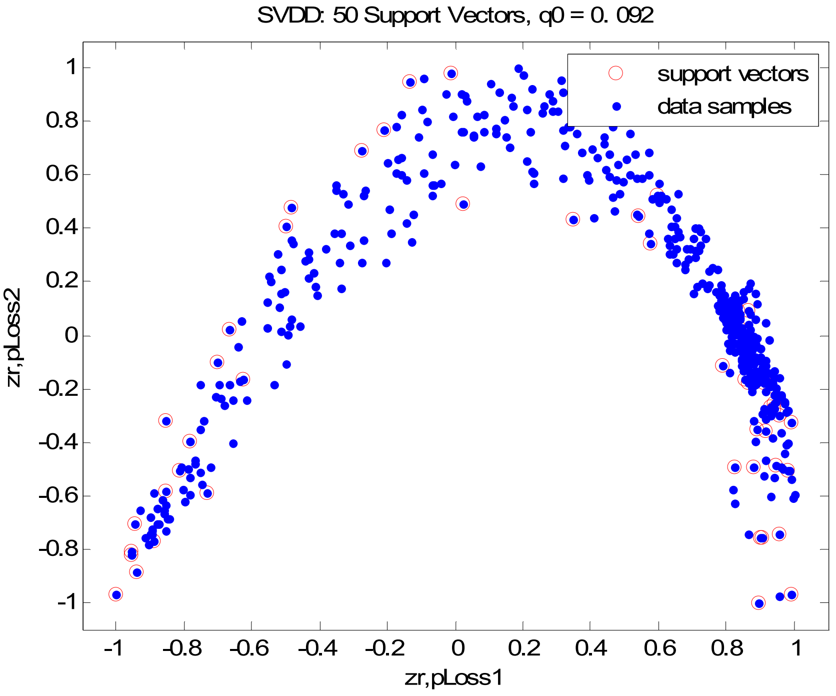

Figure 6.4 Partial SVDD Boundary, Power Loss POD Model Validity Region

6.3 ATC Problem Formulation and Solutions

Once again, the ATC problem formulation for the commercial EV powertrain model shown in Equations (4.8)-(4.9) provides the basis for the first part of this study, which implements the penalty value-based heuristic. The second part of this study, which implements both the penalty value-based heuristic as well as SVDD, augments the ATC problem formulation through the following constraints in the P_{11} subproblem:

$$g_{11,9} = R^2_{dist,max}(\bar{\mathbf{x}}_{11}) - R^2_{hyp,max} \leq 0 \tag{6.17}$$

$$g_{11,10} = R^2_{dist,min}(\bar{\mathbf{x}}_{11}) - R^2_{hyp,min} \leq 0 \tag{6.18}$$

$$g_{11,11} = R^2_{dist,pLoss}(\bar{\mathbf{x}}_{11}) - R^2_{hyp,pLoss} \leq 0 \tag{6.19}$$

Note that these constraints were derived by applying Equation (6.8). Additionally, the POD representations developed at CPV_{goal} = 99.99% were used to approximate the VVCVs associated with the motor torque curves and power loss map. In an effort to observe the accuracy and/or optimization efficiency contributions of the constraint management approaches exclusively, the "standard" RMSE consistency measure that was used in Chapter 4 is implemented here. The design problem for each constraint management method was solved using NOMADm. As in previous chapters, the default settings of this optimizer were modified for the P_{11} subproblem such that only a Latin hypercube search was performed and 1,000 function evaluations were permitted. This was necessary to alleviate computational issues associated with memory availability. However, for the P_{22} subproblem, the default settings were sufficient. Finally, in the ATC coordination strategy, the weight update parameter was set to $\beta = 2.75$, the initial weight vectors for both subproblems were set to $\mathbf{v} = \mathbf{0}$ and $\mathbf{w} = \mathbf{1}$, and the tolerance on $||\mathbf{c}^{(K)} - \mathbf{c}^{(K-1)}||_\infty$ for outer loop convergence was set to 10^{-2}. Like the other studies, all computational work was performed on a 3GHz, 4 MB RAM, Intel® Core™ 2 Duo CPU.

6.3.1 Constraint Management via Penalty Value-Based Heuristic

Tables 6.1-6.3 show the ATC optimization results when implementing the penalty value-based heuristic as a constraint management technique for the reduced representation variables. Once again, note that these results are identical to those in Chapter 4 for POD at CPV_{goal} = 99.99% but are repeated here to facilitate comparisons with the augmented constraint management technique (penalty value-based heuristic plus SVDD). Convergence was achieved after 12 ATC iterations with a runtime of approximately 10.72 hours and resulted in a system solution that was reasonably consistent between both subproblems. Recall that the only active constraints were the upper bound on ω_{max}^T, the performance constraint $g_{11,3}$, and the battery capacity constraint $g_{11,8}$ in the P_{11} subproblem; these were limited to ω_{max}^T = 755 rad/s, t_{60max} = 10 s, and C_{bmax} = 200 Ah, respectively. As usual, the optimal motor map computed by the POD coefficients is shown in Figure 6.5. Finally, the total mass of the vehicle was 1111 kg, with approximately 14.3% (158 kg) of the mass associated with the battery. These design conditions indicated that the EV could achieve a gasoline-equivalent fuel economy of mpg_e = 184 mpg and a range of R = 134 miles.

Table 6.1 Optimal Decision Vector for P_{11} Subproblem, PVBH

B_I	B_W	B_L	x_{batt}	p_r	ω_{max}^T	m_m^T	J_r^T	I_{ym}^T	I_{zm}^T	y_m^T
0.74	1.43	19.75	0.25	3.13	755	40.39	0.28	1.12	1.20	0.39

Table 6.2 Optimal Decision Vector for P_{22} Subproblem, PVBH

ζ_s	r_m	n_c	R_r
0.098	0.123	17.62	0.053

Table 6.3 Optimal Consistency Constraint Vector/Weights, PVBH

Consistency Constraint	c_{opt}	v_{opt}	w_{opt}
$c_{z,max}$	0.45	6.37×10^8	6.80×10^4
$c_{z,min}$	0.41	5.82×10^8	6.80×10^4
$c_{z,pLoss}$	0.73	1.01×10^9	6.80×10^4
$c_{\omega max}$	0	0	6.80×10^4
c_{mm}	-0.46	-6.53×10^8	6.80×10^4
c_{Jr}	0	1.51×10^6	6.80×10^4
c_{Iym}	0	5.93×10^6	6.80×10^4
c_{Izm}	-0.02	-3.21×10^7	6.80×10^4
c_{ym}	0	3.67×10^6	6.80×10^4

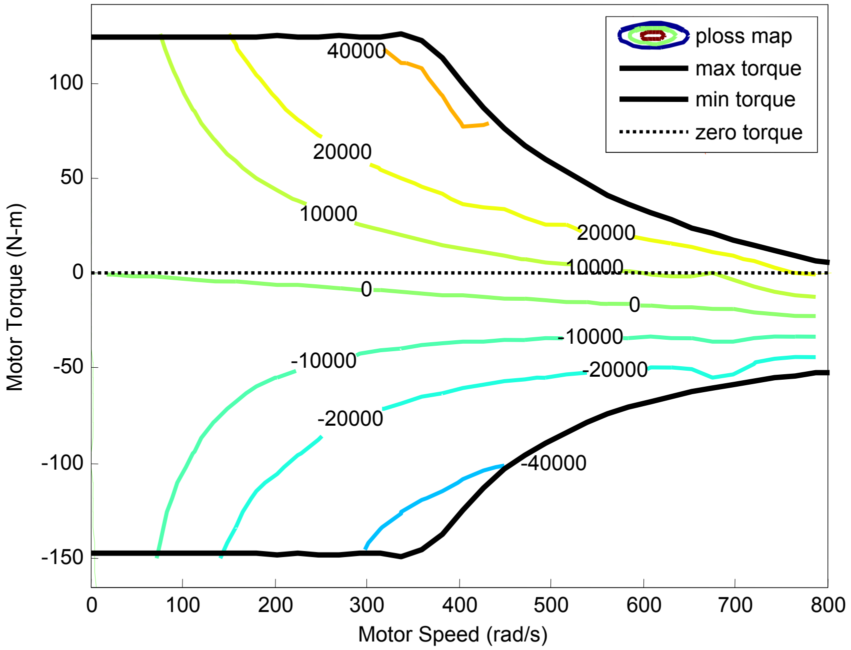

Figure 6.5 Optimal Motor Map, PVBH

6.3.2 Constraint Management via SVDD Augmentation

Similarly, Tables 6.4-6.6 show the ATC optimization results when augmenting the penalty value-based heuristic with SVDD as a constraint management technique for the reduced representation variables. The problem converged after 5 ATC iterations with a runtime of approximately 3.95 hours and resulted in a system solution that was reasonably consistent between both subproblems. The only meaningful active constraints included the upper bound on ω_{max}^T and the battery capacity constraint $g_{11,8}$ in the P_{11} subproblem, which were limited to ω_{max}^T = 755 rad/s and C_{bmax} = 200 Ah, respectively. Although the SVDD constraints $g_{11,9}$-$g_{11,11}$ were active as well, they were insignificant from a design perspective and only relevant mathematically. In particular, the activity of the SVDD constraints indicated that the optimal reduced representation variables were at the boundary of their respective POD model validity regions. The optimal motor map computed by the POD coefficients is shown in Figure 6.6. Finally, the total mass of the vehicle was 1111 kg, with approximately 14.3% (158 kg) of the mass associated with the battery. With such a design, the EV is predicted to have a gasoline-equivalent fuel economy of mpg_e = 149 mpg, a 0-60 mph acceleration time of t_{60} = 8.05 s, and a range of R = 109 miles.

Table 6.4 Optimal Decision Vector for P_{11} Subproblem, SVDD Augmentation

B_I	B_W	B_L	x_{batt}	p_r	ω_{max}^T	m_m^T	J_r^T	I_{ym}^T	I_{zm}^T	y_m^T
0.74	1.43	19.75	0.25	3.93	755	40.39	0.28	1.12	1.20	0.39

Table 6.5 Optimal Decision Vector for P_{22} Subproblem, SVDD Augmentation

ζ_s	r_m	n_c	R_r
0.096	0.124	17.87	0.065

Table 6.6 Optimal Consistency Constraint Vector/Weights, SVDD Augmentation

Consistency Constraint	c_{opt}	v_{opt}	w_{opt}
$c_{z,max}$	0.45	449	57.2
$c_{z,min}$	0.42	416	57.2
$c_{z,pLoss}$	0.29	297	57.2
$c_{\omega max}$	0	0	57.2
c_{mm}	0	-0.45	57.2
c_{Jr}	0	0.019	57.2
c_{Iym}	0	-0.031	57.2
c_{Izm}	0	0.035	57.2
c_{ym}	0	0.025	57.2

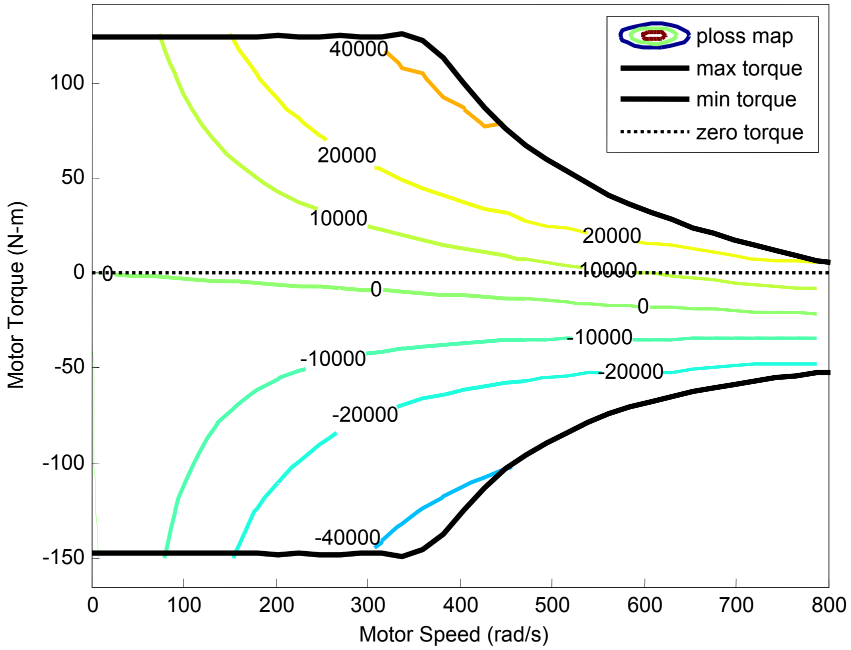

Figure 6.6 Optimal Motor Map, SVDD Augmentation

6.3.3 Summary of ATC Results

Using the same definitions for $\mathbf{x}_*^{AiO}$ and $\mathbf{x}_*^{ATC}$ that were presented in Chapter 4, it is seen that the errors between the AiO and ATC design solutions are $\frac{\left\|\mathbf{x}_*^{AiO}-\mathbf{x}_*^{ATC}\right\|_2}{\left\|\mathbf{x}_*^{AiO}\right\|_2}=0.113$ and $\frac{\left\|\mathbf{x}_*^{AiO}-\mathbf{x}_*^{ATC}\right\|_2}{\left\|\mathbf{x}_*^{AiO}\right\|_2}=0.110$ when implementing the penalty value-based heuristic and the SVDD augmentation as constraint management methods for the reduced representation variables, respectively. Hence, it is evident from the results that the constraint management of the reduced representation variables via the SVDD augmentation provides the most accurate design solution in this study. The most plausible explanation for this result is that the SVDD-related constraints forced the optimizer to perform more function evaluations in the feasible decision space, which included the POD model validity regions. Because this increased the set of feasible designs, the optimizer had a higher probability of identifying the optimal design solution instead of converging to any feasible (yet suboptimal) design. The penalty value-based heuristic, however, did not directly constrain the POD model validity regions and hence enabled the optimizer to perform function evaluations in a broader decision space which included many infeasible designs. Since this limited the set of feasible designs, the optimizer had a higher probability of converging to any feasible (yet suboptimal) design instead of identifying the optimal design solution. Of course, it is always possible that the SVDD augmentation could truncate a portion of the feasible decision space where the optimal solution exists and lead to an inferior result when compared to the penalty value-based heuristic; however, the probability of this event is ultimately related to the value prescribed for P_{target} in the SVDD models.

It is also evident from the results that the SVDD augmentation improves the efficiency of ATC compared to the penalty value-based heuristic. Indeed, the runtimes associated with the penalty value-based heuristic and the SVDD augmentation were 10.72 hours and 3.95 hours, respectively. The explanation for this outcome is directly related to the explanation for the improvement in the solution accuracy; that is, since the SVDD augmentation imposed explicit constraints on the POD model validity regions, the optimizer spent less time (i.e., fewer function evaluations) exploring designs outside the feasible decision space. Nevertheless, although the SVDD augmentation reduces the computational time during optimization, it still requires significant modeling time offline. Therefore, the SVDD augmentation is a more computationally efficient constraint management approach only if its total computational effort (modeling time plus runtime) is less than the runtime associated with the penalty value-based heuristic. The modeling times required to construct the optimal SVDDs for the POD model validity regions of the maximum and minimum motor torque curves and power loss map were 0.94 hours, 1.13 hours, and 0.27 hours, respectively. Because the total computational effort (6.29 hours) associated with the SVDD augmentation was less than the runtime associated with the penalty value-based heuristic, it is clear that the SVDD augmentation is a more computationally efficient constraint management approach.

6.4 Conclusions

Based on the results, it is evident that the best constraint management method for the reduced representation variables in this study is the SVDD augmentation. This approach produced the most accurate design solution with the least overall computational effort. While this conclusion holds for most optimization problems, including AiO problems, it may not be true for every case as the design solution accuracy could exhibit significant tradeoffs with the overfitting target P_{target} in the SVDD models. For example, as this parameter is increased, the probability of overfitting is also increased, and this may ultimately lead to the truncation of a region within the feasible decision space that contains the optimal design solution. Conversely, as this parameter is decreased, the probability of overfitting is decreased, but the optimizer may converge to any feasible (yet suboptimal) design due to the abundance of infeasible designs. Hence, there is a need to balance the limitation of SVDD (overfitting) with the limitation of the optimizer (convergence to any feasible design) when setting P_{target} in these studies. The exploration of this issue is proposed as a topic for future work.

6.5 Summary

This chapter investigated the use of appropriate constraint management methods for reduced representation variables in an ATC framework. Specifically, a penalty value-based heuristic was introduced and compared to an alternative method that augmented this heuristic with SVDD. The results from this study indicated that the SVDD augmentation was the best constraint management technique as it yielded the most accurate design solution with the least computational effort. Moreover, it was indicated that this would be the most promising constraint management method in the majority of optimization problems (both decomposition-based and AiO) since the SVDD-related constraints forced the optimizer to perform more function evaluations in the feasible decision space, thus leading to a higher probability of convergence to the optimal design solution with fewer overall function evaluations (and hence less runtime) instead of convergence to any feasible (yet suboptimal) solution. However, it was recognized that further exploration with respect to the performance target in SVDD and its impact on design solution accuracy would be necessary before completely assessing its suitability in broader problem applications. The next chapter will finally apply the knowledge gained from addressing the key dissertation research questions over the past three chapters to a military EV design optimization study.

Chapter 7

Military Electric Vehicle Design Optimization

The work throughout this dissertation thus far has addressed some of the challenges involved when using formal, decomposition-based optimization strategies to solve complex, simulation-based design problems in applications such as commercial EV powertrain design. In particular, when the problem decomposition yields decision variables that are coupled, functional data such as motor maps, it has been demonstrated that the implementation of appropriate reduced representations, consistency measures, and constraint management techniques for reduced representation variables are critical for the success of these optimization strategies.

Although success can be assessed in a variety of ways, the key measures that have been used in this dissertation are design solution accuracy and overall computational effort. These measures have suggested that the best design solutions will occur when using the most accurate POD reduced representations, implementing generalized AVASIM as a functional data consistency measure, and implementing a penalty value-based heuristic in conjunction with SVDD as a constraint management method for reduced representation variables. However, all of these findings have been based on a small, commercial vehicle application, and it would be both interesting and relevant to apply this knowledge to a larger scale design problem with slightly different decision criteria and requirements. This chapter, therefore, examines the aggregate contributions of the core research findings in the design optimization of a military EV in an ATC framework. Like the commercial EV application, an AiO optimization problem formulation and solution for the military EV powertrain model is introduced at the beginning of this chapter to facilitate comparisons among the design solutions.

7.1 AiO Problem Formulation and Solution

The AiO problem formulation uses the same analysis models as those described in Equations (3.1)-(3.3) and Equations (3.99)-(3.100) for the military EV with the exception that the electric traction motor analysis model $\mathbf{f}_{motor}$ is integrated as a sub-analysis model for the front and rear motors within the LTV-level analysis model $\mathbf{f}_{ltv}$. This was necessary because in the AiO problem, the motor designs are not considered separately; instead, all of the key design components of the EV powertrain—the battery, gearboxes, and motors—are considered simultaneously. Therefore, Equation (3.100) is modified as

$$\begin{aligned}[mpg_e, t_{50}, \tau_{V,f}, \tau_{V,r}, \omega_{V,f}, \omega_{V,r}, R, P_V, P_{V50}, C_b, d_s, P_{fail}] = \mathbf{f}_{ltv}(B_I, B_W, B_L, \cdots \\ m_{batt}, m_s, I_y, \ell_1, h, g_{b,f}, g_{b,r}, \ell_{s,f}, r_{m,f}, n_{c,f}, R_{r,f}, \cdots \\ \ell_{s,r}, r_{m,r}, n_{c,r}, R_{r,r})\end{aligned} \tag{7.1}$$

where the input variables to $\mathbf{f}_{motor}$ are now shared with $\mathbf{f}_{ltv}$. Figure 7.1 illustrates the relationships among the remaining analysis models that were described in Chapter 3 for the military EV powertrain, with the dashed box indicating that all analysis models are integrated into a single optimization problem formulation.

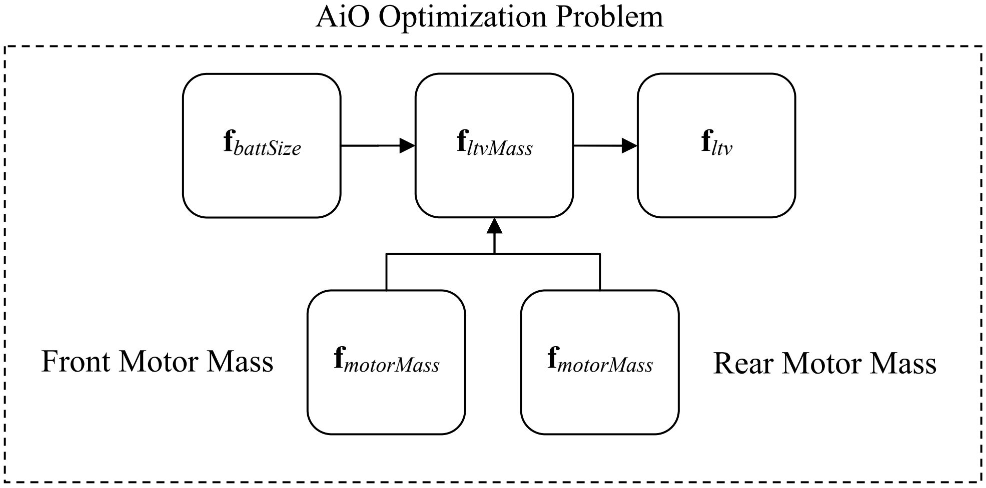

Figure 7.1 Analysis Model Relationships for Military EV AiO Problem

In military vehicle applications, a more meaningful design criterion is vehicle range as opposed to energy efficiency since it is critical for these vehicles to travel long distances in hostile environments without needing to refuel. Therefore, the objective of the AiO problem formulation is to maximize the vehicle range of the electric LTV while satisfying constraints related to battery packaging, performance, motor feasibility, power availability, battery capacity, mobility, and occupant safety:

$$
\begin{aligned}
&\min_{\mathbf{x}} \; -R(\mathbf{x}) \\
&\textit{subject to} \\
&\qquad \begin{aligned}
g_1 &= b_{w,V}(\mathbf{x}) \le 0 & g_7 &= \omega_{V,r}(\mathbf{x}) \le 0 \\
g_2 &= b_{\ell,V}(\mathbf{x}) \le 0 & g_8 &= P_V(\mathbf{x}) \le 0 \\
g_3 &= t_{50}(\mathbf{x}) - t_{50max} \le 0 & g_9 &= P_{V50}(\mathbf{x}) \le 0 \\
g_4 &= \tau_{V,f}(\mathbf{x}) \le 0 & g_{10} &= C_b(\mathbf{x}) - C_{bmax}(\mathbf{x}) \le 0 \\
g_5 &= \tau_{V,r}(\mathbf{x}) \le 0 & g_{11} &= -d_s(\mathbf{x}) \le 0 \\
g_6 &= \omega_{V,f}(\mathbf{x}) \le 0 & g_{12} &= P_{fail}(\mathbf{x}) - P_{failmax} \le 0
\end{aligned} \\
&\textit{where} \\
&\qquad \mathbf{x} = [B_I, B_W, B_L, x_{batt}, g_{b,f}, g_{b,r}, \ell_{s,f}, r_{m,f}, n_{c,f}, R_{r,f}, \ell_{s,r}, r_{m,r}, n_{c,r}, R_{r,r}]
\end{aligned}
\tag{7.2}
$$

In the above, g_1 and g_2 are battery packaging constraints, g_3 is a performance (0-50 mph acceleration time) constraint, g_4-g_7 are motor feasibility constraints, g_8-g_9 are power availability constraints, g_{10} is a battery capacity constraint, g_{11} is a mobility (vehicle directional stability) constraint, and g_{12} is an occupant safety (probability of exceeding underbody blast injury threshold) constraint. Note that appropriate bound constraints are included for the decision variables in **x**. As with the other case studies in this dissertation, the derivative-free optimization software package known as NOMADm [*Abramson* (2007)] was used to solve the problem. However, the settings for this optimizer were modified such that only a Latin hypercube search was performed. This was necessary to alleviate computational issues associated with an underlying kriging metamodel of the design problem that the optimizer constructs by default.

The results from the AiO problem formulation are shown in Table 7.1. It should be noted that the only active constraints in this problem were the motor torque feasibility constraints g_4-g_5, the performance-related power availability constraint g_9, and the battery capacity constraint g_{10}, which was limited to C_{bmax} = 500 Ah. The activity of the battery capacity constraint was expected given the objective of vehicle range for the electric LTV. Specifically, maximizing the range of the vehicle requires the battery to be as large as possible, which in this case is limited indirectly by cost. However, the activity of the motor torque feasibility constraints, which were both limited by the minimum torque curves, was not expected; it is believed that this behavior was caused by the aggressive braking within the convoy escort drive cycle. This in turn might have led to motor designs that possessed excessively high maximum torque curves which, when used in the forward-looking powertrain model, predicted an uncharacteristically fast 0-50 mph acceleration time (t_{50} = 5.56 s). Since this also places a significant power demand on the battery, it is believed that the aggressive 0-50 mph acceleration time led to the activity of the performance-related power availability constraint.

Finally, observe that the design solution suggests the use of 77 kW front motors (Figure 7.2) and 130 kW (Figure 7.3) rear motors to propel a 3116 kg vehicle, with approximately 8.5% (264 kg) of the mass associated with the battery. These design conditions indicate that the electric LTV could achieve a range of R = 79 miles while remaining directionally stable up to its maximum speed (70 mph) and limiting the probability of occupant injury to 12%.

Table 7.1 Optimal Decision Vector for Military EV AiO Problem

B_I	B_W	B_L	x_{batt}	$g_{b,f}$	$g_{b,r}$	$\ell_{s,f}$	$r_{m,f}$	$n_{c,f}$	$R_{r,f}$	$\ell_{s,r}$	$r_{m,r}$	$n_{c,r}$	$R_{r,r}$
1.22	2.01	21.00	0.05	0.86	1.13	0.122	0.118	19.30	0.275	0.07	0.131	13.90	0.075

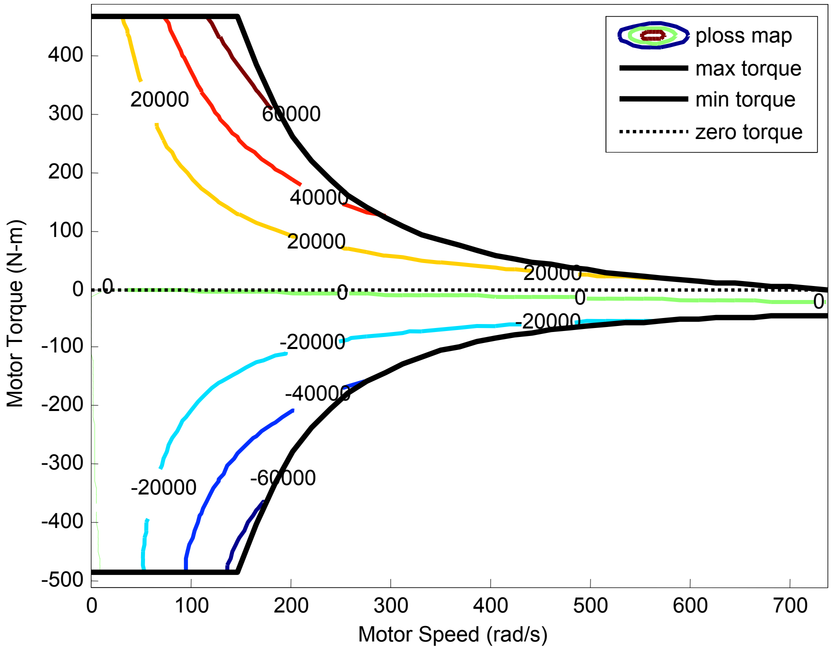

Figure 7.2 Optimal Front Motor Map, Military EV AiO Problem

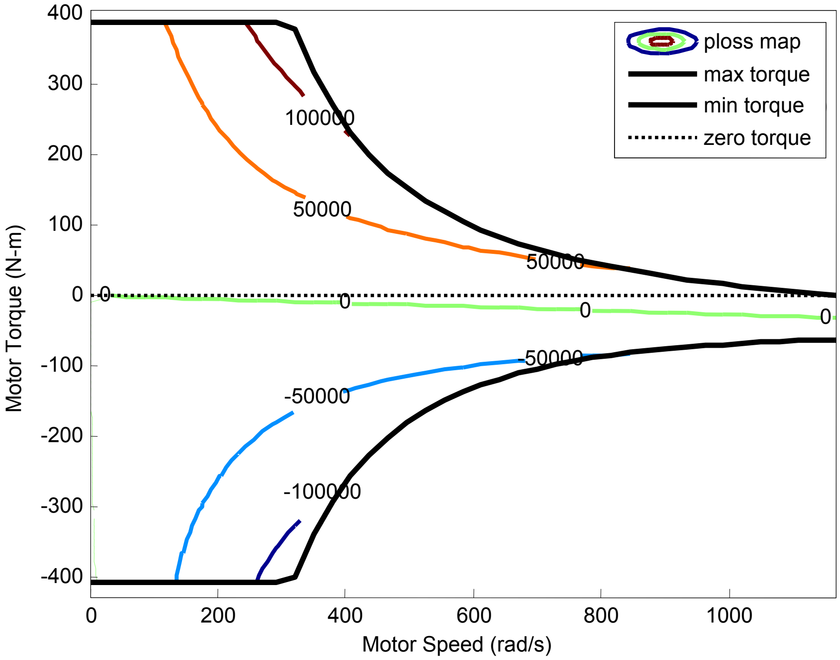

Figure 7.3 Optimal Rear Motor Map, Military EV AiO Problem

7.2 POD Representations and Accuracy Assessment

In preparation for the ATC problem formulation, POD representations were developed *a priori* at $CPV_{goal} = 99.99\%$ to approximate the VVCVs associated with the maximum and minimum torque curves and power loss map of the front and rear motors:

$$\mathbf{z}_{max,f} \approx \mathbf{\Phi}_{p,max,f}\mathbf{z}_{r,max,f} + \overline{\mathbf{z}}_{max,f} \tag{7.3}$$

$$\mathbf{z}_{min,f} \approx \mathbf{\Phi}_{p,min,f}\mathbf{z}_{r,min,f} + \overline{\mathbf{z}}_{min,f} \tag{7.4}$$

$$\mathbf{z}_{pLoss,f} \approx \mathbf{\Phi}_{p,pLoss,f}\mathbf{z}_{r,pLoss,f} + \overline{\mathbf{z}}_{pLoss,f} \tag{7.5}$$

$$\mathbf{z}_{max,r} \approx \mathbf{\Phi}_{p,max,r}\mathbf{z}_{r,max,r} + \overline{\mathbf{z}}_{max,r} \tag{7.6}$$

$$\mathbf{z}_{min,r} \approx \mathbf{\Phi}_{p,min,r}\mathbf{z}_{r,min,r} + \overline{\mathbf{z}}_{min,r} \tag{7.7}$$

$$\mathbf{z}_{pLoss,r} \approx \mathbf{\Phi}_{p,pLoss,r}\mathbf{z}_{r,pLoss,r} + \overline{\mathbf{z}}_{pLoss,r} \tag{7.8}$$

The functional data samples used to construct these reduced representations were generated separately for the front and rear motors through a LHS design of experiments consisting of $m = 750$ motor map samples each from $\mathbf{f}_{motor}$. During the sampling process, both functional data sample sets were interpolated onto prescribed, standard torque-speed meshes according to the same procedure described in Chapter 4. These meshes were defined as

$$\tau_i^{mesh,f} = -1600 + \left(\frac{3200}{n_{p,\tau,f} - 1}(i-1) \right), \quad i = 1 \cdots 81 \tag{7.9}$$

$$\omega_i^{mesh,f} = \frac{800}{n_{p,\omega,f} - 1}(i-1), \quad i = 1 \cdots 41 \tag{7.10}$$

and

$$\tau_i^{mesh,r} = -700 + \left(\frac{1400}{n_{p,\tau,r} - 1}(i-1) \right), \quad i = 1 \cdots 81 \tag{7.11}$$

$$\omega_i^{mesh,r} = \frac{1200}{n_{p,\omega,r} - 1}(i-1), \quad i = 1 \cdots 41 \tag{7.12}$$

for the front and rear motors respectively, where $n_{p,\tau,f} = n_{p,\tau,,r} = 81$ and $n_{p,\omega,f} = n_{p,\omega,,r} = 41$.

Based on the definitions of the standard meshes, the number of discretized points in $\mathbf{z}_{max}$, $\mathbf{z}_{min}$, and $\mathbf{z}_{pLoss}$ for the front and rear motor maps were $q_{max} = 41$, $q_{min} = 41$, and $q_{pLoss} = 3321$, respectively. Since $q_{max} = q_{min} << m$, the direct method outlined in Equations (2.6)-(2.9) was used to develop the POD representations for the maximum and minimum motor torque curves. Conversely, the method of snapshots described in Equations (2.10)-(2.12) was used to develop the POD representations for the motor power loss maps since $q_{pLoss} >> m$. Table 7.2 lists the number of POD coefficients (and hence reduced representation variables) required for both the front and rear motor maps. In each case, it is evident that the combined dimensionality Q of the VVCVs was dramatically reduced from $Q = q_{max} + q_{min} + q_{pLoss} = 3403$ to $Q = p_{max} + p_{min} + p_{pLoss} = 107$ and $Q = 97$, respectively. Finally, note that the computational effort required for the development of the POD representations for the front and rear motor maps (excluding motor map sample generation) was 1.53 s and 2.30 s.

Table 7.2 Number of POD Coefficients for Front/Rear Motor Maps

Motor Map	$\mathbf{z}_{r,max}$	$\mathbf{z}_{r,min}$	$\mathbf{z}_{r,pLoss}$
Front	12	12	83
Rear	11	11	75

The accuracy of the POD representations for the front and rear motors was quantified through AVASIM. In particular, both 1D and 2D formulations were applied as appropriate using a uniform tolerance of $tol_i = 0.10$ to assess the accuracy of the torque curves and power loss maps produced by the POD representations against the optimal torque curves and power loss maps produced by $\mathbf{f}_{motor}$ from the AiO optimization problem. Note that like the demonstration in Chapter 2, all phase threshold coefficients were set to zero, and division-by-zero errors were avoided by setting $\delta = 10^{-4}$ for the torque curves and $\delta = 1$ for the power loss maps based on experience. Tables 7.3-7.4 show the results from AVASIM, which are supplemented by visual comparisons in Figures 7.4-7.7. Using this information, it can be reasonably assumed that the POD representations for this study are accurate.

Table 7.3 AVASIM Results for POD, Front Motor Map

Index	Max-Torque	Min-Torque	Power Loss
E_{local}	0.565	0.965	0.612
E_{global}	0.980	0.986	0.883
E_{comb}	0.772	0.976	0.748

Table 7.4 AVASIM Results for POD, Rear Motor Map

Index	Max-Torque	Min-Torque	Power Loss
E_{local}	-0.332	0.894	0.436
E_{global}	0.899	0.922	0.869
E_{comb}	0.284	0.908	0.652

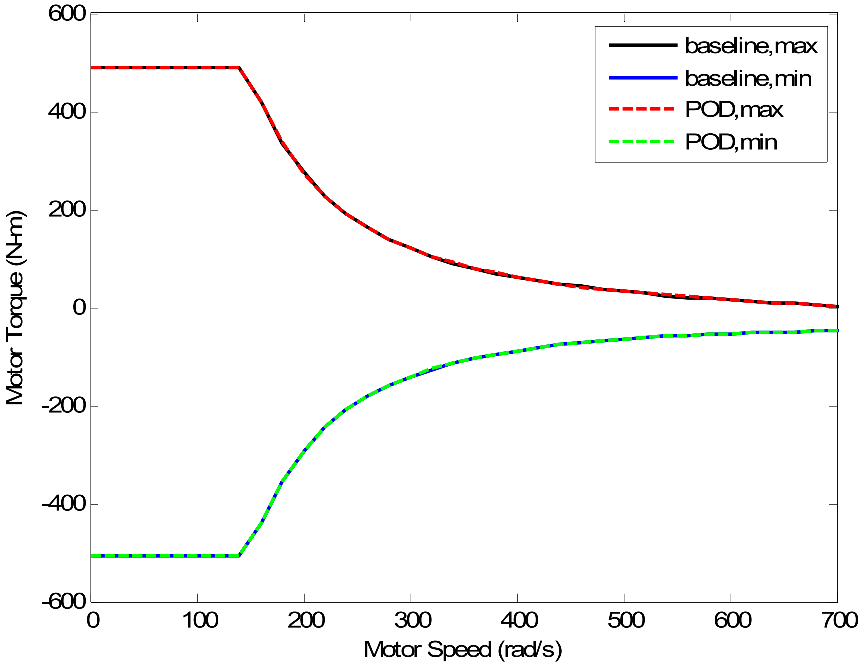

Figure 7.4 Torque Curve Comparison, Front Motors

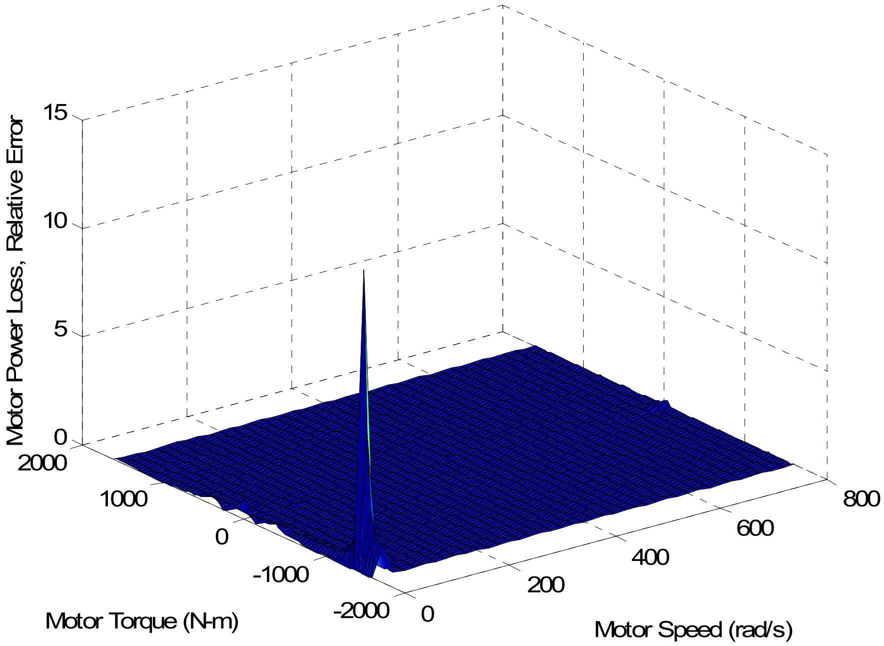

Figure 7.5 Power Loss Map Relative Error, Front Motors

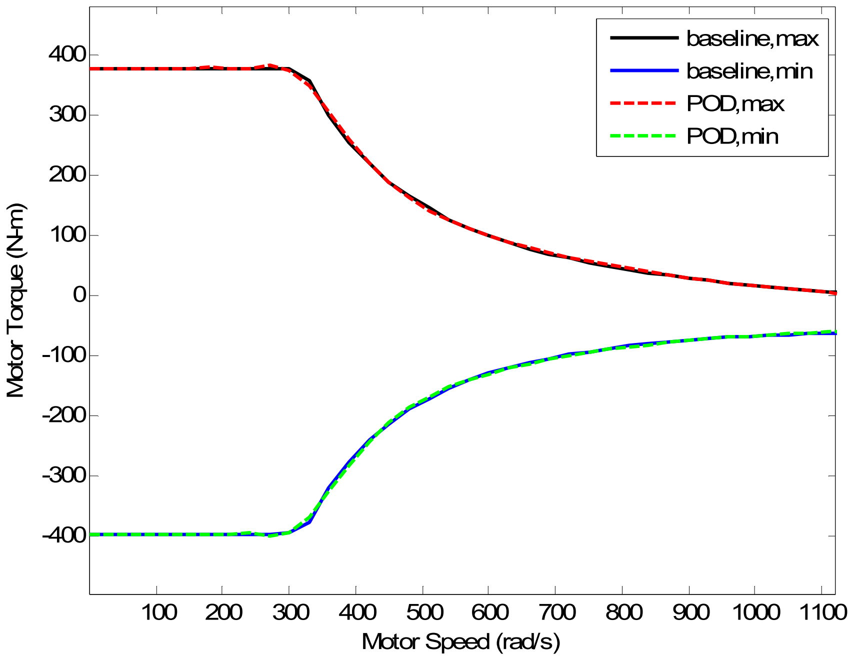

Figure 7.6 Torque Curve Comparison, Rear Motors

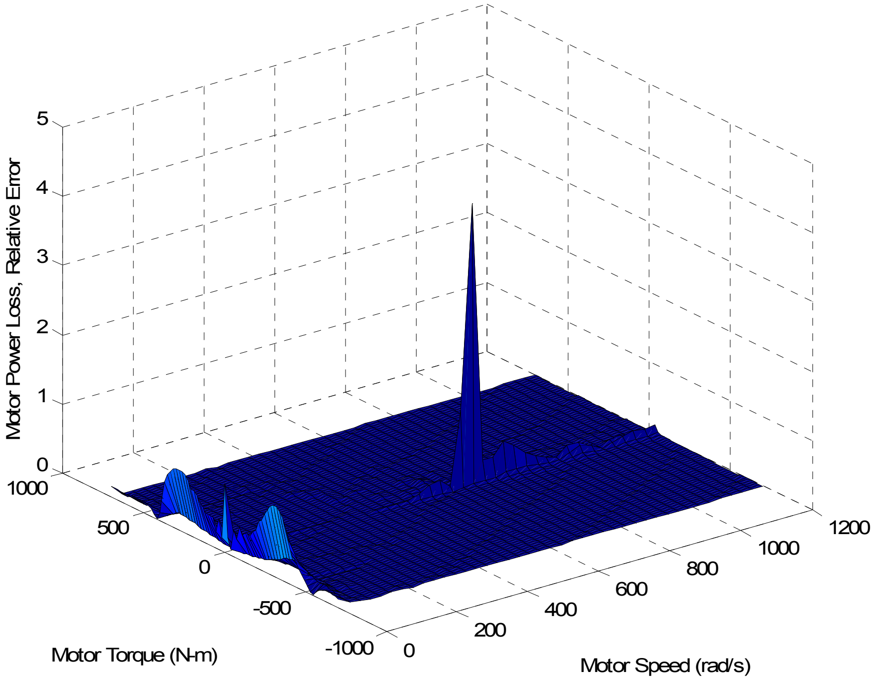

Figure 7.7 Power Loss Map Relative Error, Rear Motors

7.3 SVDD for POD Model Validity Regions

Since the SVDD augmentation was identified as the best constraint management approach for a similar case study in Chapter 6, the same method was implemented for the military EV powertrain design problem. In particular, six SVDD models were developed to approximate the boundaries of the POD model validity regions associated with the maximum and minimum torque curves and power loss maps of the front and rear motors. The data sample vectors upon which the SVDD models were based were identical to those used for the POD representations but mapped appropriately into POD-space as indicated in Equations (6.14)-(6.16) for each set of motors. Based on standard practice, these data sample vectors were subsequently normalized through the MATLAB® function *mapminmax* in order to improve the performance of their associated models. From here, the slack variable penalty constants were set to $C_p = 0.5$, the overfitting targets were set to $P_{target} = 0.10$, and the kernel width parameter bounds were set to $q_{0,min} = 10^{-6}$ and $q_{0,max} = 10$ based on experience for each SVDD problem formulation. In an effort to obtain the global optimum for the tuning problem in Equation (6.13), the non-gradient-based optimizer NOMADm was selected again. However, because of the convexity of the SVDD optimization problem in Equation (6.10), the MATLAB® gradient-based optimizer *fmincon* [*MATLAB® Function Reference*] was selected. In both cases, the default settings were appropriate for the optimizers. Figures 7.8-7.13 illustrate portions of the optimal SVDD boundaries for two dimensions of the POD model validity regions associated with the torque curves and power loss map for the front and rear motors. Finally, note that the total computational effort required for the development of the SVDD models for the front and rear motor maps was 5.76 hours and 5.36 hours, respectively.

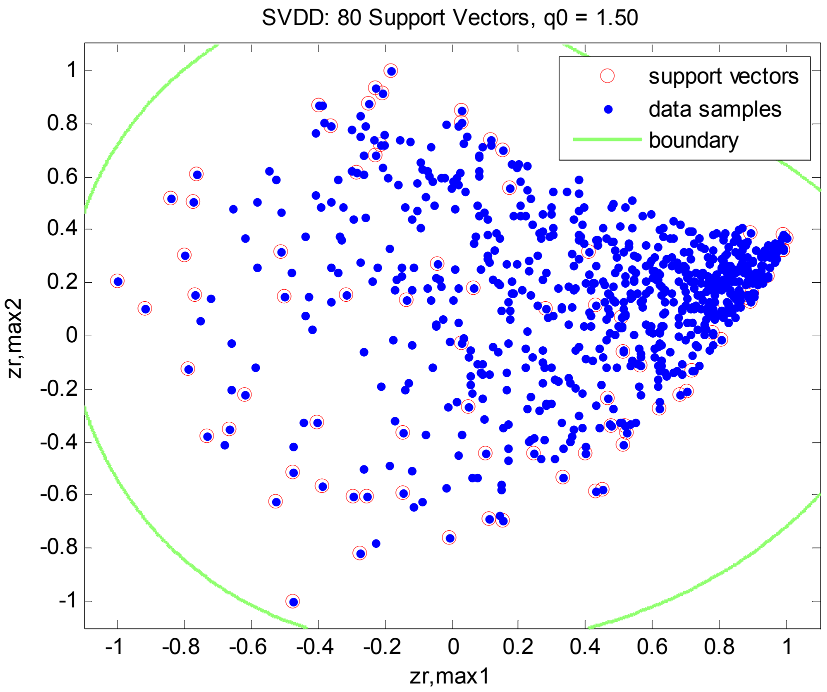

Figure 7.8 Partial SVDD Boundary, Front Max-Torque POD Model Validity Region

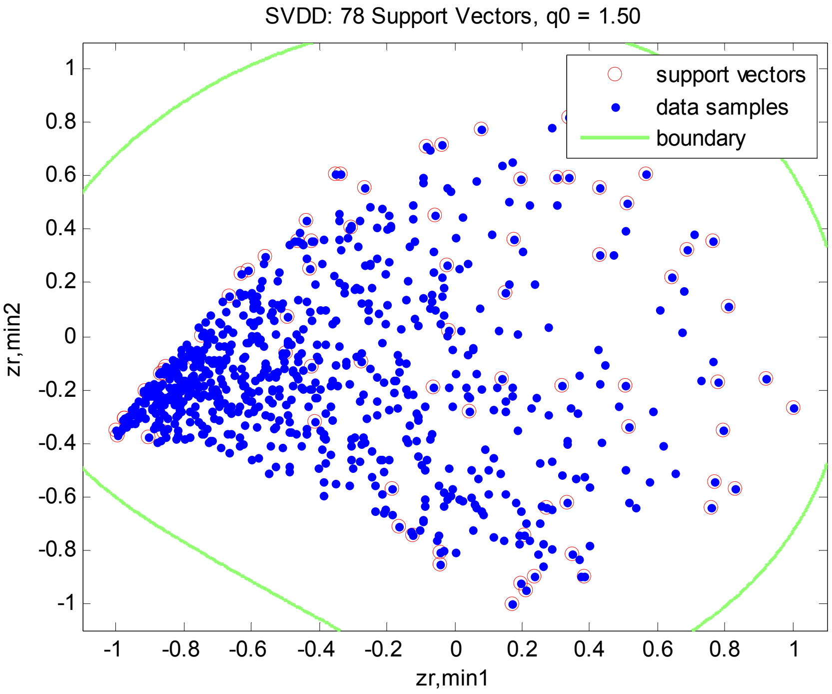

Figure 7.9 Partial SVDD Boundary, Front Min-Torque POD Model Validity Region

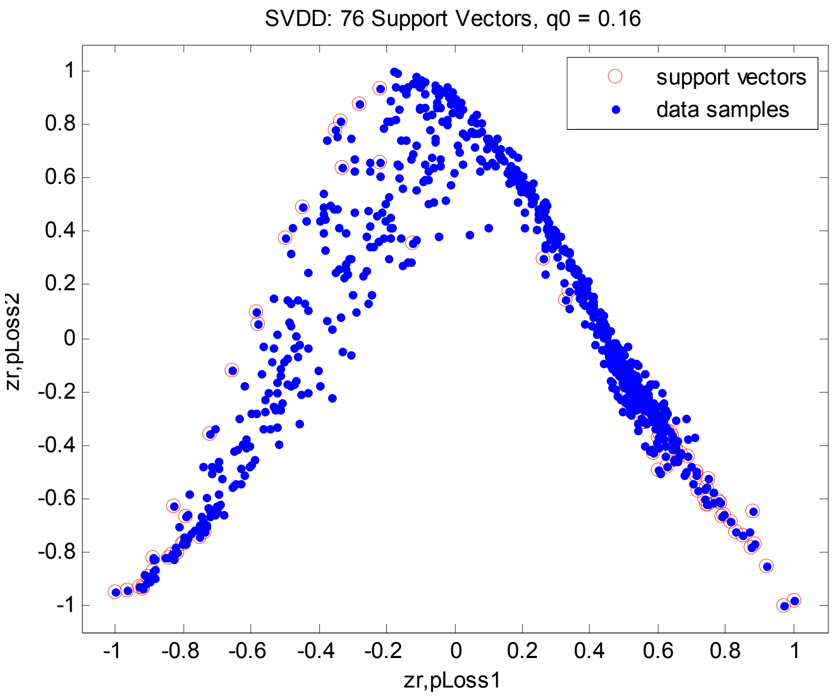

Figure 7.10 Partial SVDD Boundary, Front Power Loss POD Model Validity Region

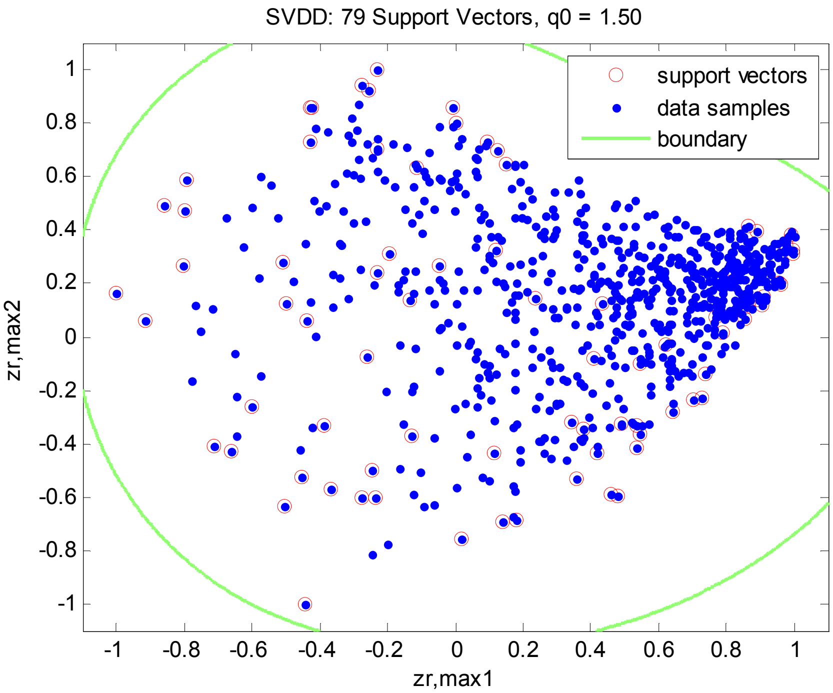

Figure 7.11 Partial SVDD Boundary, Rear Max-Torque POD Model Validity Region

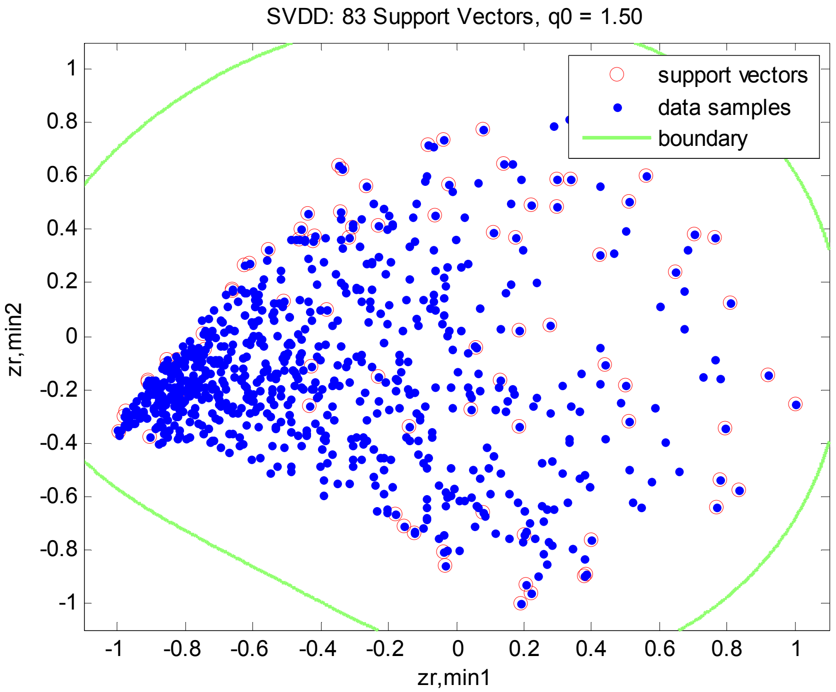

Figure 7.12 Partial SVDD Boundary, Rear Min-Torque POD Model Validity Region

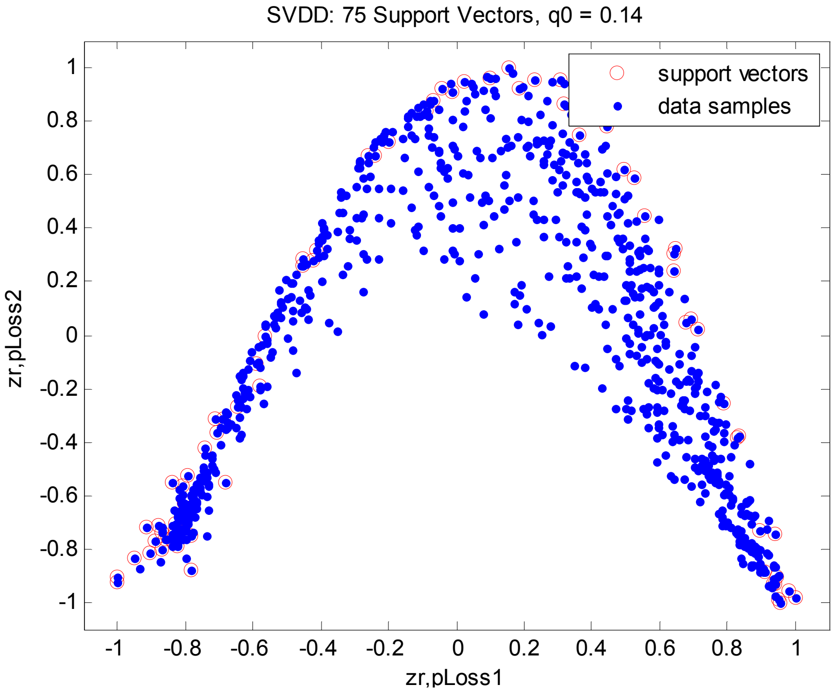

Figure 7.13 Partial SVDD Boundary, Rear Power Loss POD Model Validity Region

7.4 ATC Problem Formulation and Solutions

The ATC problem formulation for the electric LTV consists of a two-level hierarchical decomposition based on Figure 3.14. In this study, the objective of the vehicle subproblem is to maximize the range while minimizing the AL penalty function, whereas the objective of both motor subproblems is to minimize the AL penalty function exclusively. Recall that these penalty functions ensure consistency, or agreement, among the coupled quantities from the vehicle and motor subproblems. Although all of the subproblems are subject to decision variable bound constraints, only the vehicle subproblem contains additional constraints based on battery packaging, performance, motor feasibility, power availability, battery capacity, mobility, and occupant safety.

Applying Equation (2.2) directly, the vehicle subproblem P_{11}, excluding decision variable bound constraints, is formulated as

$$\min_{\bar{\mathbf{x}}_{11}} -R(\bar{\mathbf{x}}_{11}) + \mathbf{v}_{22}^T(\mathbf{t}_{22} - \mathbf{r}_{22}) + \mathbf{v}_{23}^T(\mathbf{t}_{23} - \mathbf{r}_{23}) + \left\| \mathbf{w}_{22} \circ (\mathbf{t}_{22} - \mathbf{r}_{22}) \right\|_2^2 + \left\| \mathbf{w}_{23} \circ (\mathbf{t}_{23} - \mathbf{r}_{23}) \right\|_2^2$$

subject to

$$\begin{array}{ll}
g_{11,1} = b_{w,V}(\bar{\mathbf{x}}_{11}) \le 0 & g_{11,7} = \omega_{V,r}(\bar{\mathbf{x}}_{11}) \le 0 \\
g_{11,2} = b_{\ell,V}(\bar{\mathbf{x}}_{11}) \le 0 & g_{11,8} = P_V(\bar{\mathbf{x}}_{11}) \le 0 \\
g_{11,3} = t_{50}(\bar{\mathbf{x}}_{11}) - t_{50max} \le 0 & g_{11,9} = P_{V50}(\bar{\mathbf{x}}_{11}) \le 0 \\
g_{11,4} = \tau_{V,f}(\bar{\mathbf{x}}_{11}) \le 0 & g_{11,10} = C_b(\bar{\mathbf{x}}_{11}) - C_{bmax}(\mathbf{x}) \le 0 \\
g_{11.5} = \tau_{V,r}(\bar{\mathbf{x}}_{11}) \le 0 & g_{11,11} = -d_s(\bar{\mathbf{x}}_{11}) \le 0 \\
g_{11,6} = \omega_{V,f}(\bar{\mathbf{x}}_{11}) \le 0 & g_{11,12} = P_{fail}(\bar{\mathbf{x}}_{11}) - P_{failmax} \le 0
\end{array}$$

where

$$\begin{aligned}
\bar{\mathbf{x}}_{11} &= [B_I, B_W, B_L, x_{batt}, g_{b,f}, g_{b,r}, \mathbf{z}_{r,comb,f}^T, \mathbf{z}_{r,comb,r}^T, \omega_{max,f}^T, \omega_{max,r}^T, \cdots \\
&\qquad m_{m,f}^T, m_{m,r}^T, J_{r,f}^T, J_{r,r}^T, I_{ym,f}^T, I_{ym,r}^T, I_{zm,f}^T, I_{zm,r}^T, y_{m,f}^T, y_{m,r}^T] \\
\mathbf{t}_{22} &= [\mathbf{z}_{comb,f}^T, \omega_{max,f}^T, m_{m,f}^T, J_{r,f}^T, I_{ym,f}^T, I_{zm,f}^T, y_{m,f}^T],\ \mathbf{z}_{comb,f}^T = \mathbf{f}(\mathbf{z}_{r,comb,f}^T) \\
\mathbf{r}_{22} &= [\mathbf{z}_{comb,f}^R, \omega_{max,f}^R, m_{m,f}^R, J_{r,f}^R, I_{ym,f}^R, I_{zm,f}^R, y_{m,f}^R] \\
\mathbf{t}_{23} &= [\mathbf{z}_{comb,r}^T, \omega_{max,r}^T, m_{m,r}^T, J_{r,r}^T, I_{ym,r}^T, I_{zm,r}^T, y_{m,r}^T],\ \mathbf{z}_{comb,r}^T = \mathbf{f}(\mathbf{z}_{r,comb,r}^T) \\
\mathbf{r}_{23} &= [\mathbf{z}_{comb,r}^R, \omega_{max,r}^R, m_{m,r}^R, J_{r,r}^R, I_{ym,r}^R, I_{zm,r}^R, y_{m,r}^R]
\end{aligned} \tag{7.13}$$

where the constraints $g_{11,1}$-$g_{11,12}$ are identical to the constraints g_1-g_{12} from the AiO problem formulation. The vectors $\mathbf{z}_{comb,f} = [\mathbf{z}_{max,f}, \mathbf{z}_{min,f}, \mathbf{z}_{pLoss,f}]$ and $\mathbf{z}_{comb,r} = [\mathbf{z}_{max,r}, \mathbf{z}_{min,r}, \mathbf{z}_{pLoss,r}]$ refer to the combined vector of original VVCVs for the front and rear motors, respectively. Likewise, the vectors $\mathbf{z}_{r,comb,f} = [\mathbf{z}_{r,max,f}, \mathbf{z}_{r,min,f}, \mathbf{z}_{r,pLoss,f}]$ and $\mathbf{z}_{r,comb,r} = [\mathbf{z}_{r,max,r}, \mathbf{z}_{r,min,r}, \mathbf{z}_{r,pLoss,r}]$ refer to the combined vector of reduced representation variables, which are POD coefficients. Additionally, the vectors $\mathbf{t}_{22}$ and $\mathbf{r}_{22}$ include six scalar-valued coupling variables: $\omega_{max,f}$, $m_{m,f}$, $J_{r,f}$, $I_{ym,f}$, $I_{zm,f}$, and $y_{m,f}$. The vectors $\mathbf{t}_{23}$ and $\mathbf{r}_{23}$ also include similar scalar-valued coupling variables: $\omega_{max,r}$, $m_{m,r}$, $J_{r,r}$, $I_{ym,r}$, $I_{zm,r}$, and $y_{m,r}$. Finally, note that the superscripts T and R indicate target and response versions of the same coupling variable. The front and rear motor subproblems P_{22} and P_{23} are formulated in a similar manner as:

$$\begin{aligned}
&\min_{\bar{\mathbf{x}}_{22}} \mathbf{v}_{22}^T(\mathbf{t}_{22}-\mathbf{r}_{22}) + \left\|\mathbf{w}_{22} \circ (\mathbf{t}_{22}-\mathbf{r}_{22})\right\|_2^2 \\
&\textit{where } \bar{\mathbf{x}}_{22} = [\ell_{s,f}, r_{m,f}, n_{c,f}, R_{r,f}] \\
&\qquad \mathbf{t}_{22} = [\mathbf{z}_{comb,f}^T, \omega_{max,f}^T, m_{m,f}^T, J_{r,f}^T, I_{ym,f}^T, I_{zm,f}^T, y_{m,f}^T] \\
&\qquad \mathbf{r}_{22} = [\mathbf{z}_{comb,f}^R, \omega_{max,f}^R, m_{m,f}^R, J_{r,f}^R, I_{ym,f}^R, I_{zm,f}^R, y_{m,f}^R] = \mathbf{f}(\bar{\mathbf{x}}_{22})
\end{aligned} \tag{7.14}$$

$$\begin{aligned}
&\min_{\bar{\mathbf{x}}_{23}} \mathbf{v}_{23}^T(\mathbf{t}_{23}-\mathbf{r}_{23}) + \left\|\mathbf{w}_{23} \circ (\mathbf{t}_{23}-\mathbf{r}_{23})\right\|_2^2 \\
&\textit{where } \bar{\mathbf{x}}_{23} = [\ell_{s,r}, r_{m,r}, n_{c,r}, R_{r,r}] \\
&\qquad \mathbf{t}_{23} = [\mathbf{z}_{comb,r}^T, \omega_{max,r}^T, m_{m,r}^T, J_{r,r}^T, I_{ym,r}^T, I_{zm,r}^T, y_{m,r}^T] \\
&\qquad \mathbf{r}_{23} = [\mathbf{z}_{comb,r}^R, \omega_{max,r}^R, m_{m,r}^R, J_{r,r}^R, I_{ym,r}^R, I_{zm,r}^R, y_{m,r}^R] = \mathbf{f}(\bar{\mathbf{x}}_{23})
\end{aligned} \tag{7.15}$$

Because the goal of this study was to observe the aggregate contributions of the best consistency measure and the best constraint management method in an ATC framework, the problem formulation in Equations (7.13)-(7.15) was solved using both the "standard" and alternative approach. For the purposes of this study, the "standard" approach includes the RMSE consistency measure and the penalty-value based heuristic for constraint management, whereas the alternative approach refers to the generalized AVASIM consistency measure and the SVDD augmentation for constraint management.

Note that the latter solution methodology requires weights to be prescribed within AVASIM, which were set to w_{local} = 1/3 and w_{global} = 2/3 based on experience. It also introduces six SVDD-related constraints in the P_{11} subproblem:

$$g_{11,13} = R^2_{dist,max,f}(\bar{\mathbf{x}}_{11}) - R^2_{hyp,max,f} \leq 0 \tag{7.16}$$

$$g_{11,14} = R^2_{dist,min,f}(\bar{\mathbf{x}}_{11}) - R^2_{hyp,min,f} \leq 0 \tag{7.17}$$

$$g_{11,15} = R^2_{dist,pLoss,f}(\bar{\mathbf{x}}_{11}) - R^2_{hyp,pLoss,f} \leq 0 \tag{7.18}$$

$$g_{11,16} = R^2_{dist,max,r}(\bar{\mathbf{x}}_{11}) - R^2_{hyp,max,r} \leq 0 \tag{7.19}$$

$$g_{11,17} = R^2_{dist,min,r}(\bar{\mathbf{x}}_{11}) - R^2_{hyp,min,r} \leq 0 \tag{7.20}$$

$$g_{11,18} = R^2_{dist,pLoss,r}(\bar{\mathbf{x}}_{11}) - R^2_{hyp,pLoss,r} \leq 0 \tag{7.21}$$

Once again, NOMADm was selected as the optimizer in order to facilitate consistent results with the AiO problem formulation. In the P_{11} subproblem, the default settings of this optimizer were adjusted such that only a Latin hypercube search was performed and 1,000 function evaluations were permitted. This was necessary to alleviate computational issues associated with memory availability. However, in the P_{22} and P_{23} subproblems, the default settings for NOMADm were appropriate. Finally, in the ATC coordination strategy, the weight update parameter was set to $\beta = 2.75$, the initial weight vectors were set to $\mathbf{v} = \mathbf{0}$ and $\mathbf{w} = \mathbf{1}$, and the tolerance on $\|\mathbf{c}^{(K)} - \mathbf{c}^{(K-1)}\|_\infty$ for outer loop convergence was set to 10^{-2}. Due to the complexity of this design problem, all computational work was performed on a 2.8 GHz, 8 GB RAM, Intel® Core™ i7 CPU. The solutions are part of ongoing work as it was seen that more experimentation with the overfitting targets within SVDD would be necessary to produce SVDD-related constraints that enable the convergence of the ATC formulation and thus facilitate a complete comparative study.

7.5 Summary

This chapter explored the design optimization of a military EV powertrain. In particular, an AiO problem formulation was introduced and solved and an ATC problem formulation was constructed. The solutions of this latter optimization problem formulation, which will be based on a “standard” (RMSE consistency measure and penalty value-based heuristic) and alternative (generalized AVASIM consistency measure and SVDD augmentation) approach, are part of ongoing work due to the complexities of constructing effective SVDD-related constraints that enable convergence and thus facilitate a complete comparative study. It is expected, however, that the alternative approach will have significant benefits with respect to design solution accuracy and overall computational effort based on independent studies performed in Chapters 5-6.

Chapter 8

Conclusions

With the advent of highly-sophisticated systems such as electric vehicles that require design knowledge from a variety of engineering disciplines, it becomes increasingly advantageous to implement formal, decomposition-based optimization strategies to facilitate design decisions. In techniques such as ATC, this requires systems to be represented as a hierarchical composition of subsystems that interact with one another through the mutual exchange of information. Such behavior is formally captured through coupling variables that serve as a vital link for ensuring that the subsystem design solutions are consistent, or in agreement, with one another.

Many times the coupling variables exchanged among the subsystems are few in number and scalar-valued, which readily enables the use of decomposition-based optimization strategies. However, this dissertation presented other situations in which the coupling variables may be highly-discretized functional data, which lead to high-dimensional, vector-valued quantities. Because each element within these VVCVs is a decision variable in the ATC framework, the design problem can become prohibitively large for optimization. While it is recognized that optimization with respect to highly-discretized functional data may occur in AiO problem formulations as well, this issue is particularly acute in decomposition-based optimization strategies due to the additional computational overhead required for such approaches. Therefore, it was necessary to identify and implement reduced representations of the VVCVs that enabled efficient, practical design optimization while maintaining reasonable accuracy.

8.1 Summary

In Chapters 1-2, POD was introduced as a promising reduced representation method since it utilized data samples exclusively to determine the functional form of its approximation model, required minimal assumptions about the number of reduced representation variables (POD coefficients), and generated a relatively small number of such variables for approximation [*Alexander et al.* (2010a)]. Chapter 4 explored the capability of POD as a reduced representation method within ATC further by experimenting with a tuning parameter known as the CPV and observing its overall impact on design solution accuracy and optimization efficiency. This parameter, which balances dimensionality reduction (and hence the number of reduced representation variables) with model accuracy, was set to its "nominal" value (CPV_{goal} = 99.99%) as well as two other values (CPV_{goal} = 99.95% and CPV_{goal} = 99.85%) and yielded the best design solution in terms of accuracy and efficiency (minimal runtime) at CPV_{goal} = 99.99%. While the link between model accuracy and design solution accuracy was straightforward, the behavior with respect to optimization efficiency was not anticipated. It was reasoned that the high-fidelity POD representation enhanced the capability of achieving functional data consistency in ATC through additional degrees of freedom (POD coefficients), thus leading to fewer ATC iterations and a faster runtime. Hence, it was concluded that high-fidelity POD representations would be most appropriate for the reduced representation of VVCVs in ATC.

Although the reduced representation variables served as decision variables during optimization, they still had to compute approximations of the corresponding functional data since these were needed in the underlying analysis models. Moreover, since the functional data existed as coupled information in a decomposition-based optimization strategy, it was most meaningful to use the functional data directly to assess their discrepancies among similar information from other subproblems. Because these discrepancies ultimately impact the convergence of the optimization strategy, it was necessary to implement an appropriate consistency measure (and hence error metric) for these functional data. Since the literature did not indicate any well-established functional data consistency measure for decomposition-based design optimization, Chapter 1 introduced AVASIM as an alternative to the "standard" RMSE metric since it could systematically, objectively and efficiently provide a clear indication of local and global functional data accuracy with respect to preset thresholds [*Sohns et al.* (2006)]. The offline capability of AVASIM was demonstrated in Chapter 2 for both 1D and 2D applications, and its flexibility in allocating the importance of local versus global functional data accuracy through a generalized formulation was also highlighted. Chapter 5 then leveraged this capability to formally investigate AVASIM and generalized AVASIM as potential alternatives for measuring functional data consistency. Based on the results, it was found that the generalized AVASIM consistency measure (with an emphasis on global accuracy) was ideal for functional data as it provided a clear indication of consistency and led to the most accurate design solution in the least amount of time. In particular, the global measure was more stable than the local measure within generalized AVASIM and thus provided more accurate design solutions using fewer function evaluations.

Another issue that was highlighted in Chapter 1 was the inability to properly constrain the reduced representation variables. Because many times these variables are abstract quantities, it can be challenging to identify their decision space (and hence model validity region) beyond simple variable bounds. This assumption, however, could lead to ill-behaved analysis and optimization; therefore, it was necessary to implement an effective constraint management technique for the reduced representation variables. While recent work demonstrated that a penalty value-based heuristic was effective, it also indicated that this approach was inefficient as it led to many optimization iterations and extensive runtimes. Furthermore, more direct approaches such as probability density-based models and convex hulling algorithms had significant shortcomings that made them unsuitable as competitive alternative solutions. To address this issue, Chapter 6 presented an alternative approach which augmented the penalty value-based heuristic with explicit constraints through SVDD. The results from this study indicated that the SVDD augmentation was the best constraint management technique since it yielded the best design solution in terms of accuracy and efficiency (minimal computational effort). Moreover, it was indicated that this would be the most promising constraint management method for abstract decision variables in the majority of optimization problems (both decomposition-based and AiO) since the SVDD-related constraints forced the optimizer to perform more function evaluations in the feasible decision space, thus leading to a higher probability of convergence to the optimal design solution with fewer overall function evaluations (and hence less runtime) instead of convergence to any feasible (yet suboptimal) solution.

Finally, in an effort to examine the aggregate contributions of using the most promising POD representations, consistency measure, and constraint management technique in a single decomposition-based optimization framework, Chapter 7 proposed an ATC problem formulation for the larger-scale military EV powertrain model. The complete comparative study between the "standard" (RMSE consistency and penalty value-based heuristic) and the alternative (generalized AVASIM consistency measure and SVDD augmenetation) solution approach is part of ongoing work due to the challenges in constructing SVDD-related constraints that enable convergence. However, it is expected that the alternative approach will yield significant contributions with respect to design solution accuracy and overall computational effort based on the independent results in Chapters 5-6.

8.2 Relevance of Work

Although all of the work in this dissertation is relevant to decomposition-based optimization strategies, two out of the three core research elements can be applied to any design optimization strategy in general, including single, AiO problem formulations. In particular, the selection and constraint management of decision variables that serve as efficient alternatives to functional data in simulation-based design is critical in many problem domains. For example, in controls-related problems, it is often desired to identify the optimal input signal to a dynamic system that can satisfy some prescribed output behavior. This signal may be nominally represented through an extensive discretization with respect to its states which could lead to a prohibitively large number of decision variables in an optimization framework. A reduced representation would be necessary to facilitate design optimization, and POD would be particularly appropriate since it is a well-established dimensionality reduction technique for linear, time-invariant, state-space systems. Furthermore, to ensure that the problem is well-posed with respect to the reduced representation variables, a constraint management approach such as the SVDD augmentation would be appropriate.

While the importance of a suitable consistency measure is relevant in decomposition-based optimization strategies only, the error metric upon which it is based can be implemented in a variety of situations. In the context of design optimization, one could use the combined error index E_{comb} within a generalized AVASIM formulation as the objective function for a curve-fitting problem similar to [*Sohns et al.* (2006)]. Such an approach would significantly enhance the meaning of the curve-fitting accuracy at the optimal solution compared to the RMSE measure. The same can be said of AVASIM for offline (i.e., non-optimization) accuracy assessment applications. Moreover, unlike many other error metrics, the proven capability of AVASIM for both 1D and 2D functional data demonstrates its potential for higher dimensional applications as well.

Finally, the ideas presented in this dissertation can be applied to simulation-based design problems involving computational geometry, as in Toal et al. [*Toal et al.* (2008)]. The nominal geometric representation in such problems is typically a series of Bezier curves or B-splines, which are constructed from a set of control points in space. For simple rectangular shapes, the set of control points is usually small, but for more complex, freeform shapes, it can increase dramatically. Furthermore, the number of control points can expand rapidly as the geometric design problem transitions from 2D to 3D applications. Such a geometric representation would make a formal design optimization study intractable since the control points would serve as decision variables. Therefore, an appropriate reduced representation along with a constraint management technique for its associated variables would be necessary for efficient, practical optimization. Likewise, an accuracy assessment tool such as AVASIM would facilitate any comparisons between a full, computational geometric representation and its approximation. This includes comparisons between 3D shapes since the 2D AVASIM formulation is designed to measure errors between surfaces.

8.3 Contributions

This dissertation directly addressed the three research questions that were presented in Chapter 1. To that end, the significant contributions to the research community are:

1. The identification of the impact of the number of reduced representation variables on the computational efficiency and accuracy of ATC. This was done for POD only, and it was found that the highest model fidelity (and hence largest number of reduced representation variables) for POD yielded the best ATC design solution with respect to efficiency and accuracy.
2. The identification of a suitable consistency measure for coupled, functional data within an ATC framework. In particular, it was found that the generalized AVASIM metric was an appropriate functional data consistency measure within ATC.
3. The identification of an effective constraint management method for reduced representation variables in an optimization framework. Specifically, it was demonstrated that a penalty value-based heuristic coupled with SVDD was an appropriate constraint management approach for the reduced representation variables. Note that the primary factor for the success of this method was SVDD. Also, although the original research question was addressed in an ATC framework, the general approach is applicable to almost any optimization problem with abstract decision variables. Therefore, this research contribution has the broadest implications of any in this dissertation.

In addition to these research contributions, the following practical contributions were made:

4. The enhancement of a detailed, commercial EV powertrain model that was originally developed by Allison [*Allison* (2008)]. The most significant of these improvements was the inclusion of a motor mass analysis model to account for energy efficiency and vehicle range tradeoffs.
5. The development of a large-scale, reconfigured version of the commercial EV powertrain model for a military vehicle application. The new developments

included a model accounting for power transmission (gearbox) design and a four-wheel drive version of the powertrain simulations.

8.4 Future Work

The most significant consideration that would enhance this work is the exploration of alternative reduced representation methods. As it was stated in Chapter 1, POD is a very promising approach since it satisfies the selection criteria for a reduced representation better than many of the "classical" techniques. However, this does not indicate that POD is always the best technique; indeed, for many problems, it still requires more reduced representation variables than desired, which, for decomposition-based optimization strategies, would be equivalent to the number of local design variables in a subproblem. Because this dissertation introduced a better functional data consistency measure and constraint management method to support decomposition-based design optimization, comparative studies between POD and competitive alternatives such as wavelet decomposition would be easily facilitated. Such studies should include, but not be limited to, the investigation of the impact of tuning parameters within the reduced representation models on the condition of the optimization problem.

Another aspect of this work that should be further investigated is a more complete assessment of the generalized AVASIM consistency measure. This includes, but is not limited to, the improvement of the local error measure, the methodology for assigning weights to the local and global error indices, and their impact on problem condition. As discussed in Chapter 2, the local error index can be rather unstable for target points near zero, and although this behavior is largely problem-dependent it would be ideal to identify general countermeasures beyond minimal weight allocation. Chapter 5 explained further that these weights were set based on experience and that such an approach may not be appropriate for other types of problems. After completing newer studies, one may even consider the exploration of alternative consistency measures based on other error metrics; however, such an investigation would be a challenging task given the clarity in identifying functional data consistency provided by generalized AVASIM as well as its demonstrated capability for higher dimensional (e.g., 2D) functional data.

Another research question that should be explored in future work is the effect of the SVDD overfitting target on the accuracy of design optimization solution. Recall from Chapter 6 that it is almost always likely that the SVDD augmentation will improve the optimization runtime as it imposes explicit constraints that restrict the search of the optimizer to the feasible decision space. However, it was also mentioned that an aggressive overfitting target increases the probability of overfitting error, which essentially means that some decision vectors, including the optimal decision vector, could be erroneously rejected from the feasible decision space. This behavior has already been seen when attempting to solve the ATC problem formulation for the military EV powertrain model in Chapter 7. In general, the extent to which this could occur is partially dependent on the sensitivity of the SVDD boundaries to changes in the overfitting target. Therefore, such a study could provide greater insight into the strengths and limitations of SVDD for the constraint management of reduced representation variables.

Finally, from a design perspective, this work could be improved by the addition of more detailed EV powertrain analysis models and simulations. The case studies in this dissertation have already shown how the inclusion of a simple, yet important motor mass analysis model can enhance the meaning of design tradeoffs such as energy efficiency and vehicle range. The addition of other components such as explicit battery cost and thermal management models, power inverter models, improved motor models, and heavy duty transmission models would further capture the extensive tradeoffs for such a multidisciplinary design problem. Moreover, a more detailed, comprehensive set of models could better demonstrate the utility of the research contributions discussed in this dissertation.

Bibliography

Abramson, M. (2007), *NOMADm Version 4.5 User's Guide*, Air Force Institute of Technology, Wright Patterson AFB.

Ahmed, N. and Goldstein, M. H. (1975), *Orthogonal Transforms for Digital Signal Processing*, Springer, Berlin.

Alexander, M. J. (2008), Analytical target cascading optimization of an electric vehicle powertrain system, M.S. thesis, Mechanical Engineering, University of Michigan, Ann Arbor, MI.

Alexander, M. J., Allison, J. T., and Papalambros, P. Y. (2009), Reduced representations of vector-valued coupling variables in decomposition-based design optimization, in the *8th World Congress on Structural and Multidisciplinary Optimization*, Lisbon, Portugal.

Alexander, M. J. and Papalambros, P. Y. (2010), An accuracy assessment method for two-dimensional functional data in simulation-based design, in the *13th AIAA/ISSMO Multidisciplinary Analysis and Optimization Conference*, Fort Worth, TX.

Alexander, M. J., Allison, J. T., and Papalambros, P. Y. (2010a), Reduced representations of vector-valued coupling variables in decomposition-based design optimization, *Structural and Multidisciplinary Optimization* (submitted).

Alexander, M. J., Allison, J. T., Papalambros, P. Y., and Gorsich, D. J (2010b), Constraint management of reduced representation variables in decomposition-based design optimization, in the *2010 ASME International Design Engineering Technical Conferences*, DETC2010-28788, Montreal, Canada.

Alexander, M. J., Allison, J. T., and Papalambros, P. Y. (2010c), Decomposition-based design optimization of electric vehicle powertrains using proper orthogonal decomposition, *International Journal of Powertrains* (submitted).

Allison, J. T. (2008), Optimal partitioning and coordination decisions in decomposition-based design optimization, Ph.D. dissertation, Mechanical Engineering, University of Michigan, Ann Arbor, MI.

AM General LLC (2009), *Amgeneral.com*, http://www.amgeneral.com/, (12/1)2009.

Amin, B. (2001), *Induction Motors: Analysis and Torque Control*, Springer-Verlag, Berlin.

Barber, C. B., Dobkin, D. P., and Huhdanpaa, H. T. (1996), The Quickhull algorithm for convex hulls, *ACM Transactions on Mathematical Software*, *22*(4), 469-483.

Bose, B. K. (2002), *Modern Power Electronics and AC Drives*, Prentice Hall, Inc., Upper Saddle River, NJ.

Box, G. E. P. and Hunter, J. S. (1957), Multi-factor experimental designs for exploring response surfaces, *The Annals of Mathematical Statistics*, *28*, 195-241.

Box, G. E. P. and Draper, N. R. (1987), *Empirical Model-Building and Response Surfaces*, Wiley, New York.

Braun, R. (1996), Collaborative optimization: an architecture for large-scale distributed design, Ph.D. dissertation, Stanford University, Palo Alto, CA.

Bretscher, O. (2005), *Linear Algebra with Applications*, Pearson Prentice Hall, Upper Saddle River, NJ.

Bui-Thanh, T., Damodaran, M., and Wilcox, K. (2004), Aerodynamic reconstruction and inverse design using proper orthogonal decomposition, *AIAA Journal*, *42*(8), 1505-1516.

Burkhardt, J., Du, Q., Gunzburger, M., and Lee, H. C. (2003), Reduced order modeling of complex systems, in the *20th Biennial Conference on Numerical Analysis*, 29-38, Dundee, Scotland.

Chen, S., Cowan, C. F. N, and Grant, P. M. (1991), Orthogonal least squares learning algorithm for radial-basis function networks, *IEEE Transactions on Neural Networks*, *2*(2), 302-309.

Cook, R. D. and Young, C. Y. (1999), *Advanced Mechanics of Materials*, Prentice Hall, Upper Saddle River, NJ.

Cramer, E., Dennis, J., Frank, P., Lewis, R., and Shubin, G. (1994), Problem formulation for multidisciplinary optimization, *SIAM Journal of Optimization*, *4*(4), 754-776.

Cuenca, R. M., Gaines, L. L., and Vyas, A. D. (1999), Evaluation of electric vehicle production and operating costs, *Tech. Rep. ANL/ESD-41*, Argonne National Laboratory, Argonne, IL.

Delagrammatikas, G. J. (2001), A design optimization methodology for advanced and hybrid, diesel-based, automotive powertrains, Ph.D. dissertation, Mechanical Engineering, University of Michigan, Ann Arbor, MI.

Demuth, H., Beale, M., and Hagan, M. (2009), MATLAB® Neural Network Toolbox™ Version 6.0.2 User's Guide, The MathWorks, Inc., Natick, MA.

Doyle, M., Fuller, T. H., and Newman, J. (1993), Modeling of galvanostatic charge and discharge of the lithium/polymer/insertion cell, *Journal of The Electrochemical Society*, *140*(6), 1526–1533.

Ersal, T., Kittirungsi, B., Fathy, H. K., and Stein, J. L. (2009), Model reduction in vehicle dynamics using importance analysis, *Vehicle Systems Dynamics*, *47*(7): 851-865.

Fang, P., Wu, Z., Shen, F., Ge, Y., and Fang, B. (2005), Improved DTW algorithm for online signature verification based on writing forces, in the *International Conference on Intelligent Computing*, 631-640.

Faundez-Zanuy, M. (2007), On-line signature recognition based on VQ-DTW, *Pattern Recognition Letters*, *40*, 981-992.

Fuller, T. H., Doyle, M., and Newman, J. (1994), Simulation and optimization of the dual lithium ion insertion cell, *Journal of The Electrochemical Society*, *141*(1): 1–10.

Geers, T. L. (1984), Objective error measure for the comparison of calculated and measured transient response histories, *Shock and Vibration Bulletin*, 99-107.

George, P. and Ogot, M. M. (2006), A compromise experimental design method for parametric polynomial response surface approximations, *Journal of Applied Statistics*, *33*(10), 1037-1050.

Glasbey, C. A. and Mardia, K. V. (1998), A review of image-warping methods, *Journal of Applied Statistics*, *25*(2), 155-172.

Han, J. (2008), Sequential linear programming coordination strategy for deterministic and probabilistic analytical target cascading, Ph.D. dissertation, Mechanical Engineering, University of Michigan, Ann Arbor, MI.

Hodge, N. (2010), Humvee proves tough to follow, *The Wall Street Journal-WSJ.com*, http://online.wsj.com/article/SB10001424052748703280004575308883320671168.html?mod=ITP_pageone_1, (6/15)2010.

Jacob, C., Charras, F., Trosseille, X., Hamon, J., Pajon, M., and Lecoz, J. Y. (2000), Mathematical models integral rating, *International Journal of Crashworthiness*, *5*(4), 417-431.

Karhunen, K. (1946), Zur spektral theorie stochastischer prozesse, *Annales Academiae Scientiarum Fennicae Ser*, *34*.

Keogh, E. and Pazzani, M. (1999), Scaling up dynamic time warping to massive datasets, in the *3rd European Conference on Principles and Practice of Knowledge Discovery in Databases*, 1-11.

Kim, H.-M. (2001), Target cascading in optimal system design, Ph.D. dissertation, Mechanical Engineering, University of Michigan, Ann Arbor, MI.

Kim, H.-M., Michelena, N. F., Papalambros, P. Y., and Jiang, T. (2003), Target cascading in optimal system design, *Journal of Mechanical Design*, *Transactions of the ASME*, *125*(3), 474-480.

Kokkolaras, M., Louca, L. S., Delagrammatikas, G. J., Michelena, N. F., Filipi, Z. S., Papalambros, P. Y., Stein, J. L., and Assanis, D. N. (2004), Simulation-based optimal design of heavy trucks by model-based decomposition: an extensive analytical target cascading case study, *International Journal of Heavy Vehicle Systems*, *11*(3/4), 402-431.

Larminie, J. and Lowry, J. (2003), *Electric Vehicle Technology Explained*, John Wiley and Sons, Chichester.

LeGresley, P. A. and Alonso, J. J. (2004), Improving the performance of design decomposition methods with POD, in the *10th AIAA/ISSMO Multidisciplinary Analysis and Optimization Conference*, AIAA 2004-4465, Albany, NY.

Liu, J., Cheng, Q., Zheng, Z., and Qian, M. (2002), A DTW-based probability model for speaker feature analysis and data mining, *Pattern Recognition Letters*, *23*, 1271-1276.

Loeve, M. (1945), Functions aleatoire de second ordre, *C R Academie des Sciences*, Paris, France.

Lucia, D. J., Beran, P. S., and Silva, W. A. (2003), Reduced order modeling: new approaches for computational physics, *Progress in Aerospace Sciences*, *40*, 51-117.

Malak, R. J. (2008), Using parameterized efficient sets to model alternatives for systems design decisions, Ph.D. dissertation, Mechanical Engineering, Georgia Institute of Technology, Atlanta, GA.

Malak, R. J. and Paredis, C. J. J. (2009), Using support vector machines to formalize the valid input domain of models in data-driven predictive modeling for systems design, in the *2009 ASME International Design Engineering Technical Conferences*, DETC2009-87376, San Diego, CA.

MATLAB® Function Reference, The MathWorks, Inc., Natick, MA.

Meade A. J. and Kokkolaras, M. (1996), Enhancement of a viscous-inviscid-interaction airfoil analysis code using the parallel direct search algorithm, *Tech. Rep. CRPC TR96711-S*, Rice University, Houston, TX.

Meckesheimer, M., Barton R. R., Simpson, T., Limayem, F., and Yannou, B. (2001), Metamodeling of combined discrete/continuous responses, *AIAA Journal*, *39*(10), 1950-1959.

Michelena, N., Park, H., and Papalambros, P. Y. (2003), Convergence properties of analytical target cascading, *AIAA Journal*, *41*(5), 897-905.

Mullur, A. A. and Messac, A. (2005), Extended radial basis functions: more flexible and effective metamodeling, *AIAA Journal*, *43*(6), 1306-1315.

Nissan Zero Emissions Website (2010), *Nissan-zeroemission.com*, http://www.nissan-zeroemission.com/EN/index.html, (6/1)2010.

Papalambros, P. Y. and Wilde, D. J. (2000), *Principles of Optimal Design: Modeling and Computation*, Cambridge University Press, New York.

PNGV Battery Test Manual Revision 3, *DOE/ID-10597*, February 2001.

Raser Technologies, Inc. (2010), *Rasertech.com*, http://www.rasertech.com/, (3/27)2010.

Ratanamahatana, C. A., and Keogh, E. (2004), Everything you know about dynamic time warping is wrong, in the *3rd Workshop on Mining Temporal and Sequential Data*, in conjunction with the *10th ACM SIGKDD International Conference on Knowledge Discovery and Data Mining*, 22-25.

Rexnord (2010), *Rexnord.com*, http://pt.rexnord.com/products/gear_drives/drive_one/driveone.asp, (4/1)2010.

Russell, D. M. (1997a), Error measures for comparing transient data: Part I, development of a comprehensive error measure, in the *68th Shock and Vibration Symposium*, Hunt Valley, MD.

Russell, D. M. (1997b), Error measures for comparing transient data: Part II, error measures case study, in the *68th Shock and Vibration Symposium*, Hunt Valley, MD.

Sansone, G. and Hille, E. (2004), *Orthogonal Functions*, Dover Publications Inc., Mineola, NY.

Sarin, H. (2008), Error assessment of response time histories (EARTH): A metric to validate simulation models, M.S. thesis, Mechanical Engineering, University of Michigan, Ann Arbor, MI.

Schwer, L. E. (2005), Validation metrics for response histories: a review with case studies, *Tech. Rep.*, Schwer Engineering & Consulting Service, Windsor, CA.

Scrosati, B. (1992), Lithium rocking chair batteries: an old concept?, *Journal of The Electrochemical Society*, *139*(10), 2776–2781.

Sendur, P., Stein, J. L., Loucas, L., and Peng, H. (2002), A model accuracy and validity algorithm, in the *ASME International Mechanical Engineering Congress and Exposition*, IMECE2002-DSC-34284, New Orleans, LA.

Sirovich, L. (1987), Turbulence and the dynamics of coherent structures. I – coherent structures. II – symmetries and transformations. III – dynamics and scaling, *Quarterly of Applied Mathematics*, *43*, 561-571, 573-590.

Smart USA (2010), *Smartusa.com*, http://www.smartusa.com/, (9/20)2010.

Sobieski, I. and Kroo, I. (1996), Aircraft design using collaborative optimization, in the *AIAA 34th Aerospace Sciences Meeting and Exhibit*, Reno, NV.

Sobieszczanski-Sobieski, J., James, B. B., and Dovi, A. R. (1985), Structural optimization by multilevel decomposition, *AIAA Journal*, *21*, 1291-1299.

Sohns, B., Allison, J., Fathy, H., and Stein, J. L. (2006), Parameterization of a HMMWV model through the use of model validation techniques, in the *Society of Automotive Engineers World Congress*.

Sprague, M. A. and Geers, T. L. (2004), A spectral-element method for modeling cavitation in transient fluid structure interaction, *International Journal for Numerical Methods in Engineering*, *60*(15), 2467-2499.

Stegmann, M. B. (2001), Image warping, *Tech. Rep.*, Technical University of Denmark, Copenhagen, Denmark.

Tarassenko, L., Hayton, P., Cerneaz, N., and Brady, M. (1995), Novelty detection for the identification of masses in mammograms, in the *4th International Conference on Artificial Neural Networks*, 442-447, Cambridge, UK.

Tax, D. M. J. and Duin, R. P. W. (1999a), Data domain description using support vectors, in the *European Symposium on Artificial Neural Networks*, 251-256, Bruges, Belgium.

Tax, D. M. J. and Duin, R. P. W. (1999b), Support vector domain description, *Pattern Recognition Letters*, *20*, 1191-1199.

Toal, D. J. J., Bressloff, N. W., and Keane, A. J. (2008), Geometric filtration using POD for aerodynamic design optimization, in the *26th AIAA Applied Aerodynamics Conference*, AIAA 2008-6584, Honolulu, HI.

Tosserams, S., Etman, L. F. P., Papalambros, P.Y., and Rooda, J. E. (2006), An augmented-Lagrangian relaxation for analytical target cascading using the alternating direction method of multipliers, *Structural Multidiscplinary Optimization*, *31*, 176-189.

Vapnik, V. (1995), *The Nature of Statistical Learning Theory*, Springer, New York.

Wagner, T. C. and Papalambros, P. Y. (1993), A general framework for decomposition analysis in optimal design, in the *ASME Advances in Design Automation*, *65*, 315-325, Albuquerque, NM.

Wang, G. G. and Shan, S. (2007), Review of metamodeling techniques in support of engineering design optimization, *Journal of Mechanical Design*, *Transactions of the ASME*, *129*(4), 370-380.

Wilcox, K. (2005), An introduction to model reduction for large scale applications, *Aerospace Computational Design Laboratory Seminar*, http://web.mit.edu/mor/papers/ADCL_Sept05.pdf, Massachusetts Institute of Technology, (5/1)2007.

Wong, J. Y. (2001), *Theory of Ground Vehicles*, JohnWiley and Sons, New York.